WATER STRUCTURE AT TUNABLE SURFACES

A Dissertation

Presented to the Faculty of the Graduate School

of Cornell University

In Partial Fulfillment of the Requirements for the Degree of

Doctor of Philosophy

by

Aliyah Rebecca Barrett

August 22 2016

WATER STRUCTURE AT TUNABLE SURFACES

Aliyah Rebecca Barrett, Ph. D.

Cornell University 2016

The interaction between water and a surface is highly localized and responsive to material properties, driving a diverse set of processes such as lipid membrane assembly, protein folding, proton transfer, and ion adsorption at minerals. However, naturally-occurring surfaces are highly heterogeneous and complex. Model surfaces were developed at which properties such as texture and polarity were independently controlled, and sum frequency generation spectroscopy was used to probe the water structure at these interfaces. A series of mixed hydrophobic monolayers were applied to transparent windows to create textured surfaces. The intensity of non-hydrogen bonded water molecules at the monolayers was found to correlate not with the order of the monomers within the monolayer, but with the monolayer surface area. A strategy to functionalize silica surfaces with densely-packed, well-ordered OH- and COOH-terminated siloxane monolayers was then explored. Monomers with heat labile groups were bound to silica, and the protecting groups were removed by heat after monolayer deposition. While not initially successful, with a change of monomer binding group this technique may be used generally to create high quality monolayers with termini not otherwise compatible with this type of monolayer. In a collaborative project, water structure at polymer filtration membranes was observed in the presence of a biological buffer. It was found that films functionalized with poly (ethylene glycol), used commonly to prevent protein fouling, excluded phosphate ions from the immediate interface. The resulting electrical double layer aligned water molecules at the interface. These findings demonstrate the importance of specific ion effects in surface fouling.

BIOGRAPHICAL SKETCH

Aliyah Barrett received a Bachelor of Science in Chemistry from Randolph-Macon Woman's College in 2009. She has completed her Ph.D. studies under Dr. Poul Petersen, studying surface modification and ultrafast vibrational spectroscopy.

ACKNOWLEDGMENTS

I would like to thank my collaborators Dr. Mingchee Tan, Dr. Kirk Samaroo, Dr. Joseph Imbrogno, Dr. Georges Belfort, and Dr. Jesse Silverberg. With them I was able to solve new challenges and explore new disciplines. Many thanks to all my group members, especially Dr. Carmella Calabrese, Dr. Luke McDermott, and Heather Vanselous, for support in the lab. I am grateful for the advice and help from Dr. Chad Lewis, Dr. Wesley Morris, Dr. Brian Lindley, Dave Vaccarello, Dr. Brandon Tiegs, and Parker Singleton in my synthetic projects.

For their time and guidance, I thank my committee members Dr. John Marohn and Dr. Roger Loring. Most of all, thanks to my advisor Dr. Poul Petersen for his encouragement and support.

This project was supported by the National Sciences Foundation (NSF CAREER Award: CHE-1151079).

TABLE OF CONTENTS

LIST OF FIGURES

LIST OF TABLES

1. Introduction

1.1. Motivation

Due to its ubiquity, polarity, and ability to form cohesive yet dynamic networks, water drives many of the processes on this planet. Some phenomena can be explained adequately knowing only water's macroscopic properties, such as heat distribution by convective ocean currents.[1-3] Others require a molecular understanding of water in the bulk, such as hydration of ions and small solutes.[4-7] Hydration of extended surfaces, charged and neutral, polar and nonpolar, is qualitatively different than that in the bulk. Processes occurring at extended water interfaces include reactions at atmospheric aerosols,[8,9] reactions catalyzed at water/oil emulsions,[10] and adsorption of ions at minerals.[11-13] Whereas the energy of solvation of small solutes (< 1 nm in radius) is entropically driven, dependent on the volume of water excluded, solvation of larger bodies is enthalpically driven, going as the surface area of the body.[14] This surface area dependence arises because an extended interface is too large to be accommodated without breaking hydrogen bonds, unlike small solutes which can be solvated by rearranging hydrogen bonds. Instead, the hydrogen bonding network of the bulk is terminated, and the energy of breaking hydrogen bonds manifests itself in the macroscopic surface tension.

Interfacial water is particularly important in biology for its role in lipid membrane assembly, protein folding, and proton transfer. Given the high density of biomolecules in a cell, there is only on average ~20 – 30 Å between any two biomolecules,[15] and so a large fraction of water molecules will be within the hydration shell of a biomolecule and engaging in correlated, collective hydrogen-bond motions.[16-19] A topic of broad practical interest is the prevention of

biofilm formation and protein adhesion, which has applications in marine vessels coatings,[20,21] indwelling medical devices (such as joint prostheses, catheters, contact lenses, and implantable cardiac defibrillators),[22-24] and filtration membranes.[25,26] Understanding the hydration of biomolecules and surfaces, as well as the interaction between hydration shells, is key to targeted design of anti-fouling surfaces.[27,28] The challenge is to attain general rather than specific resistance to attachment, as proteins and polysaccharides exist in a wide range of shapes, sizes, charges, and polarities. Furthermore, some organisms, such as barnacles and *Staphylococcus epidermidis,* have evolved effective adhesive materials which are a key part of their lifecycle (barnacles)[20] or impart resistance to antibiotics and immune response (*S. epidermidis*).[29]

As important as naturally-occurring surfaces are, they are also highly complex and therefore difficult to study. The focus of this research has been to create tunable and well-characterized surfaces at which to observe water structure to determine the effect of specific surface properties.

1.2. Water

Liquid water at room temperature is extensively hydrogen bonded, with an average of 3.4 hydrogen bonds per molecule compared to 4 in hexagonal ice.[30] Due to the strong intermolecular coupling, the sharp symmetric and asymmetric OH stretching modes observed for water in the gas phase are replaced by a continuous IR and Raman resonance of 3100 - 3600 cm^{-1}. Hydrogen bonds modulate the strength of the associated covalent OH bond (OH), increasing the length of the OH and causing a red-shift in the OH stretching mode.[31,32] Structural heterogeneity in the H-bonding strength and in H-bonding angle are responsible for most of the breadth of the liquid water OH stretching mode, but bonds and molecules in this system cannot be considered

independently of the H-bonding network,[33] nor can the network be considered a static entity. An excitation of an OH stretch is rapidly delocalized to many water molecules by several competing mechanisms. The overtone of the water bending mode (fundamental at 1650 cm^{-1}), overlaps with the stretching mode, and the fast response of the bending mode to excitation of the OH stretch is attributed to its mixed stretch-bend character.[34-36] Another explanation for the rapid transfer of energy, and the loss of the initial polarization of excitation, is resonant vibrational energy transfer (coupling of neighboring transition dipoles).[37] Due to exciton delocalization or resonant energy transfer, as well fluctuations of H-bond length and angle from librations,[38] the relationship between the initial and final OH frequency of a water molecule is scrambled within about 100 fs[36,39] in a process called spectral diffusion. For this reason, the homogeneous OH stretch line width observed at very early waiting times[36,40-42] expands to the several hundred wavenumbers seen in static IR spectra, within the lifetime of the vibration (200 ps).[43] Collective restructuring of the H-bonding network, including rotation (~2.5 ps),[44,45] can be observed in isotopically dilute solutions of HOD in D_2O or H_2O where the mismatch in OD and OH resonances inhibits energy transfer and thus extends the lifetime of the vibration.

At an interface, the number of possible water-water interactions is abruptly reduced, inhibiting collective processes such as energy transfer and reorientation. Fayer and coworkers have studied isotopically diluted water (HOD in H_2O) “nano pools” confined in reverse micelles, which were varied in size to hold 50 – 400,000 water molecules.[46-48] By decomposing the contribution of water at the surface and the core to the population relaxation response, OH stretch vibrational lifetimes were found to be longer for water at the perimeter of the micelles. Reorientation time was lengthened as the reduction in hydrogen bonding partners limited the pathways for rotation. At the water/air surface, non-hydrogen bonded “free" OHs (Figure 1.1) were also found to have a

longer OH stretch vibrational lifetime[49-51] and a longer hydrogen bond lifetime,[5248] but rotate faster than fully hydrogen-bonded molecules in the bulk[50,52] – a water molecule with a free OH rotating on the H-bonded OH axis can reorient by breaking only a single hydrogen bond.[53] Hydrogen bond and OH stretch dynamics of interfacial water molecules are sensitive to the strength of the interaction with the interface. A free OH at the water/air interface is only associated with the water phase by the other OH group on the molecule. Due to the difference in resonance frequencies of the H-bonded and non H-bonded OHs on the same molecule, (~165 cm^{-1} for D_2O)[54] and the lack of hydrogen bonding partners, intra- and inter-molecular energy transfer is limited for the free OH, and the vibration decays over a (3x) longer timescale compared to bulk hydrogen-bonded water.[43] However, strong interactions with a surface can also decouple a bond or a molecule from the bulk, such as hydrogen bonding to a phosphate moiety on a phospholipid[55] or to platinum.[56]

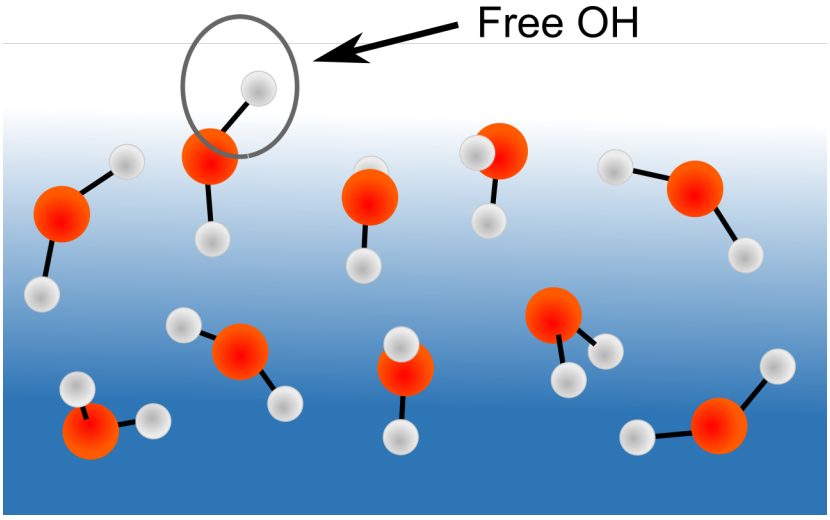

Figure 1.1 Water/air interface with non-hydrogen bonded “free OH."

Terminating the hydrogen bonding network of bulk water at a surface has a high enthalpic cost, and water molecules assume a configuration which minimizes the number of broken hydrogen bonds. This forced structuring generally dissipates in the space of two layers of water.[57]

Vibrational spectroscopy of the OH stretch probes the hydrogen bond strength and configuration, making it an ideal tool to characterize water structure. Even-order nonlinear techniques like sum frequency generation (SFG) are in addition sensitive only to surfaces, enabling observation of interfacial water structure. A lower OH stretch frequency indicates stronger hydrogen bonding and a higher complement of hydrogen bonds, though due to the fast spectral diffusion and heterogeneity of the system, the range in OH frequencies for a single water configuration is broad.[30,58,59] Water at the water/air interface is a well-studied system with a sharp transition in density from the bulk to the vapor over only several Angstroms.[60,61] Most water molecules here share two to four hydrogen bonds,[30] with approximately one out of four molecules at the surface having a free OH.[62]

In a sum frequency generation (SFG) spectrum, the free OH appears as a sharp peak at ~3700 cm^{-1} (Figure 1.2). The free OH peak is characteristic of water at hydrophobic interfaces in general, as these surfaces do not accept or receive hydrogen bonds. Weak dipole interactions between a free OH and nonpolar surface can lower the frequency as is observed at water/CCl_4, where the resonance is redshifted by 60 cm^{-1} compared to its position for water/air.[63] At hydrophilic surfaces, the free OH peak is not present.[64] At both hydrophilic and hydrophobic materials there appears a broad band stretching from 3000 to 3600 cm^{-1} (Figure 1.2) universally attributed to the hydrogen-bonded OH resonance. Specific assignments within this band are controversial, however. For instance, the band often has humps at 3200 and 3400 cm^{-1}, which are explained by Shen, et al. as (3200 cm^{-1}) "ice-like" or double hydrogen bond donors and double acceptors (DDAA), and (3400 cm^{-1}) "liquid-like" or molecules with only three hydrogen bonds (DDA and DAA) and less symmetrical DDAA-like bonding molecules.[65] Another explanation is that the H-bonded OH band is a single homogeneous peak split by a Fermi resonance coupling

between the stretch and the bend.[66] The molecular dynamics simulations of Skinner, by contrast, describe a system of broad and overlapping contributions from water in many different hydrogen-bonding configurations.[67] New data from phase-sensitive sum frequency generation,[68] which can detect alignment of chromophores, as well as time-resolved spectroscopy of the water surface, [69-71] support the later picture of a broad, heterogeneous distribution of hydrogen bonding configurations with a general trend towards stronger hydrogen bonding with decreasing OH stretch frequency.

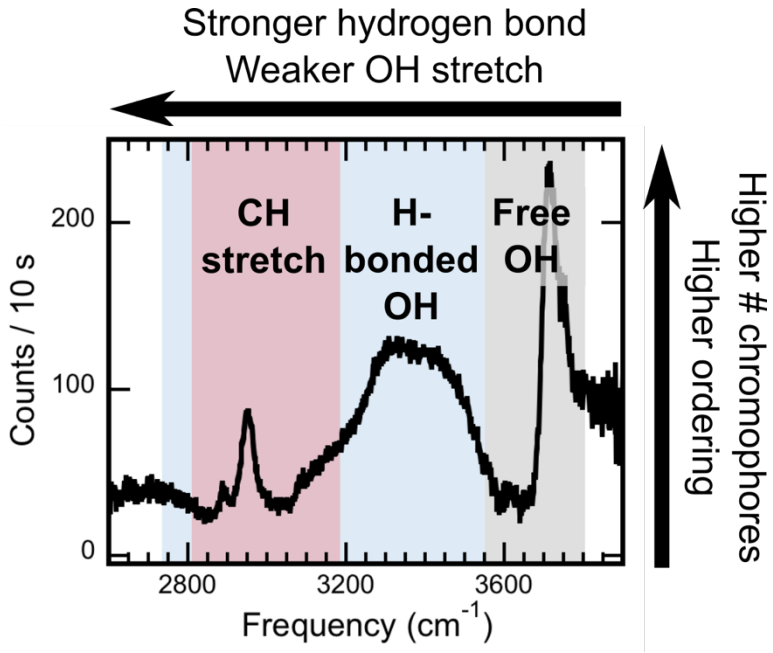

Figure 1.2 OH and CH peak assignments for an SFG spectrum of H_2O at a hydrophobic surface.

Interfacial water is also sensitive to the charge of a surface. A static electric field causes water molecules to orient according to their dipoles, aligning molecules relative to the surface plane, deepening the region of structured water, and increasing the (surface sensitive) SFG signal (Figure 1.3 a and b).[72,73] The relationship between SFG signal intensity and surface charge has been used to find the isoelectric points of silica,[74,75] alumina,[76,77] titania,[78] and CaF_2[79] by

observing the pH at which the nonlinear signal reaches a minimum. SFG spectral line shapes suggest which water hydrogen bonding environments are favored at different surface potentials; generally, the more strongly hydrogen bonded and tetrahedral configurations are enhanced by a surface potential as molecules are aligned further into the bulk.[74,79-81] Phase-sensitive methods, in addition, indicate the direction of the flip in water orientation accompanying the switch in surface charge.[82,83] Phase information is particularly useful when studying heterogeneous systems such as zwitterionic surfactants, where the water orientation is not as easily predicted,[84] and where the larger information content can make it possible to distinguish populations near different charge groups with different orientations.[85,86] Surface potentials can be screened by the addition of a salt, such as sodium chloride at silica,[81,87] or sodium salts at charged polymer or surfactant monolayers at air/water (Figure 1.3 c).[88,89] The reduction in potential experienced by water near the interface also reduces the structuring effect of the surface charge, reducing SFG signal. At an intrinsically neutral surface, ion pairs which differ in surface affinity can generate a surface potential since the difference in cation and anion density profiles results in a charge separation and therefore a surface field (Figure 1.3 d).[80,90,91] Water molecules aligned by the field give rise to a larger SFG signal.

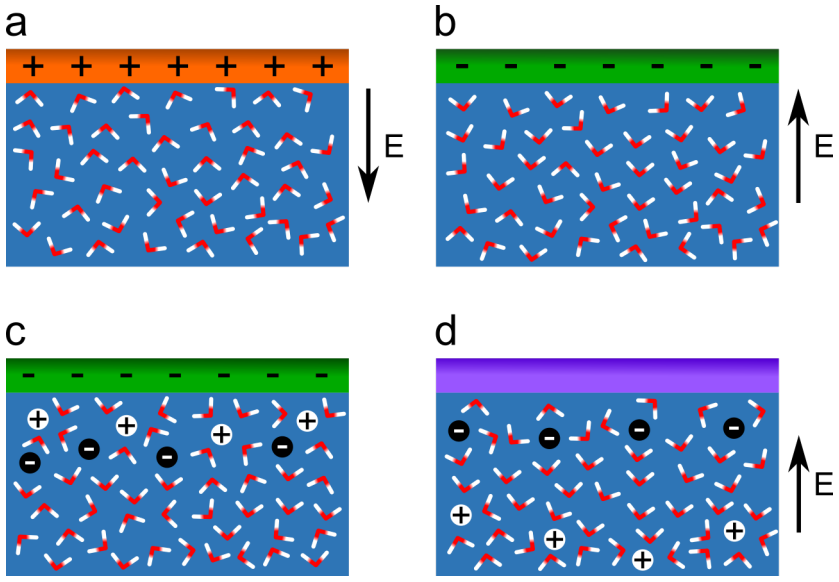

Figure 1.3 Water molecules are aligned by surface potential: (a) positively charged surface, (b) negatively charged surface, (c) screening of negatively charged surface, (d) preferential adsorption of anions at neutral surface creates electric double layer.

1.3. Sum frequency generation

The number of techniques capable of directly characterizing interfacial water at the water/air interface is limited, and of those, few can probe water at a buried interface. For instance, x-ray photoelectron spectroscopy is commonly used to characterize surfaces, but the short inelastic mean path length of the electrons which gives the technique its surface specificity limits its use to vacuum. Spectroscopies using visible and infrared light can penetrate to a buried interface as long as materials are chosen to be transparent at the relevant wavelengths. Still, techniques such as linear IR and Raman spectroscopy and IR pump/probe spectroscopy can only be used to study the water surface by careful selection of surface-rich samples and the use of signal decomposition to extract information about the surface, because otherwise signal from the bulk liquid is overwhelming.[4,48,92,93] Sum frequency signal, in contrast, can be generated at buried interfaces if transmissive materials are used, and has the advantage of being inherently surface

specific due to symmetry requirements. An SFG experiment can be designed to probe the water OH stretch mode which, as discussed above, is sensitive to water ordering, orientation, and hydrogen bonding structure.

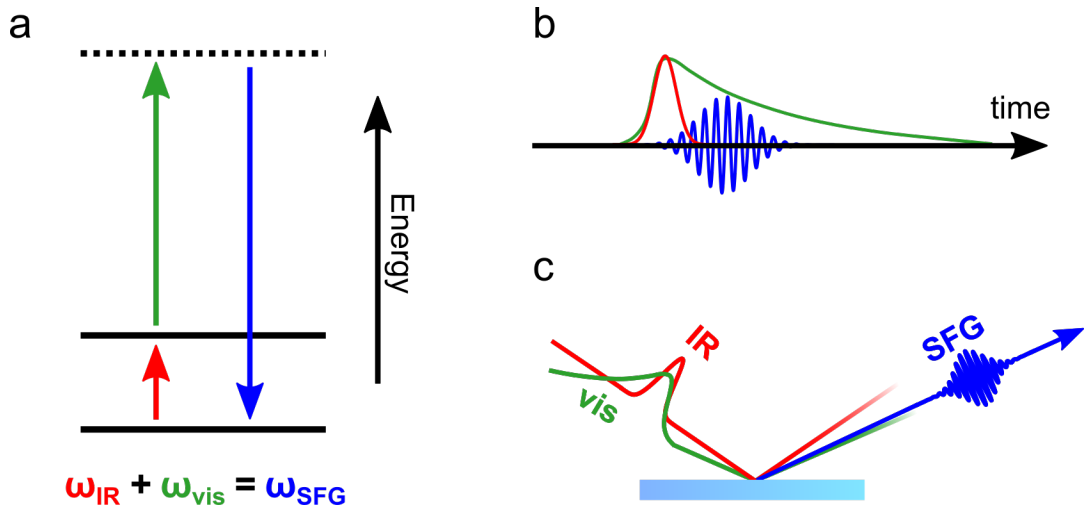

Figure 1.4 Sum frequency generation. (a) Addition of IR photon resonant with sample (red) to visible photon (green) to produce sum frequency photon (blue). (b) Short broadband IR pulse is overlapped with long narrowband visible pulse in time. (c) SFG signal is produced in reflection off the sample.

Sum frequency generation is a nonlinear optical process in which two laser pulses are overlapped on a sample to produce photons of a third frequency (ω_{SFG}), the sum of the frequencies of the two incident beams (Figure 1.4 a).[94] One of the incident beams is chosen to be resonant with a vibrational transition of interest, and is used to excite a vibrational coherence in the sample (frequency ω_{IR}). The addition of the second incident beam, usually a visible frequency (ω_{vis}), induces a Raman anti-Stokes transition from that coherence.[95] To produce an SFG signal, then, a vibrational mode must be both IR and Raman active, which in turn requires that it lack inversion symmetry. The SFG intensity of a chromophore, the molecular hyperpolarizability $\beta_{ijk}^{(2)}$, is proportional to the (Raman) polarizability tensor $\partial\alpha_{ij}/\partial Q_q$ and (IR) dipole transition moment $\partial\mu_k/\partial Q_q$:[96]

$$\beta^{(2)}_{q,ijk} \propto -\frac{\partial \alpha_{ij}}{\partial Q_q}\frac{\partial \mu_k}{\partial Q_q}. \quad \textbf{(1.1)}$$

Here the coordinates *ijk* are the molecular coordinates and the subscript q specifies the resonance. To generate SFG signal, molecular-level non-centrosymmetry is not sufficient. SFG-active chromophores must also be aligned so that $\beta^{(2)}_{ijk}$ adds across the sample. The amplitude $A_{q,xyz}$ of resonance q in sample coordinates *xyz* is proportional to the number density of chromophores N_s and the orientational average of $\beta^{(2)}_{ijk}$ rotated from the polar molecular coordinates (θ, ϕ, ψ) to the rectalinear sample coordinates (x, y, z) by Euler transformation matrices R.[97]

$$A_{q,xyz} = N_s \sum_{ijk} \langle R_{xi} R_{yj} R_{zk} \rangle \beta^{(2)}_{ijk} \quad \textbf{(1.2)}$$

Interfacial water is SFG active because the OH stretch is both IR and Raman active (molecular non-centrosymmetry), and the anisotropic environment produced by an interface orders water molecules along the plane of the interface (macroscopic non-centrosymmetry). Below this surface region, where the isotropic symmetry of bulk water is recovered, negligible signal is generated.[98-100] Charged surfaces are an important exception to this rule. A surface potential creates a third electric field E_0 which interacts with the two transient electric fields of the IR and visible incident pulses to produce a bulk-allowed nonlinear signal from water molecules within E_0. This third-order signal is linear in E_0 and can be larger than the second-order SFG response.[81]

In the Petersen laboratory, IR and visible pulses are overlapped in time (Figure 1.4 b) and space on the sample, emitting sum frequency signal in reflection (Figure 1.4 c). The IR and visible

beams travel along one plane perpendicular to the substrate, and the SFG beam is emitted along the same plane at an angle dictated by conservation of momentum. A combination of short, broadband IR pulses (80 fs, 230 cm^{-1}) and long, narrowband visible pulses (2 ps, 10 cm^{-1}) allows a wide window of vibrational resonances to be probed in each laser shot due to the large bandwidth of the IR pulses, while also having the sharp frequency resolution determined by the narrow frequency width of the visible source. The intensity of the SFG signal, I_{SFG}, is proportional to the intensities of the visible and IR beams, I_{vis} and I_{IR}, and the square of the second-order nonlinear susceptibility, $\chi^{(2)}$.

$$I_{\mathrm{SFG}} \propto |\chi^{(2)}|^2 I_{\mathrm{vis}} I_{\mathrm{IR}} \tag{1.3}$$

The SFG susceptibility has a nonresonant $\chi^{(2)}_{\mathrm{NR}}$ component, and resonant $\chi^{(2)}_q$ components, one for each resonance q. At IR frequencies ω_{IR} near SFG active modes of frequency ω_q, $\chi^{(2)}_q$ is resonantly enhanced. Peaks with purely homogeneous broadening are Lorentzian in shape with dampening constant Γ_q and amplitude A_q.

$$\chi^{(2)} = \chi^{(2)}_{\mathrm{NR}} + \sum_q \frac{A_q}{\omega_q - \omega_{\mathrm{IR}} - i\Gamma_q} \tag{1.4}$$

$I_{\mathrm{SFG}}$is uniformly positive in sign due to the squaring of $\chi^{(2)}$ (Equation 1.3), even though A_q may be either positive or negative depending on the orientation of the chromophore and the sign of $\beta^{(2)}$. Nonresonant $\chi^{(2)}_{\mathrm{NR}}$ signal also interferes with the resonant components, distorting peak shapes. Phase-sensitive or heterodyned SFG is an elaboration on standard "homodyned" SFG described above, which removes these ambiguities in spectral interpretation.[82,83] The experimental setup of both is as follows.

The oscillator (Micra, Coherent) generates ultrafast pulses (800 nm, 80 MHz, 75 nm full width at half maximum (FWHM), 440 mW) which are directed into the amplifier (Legend Elite Duo, Coherent) to produce more intense pulses with a lower repetition rate (793 nm, 1 kHz, 38 nm FWHM, 25 fs). The output of the amplifier is split, with 1 mJ spectrally narrowed to become the visible SFG pulse, and 3 mJ converted to broadband IR pulses. The 1 mJ (visible) fraction is passed through an etalon filter and then a narrow bandpass filter, narrowing the peak in frequency to 10 cm^{-1} and giving rise to the temporal profile shown in Figure 1.4 b which is characterized by a sharp leading edge and long tail. The 3 mJ (IR) fraction is routed through an optical parametric amplifier (OperA Solo, Coherent) which, through optical parametric amplification and difference frequency generation, transforms the 794 nm input into tunable (2.6-20 μm) infrared pulses (~230 cm^{-1}, 70 fs). Both the visible and IR beams are then reflected off mirrors mounted on motorized translation stages to finely control the path lengths and therefore the timing of the pulses. IR and visible polarization is controlled with half-wave plates and polarizers.

Standard and heterodyned SFG are performed using the same system (Figure 1.5) with minor adjustments.[101] Elements specific to heterodyned SFG are labelled in orange, and are absent when collecting standard SFG spectra. To characterize a sample using standard SFG, the visible and IR beams are focused on the sample surface with parabolic mirror P2 and the pulses are timed to arrive at the sample simultaneously. Emitted SFG signal (blue) is focused into the monochromator (Princeton Instruments) to be dispersed by a grating onto a CCD camera (Spec-10, Princeton Instruments, 1340 × 400 pixels). As the IR pulse is wide in frequency, the image captured by the CCD camera is a spectrum. A nonresonant sample such as gold generates a signal like the blue trace (Figure 1.5). While $\chi_{\mathrm{NR}}^{(2)}$ is not resonant and therefore constant with

frequency, the observed signal is convoluted by the intensity of the IR pulse, which is frequency dependent. Spectra are collected from purely nonresonant samples to normalize data the IR power envelope.

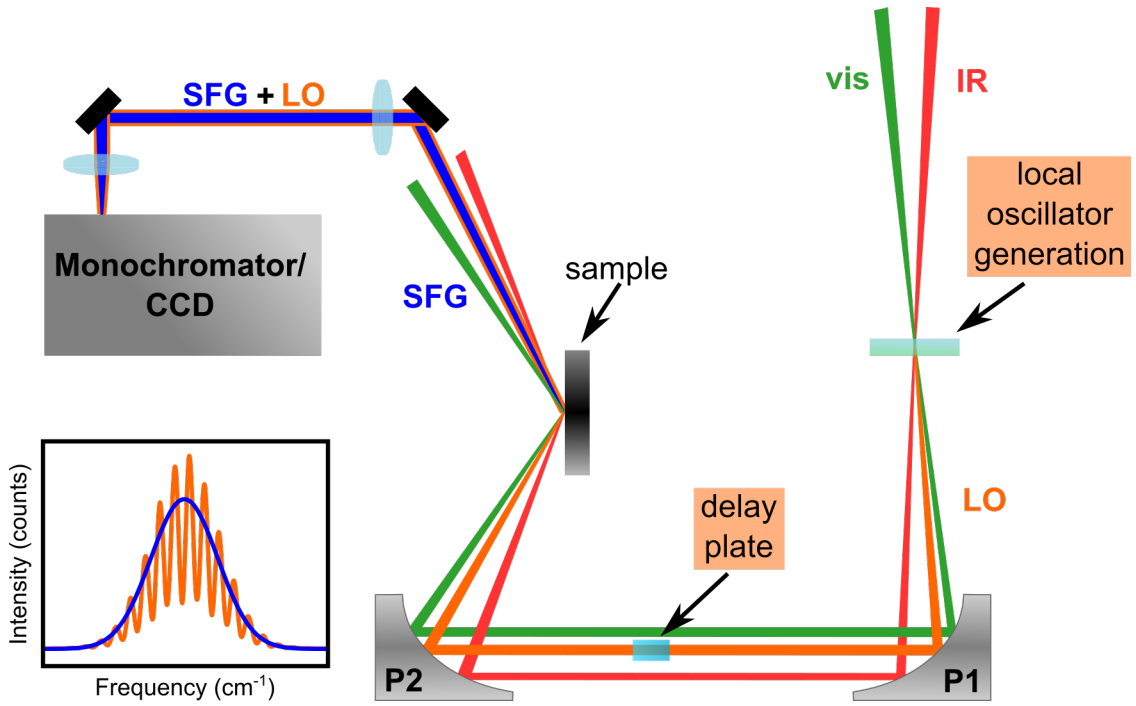

Figure 1.5 Standard and heterodyned SFG setup. For collection of standard SFG, the bulk local oscillator medium is absent, and local oscillator signal (LO) is not produced, generating signal shown in blue. For heterodyned SFG, LO signal is overlapped with SFG signal, producing interference fringes in signal (orange). Parabolic mirrors collimate (P1) and focus (P2) visible, IR and LO.

To collect heterodyned SFG, z-cut quartz or ZnO on CaF_2 is added in the first focus of the visible and IR beams (Figure 1.5, right) to generate a local oscillator (LO) field E_{LO} with frequency ω_{SFG}, shown in orange. The LO signal is then passed through a delay plate which retards the pulse relative to the visible and IR pulses by a small time Δt. As with standard SFG, the SFG signal is emitted from the surface of the sample, but due to the optical geometry, the SFG signal is overlapped with the LO reflecting off the sample. The small time difference between the LO and SFG introduced by the delay plate causes them to interfere (orange trace).

The real and imaginary components of $\chi^{(2)}$ can be recovered using the phase information in the interference fringes. While in standard SFG this is lost as the SFG electric field E_{SFG} is squared,

$$I_{SFG} \propto |E_{\mathrm{SFG}}|^2 \tag{1.5}$$

the cross terms between E_{SFG} and E_{LO} for the heterodyned SFG intensity $I_{\mathrm{SFG,het}}$ retain the phase.[82]

$$I_{\mathrm{SFG,het}} \propto |E_{\mathrm{LO}}|^2 + |E_{\mathrm{SFG}}|^2 + E_{\mathrm{LO}}E_{\mathrm{SFG}}^{*}e^{-i\omega_{\mathrm{SFG}}\Delta t} + E_{\mathrm{LO}}^{*}E_{\mathrm{SFG}}e^{+i\omega_{\mathrm{SFG}}\Delta t} \tag{1.6}$$

From this the imaginary component $Im\chi^{(2)}$ can be calculated, which does not include $\chi_{\mathrm{NR}}^{(2)}$ (this is in the real part), and which does indicate the sign of A_q.[100] Knowing the sign of A_q for each resonance, the absolute (up/down) orientation of the corresponding chromophore can be determined.

$$\mathrm{Im}\chi^{(2)} = -\sum_{q} \frac{A_q \Gamma_q}{(\omega_{\mathrm{IR}} - \omega_q)^2 + \Gamma_q^2} \tag{1.7}$$

1.4. SFG probe depth

In the electric dipole approximation, the second order nonlinear polarizability $\chi^{(2)}$ is zero in material with inversion symmetry.[102,103] This leads to the rule that sum frequency is generated only where inversion symmetry is broken, such as at an interface, and is often a reasonable approximation. Simulations of SFG spectra for liquid interfaces with very few exceptions[104,105] include only the electric-dipole allowed $\chi^{(2)}$. The water/air interface is a frequent subject of calculations, and these provide structural details about the interface which cannot be extracted from experimental data. A general picture emerges that SFG spectral density,[60,106] vibrational

coupling,[107] water density,[59,106-110] hydrogen-bonding complement,[59,60,109] and water orientation[60,109] return to bulk values within about 5 Å of the Gibbs dividing surface. The non-hydrogen bonded "free" OH is localized to the first water layer, while the remaining configurations are mainly confined to the first two layers.[59,106,110] The depth of anisotropic water orientation at the air interface is extended by ion pairs which create an electrical double layer and align water molecules, such as 1.2 M $(NH_4)_2SO_4$, which increased the depth to ~20 Å,[80] 2.1 M NaI and 1.1 M HCl, to 15 Å and 10 Å respectively,[111] and 1.2 M NaI, to > 6 Å.[61] Part of the sum frequency signal at these interfaces comes from isotropically-oriented water molecules as the addition of the third, static, electric field E_0 from the ion arrangement generates a bulk-allowed third-order signal. The combined second- and third- order polarization ($P^{(2)}$ and $P^{(3)}$) is given by[72,112,113]

$$P^{(2)} + P^{(3)} = N_2\langle\beta^{(2)}\rangle E_1 E_2 + N_3 \left(\langle\beta^{(3)}\rangle + \frac{\mu_{\text{water}}\langle\beta^{(2)}\rangle}{bkT}\right) E_1 E_2 \int_0^\infty E_0(z)dz \,. \qquad \textbf{(1.8)}$$

The first term in Equation 1.8 gives the second-order response, which depends on the number of water molecules with noncentrosymmetric orientation N_2, the orientational average of the second order molecular hyperpolarizability $\beta^{(2)}$, and the electric fields E_1 and E_2 from the incident pulses. This is the standard response $\chi^{(2)}E_1E_2$ generated at a neutral surface. The second term gives the third-order response, and is linear in the number of molecules N_3 experiencing the field E_0, which varies with depth from the interface, *z*. In the Gouy-Chapman model, the surface potential Ψ_0 from the integral of E_0 decays exponentially with distance from the surface as $e^{-\kappa z}$, where $1/\kappa$ is the Debye (screening) length.[114] For the phosphate buffers discussed in Chapter 5 with ionic strengths of 166 mM and 25 mM, the Debye length is 0.7 nm and 2 nm, respectively.

There is a third-order hyperpolarizability $\beta^{(3)}$ component, as well as a second-order component dependent on the permanent dipole moment of the water molecules μ_{water}, a constant b determined by the $\beta^{(2)}$ element, and kT. This treatment is still within the electric dipole approximation, and has been used to correlate surface potential at the water interface with water second harmonic or sum frequency generation intensity.[12,113,115-118] For instance, the surface potential created by the adsorption of different anions to a neutral polymer film at the water/air interface followed the ion surface activity predicted by the Hofmeister series.[119]

Higher order terms in $\chi^{(2)}$ can result in significant bulk SFG signal, but for many samples and experimental geometries it appears to be negligible. Expanding to the electric quadrupole and magnetic dipole level, the second-order polarization has a surface component $P_S^{(2)}$ as in the electric dipole approximation, with a corresponding surface nonlinear susceptibility $\chi_S^{(2)}$,

$$P_S^{(2)} = \chi_S^{(2)} E_1 E_2 \tag{1.9}$$

as well as a bulk component $P_B^{(2)}$ with bulk electric dipole polarization $P_{B,D}^{(2)}$, electric quadrupole polarization $Q^{(2)}$, and magnetization $M^{(2)}$ contributions.[100,120] Here k_i are wave vectors and ω_i are frequencies, with IR and visible beams indicated by a subscript of 1 and 2, and sum frequency with no subscript.

$$P_B^{(2)}(\omega, k) = P_{B,D}^{(2)}(\omega, k) - ik \cdot Q^{(2)}(\omega, k) - \frac{c}{\omega} k \times M^{(2)}(\omega, k) + \cdots \tag{1.10}$$

The electric dipole, electric quadrupole, and magnetic dipole $\chi^{(2)}$ associated with these polarization terms can be grouped into one surface $\chi_S^{(2)}$ and two bulk terms $\chi_{BS}^{(2)}$ and $\chi_{BB}^{(2)}$.

$$\chi^{(2)}_{S,\text{eff}}(k_1, k_2, k) = \chi^{(2)}_S + \chi^{(2)}_{BS}(k_1, k_2, k) + \frac{\chi^{(2)}_{BB}}{-i|\Delta k|} \quad \textbf{(1.11)}$$

While $\chi^{(2)}_{BB}$ can be determined in experiment by varying the coherence length $l_c = 1/|k_z - k_{1,z} - k_{2.z}| = 1/\Delta k$, $\chi^{(2)}_S$ and $\chi^{(2)}_{BS}$ are not separable. This is because the relative strength of the dipole $\chi^{(2)}_S$ and quadrupole $\chi^{(2)}_{BS}$ responses depends on where the dividing surface is drawn, and thus how the charges are grouped.[99,121] Still, it has been possible to estimate the size of the bulk signal. One strategy is to compare sum frequency generated in reflection to transmission, as the coherence length is much longer in transmission, leading to a larger bulk signal.[98,99,122] It was found that at most 10% of the signal in the reflection geometry came from the bulk for methanol/air and polyethylene/air. As for the water/air system, application of a stearyl alcohol film to the water surface removed the non-hydrogen-bonded "free" OH peak as well as some of the higher frequency H-bonded OH intensity,[64] suggesting sensitivity to only the topmost water layers. A comparison of water/air SFG spectra from different groups showed remarkable consistency after corrections were made for differences in beam angles and normalization method.[123] If multipolar contributions were significant in water/air spectra, the difference in coherence length accompanying the difference in beam angles would limit reproducibility. Finally, a large bulk response would be immediately noticeable for samples with inherently fine surface structures such as water at phospholipid membranes,[84] where signal from the thin layer of oriented water molecules could be easily overwhelmed.

1.5. Self-Assembled Monolayers

Self-assembled monolayers are films composed of molecules which spontaneously arrange themselves roughly normal to a surface and parallel to their neighbors (Figure 1.6). At the end facing away from the substrate is the terminal group, which largely determines the surface energy and the nature of surface interactions. The surface of a monolayer may be decorated with a wide range of functional groups and macromolecules, ranging from small methyl, alcohol, and cyanide moieties, to polymers, to proteins.[124-127] Connecting the head and the tail is a spacer group, usually an alkane chain. Its function is central to the self-assembly process, as the van der Waals attraction (1-2 kCal/mol/methylene group) between chains drives monomers to pack together in orderly arrays.[124,128-131] For chains of sufficient length, the resulting monolayer can resemble a two-dimensional crystal.[132-135] A head group selectively binds monomers to the substrate, anchoring the molecule to the surface or cross linking to head groups of other monomers.[136] As the substrate/anchor interaction is specific, binding groups are compatible with a limited number of substrates. Commonly-used binding group and substrate combinations are thiol/Au,[126] amphiphile/water (Langmuir film),[137] and chlorosilane/oxide.[138]

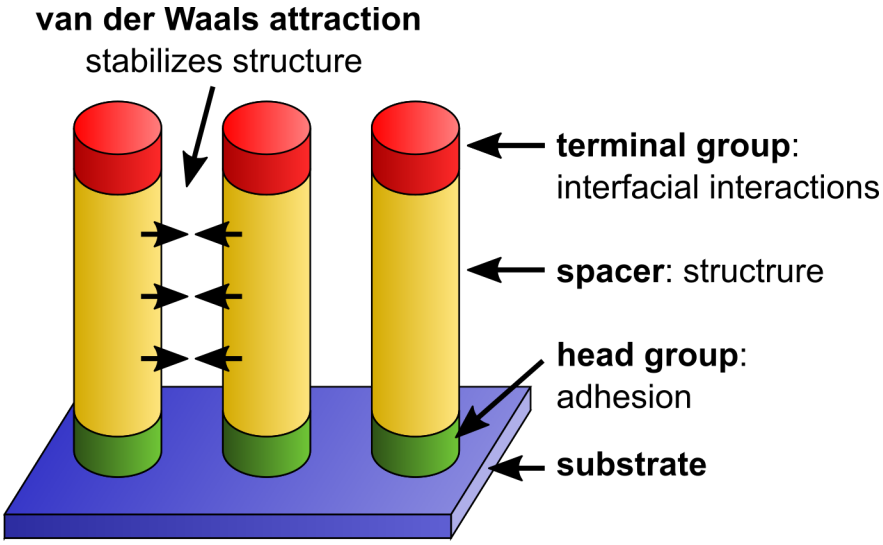

Figure 1.6 Structure of a self-assembled monolayer.

Self-assembled monolayers are a highly tunable and ordered platform for studying water structure at surfaces with different chemical and textural properties. As the motivation for this project is to probe the buried water/monolayer interface, the substrate must be transparent in the IR, visible, and SFG frequencies. Chlorosilane/oxide monolayers are ideal because they can be applied to visible-transparent materials like silica and alumina. While silica absorbs between 3500-3700 cm^{-1} and below 2500 cm^{-1}, a chlorosilane compatible and IR/vis transparent substrate was fabricated by depositing a thin layer of silica on CaF_2. Chlorosilane monolayers are chemically and thermally robust due to the strong siloxane bonds formed to the substrate and between monomers.[138] The highly reactive trichlorosilane groups which create these bonds are also incompatible with many functionalities of interest, including alcohols and carboxylic acids. Several post-deposition modification strategies have been developed to bypass this limitation: nucleophilic substitution,[139] oxidation,[140] cycloaddition,[141] photodecomposition,[142] and various others.[125,143] However, most reactions rates are much smaller at surfaces than in the bulk due to steric constraints, and decrease with increasing monolayer packing.[144-147] The cycloaddition and photodecomposition schemes fare better here, but introduce moieties that are larger than the

footprint of an alkane chain and either react incompletely or interfere with dense monomer packing. A new solution is needed to expand the chlorosilane/oxide monolayer repertoire to include hydrophilic moieties without sacrificing monolayer density and homogeneity.

1.6. Research Overview

The following chapters describe the development of tools to study water at interfaces, the creation of tunable surfaces to observe interfacial water, and the interaction of water, ions, and surfaces. Chapter 2 details a system for controlling the environment on the laser table, an accessory for amplification of transmission IR signal, a chlorosilane-compatible substrate allowing the buried water interface to be probed by SFG, a mounting system for those samples, and a tool for choosing optimal SFG beam angles and substrate geometries. In Chapter 3, the characterization of a series of textured hydrophobic monolayers is presented, along with observations of the weak interaction between the monolayers and water. The exploration of a heat deprotection strategy for preparing densely-packed hydrophilic monolayers is discussed in Chapter 4. Then, in Chapter 5, a collaborative project investigating water structure at anti-fouling films is reviewed, where biological buffers are found to generate an electrical double layer. Lastly, a new method of determining the composition of large brush polymers is described.

References

(1) Faizal, M.; Rafiuddin Ahmed, M. On the Ocean Heat Budget and Ocean Thermal Energy Conversion. *Int. J. Energy Res.* **2011**, *35* (13), 1119–1144.

(2) Sawada, K.; Handa, N. Variability of the Path of the Kuroshio Ocean Current Over the Past 25,000 Years. *Nature* **1998**, *392* (6676), 592–595.

(3) Armour, K. C.; Marshall, J.; Scott, J. R.; Donohoe, A.; Newsom, E. R. Southern Ocean Warming Delayed by Circumpolar Upwelling and Equatorward Transport. *Nature Geoscience* **2016**, *9* (7), 549–554.

(4) Davis, J. G.; Zukowski, S. R.; Rankin, B. M.; Ben-Amotz, D. Influence of a Neighboring Charged Group on Hydrophobic Hydration Shell Structure. *J Phys Chem B* **2015**, *119* (29), 9417–9422.

(5) Smith, J. D.; Saykally, R. J.; Geissler, P. L. The Effects of Dissolved Halide Anions on Hydrogen Bonding in Liquid Water. *Journal of the American Chemical Society* **2007**, *129* (45), 13847–13856.

(6) Chen, Y.; Okur, H. I.; Gomopoulos, N.; Macias-Romero, C.; Cremer, P. S.; Petersen, P. B.; Tocci, G.; Wilkins, D. M.; Liang, C.; Ceriotti, M.; et al. Electrolytes Induce Long-Range Orientational Order and Free Energy Changes in the H-Bond Network of Bulk Water. *Sci Adv* **2016**, *2* (4), e1501891–e1501891.

(7) Perera, P. N.; Fega, K. R.; Lawrence, C.; Sundstrom, E. J.; Tomlinson-Phillips, J.; Ben-Amotz, D. Observation of Water Dangling OH Bonds Around Dissolved Nonpolar Groups. *Proc. Natl. Acad. Sci. U.S.A.* **2009**, *106* (30), 12230–12234.

(8) Vaida, V. Perspective: Water Cluster Mediated Atmospheric Chemistry. *The Journal of Chemical Physics* **2011**, *135* (2), 020901.

(9) Ault, A. P.; Zhao, D.; Ebben, C. J.; Tauber, M. J.; Geiger, F. M.; Prather, K. A.; Grassian, V. H. Raman Microspectroscopy and Vibrational Sum Frequency Generation Spectroscopy as Probes of the Bulk and Surface Compositions of Size-Resolved Sea Spray Aerosol Particles. *Phys. Chem. Chem. Phys.* **2013**, *15* (17), 6206–6214.

(10) Karhan, K.; Khaliullin, R. Z.; Kühne, T. D. On the Role of Interfacial Hydrogen Bonds in "on-Water" Catalysis. *Journal of Chemical Physics* **2014**, *141* (22), 22D528.

(11) Jordan, D. S.; Saslow, S. A.; Geiger, F. M. Exponential Sensitivity and Speciation of Al(III), Sc(III), Y(III), La(III), and Gd(III) at Fused Silica/Water Interfaces. *J. Phys. Chem. A* **2011**, *115* (50), 14438–14445.

(12) Gomez, S. A. S.; Geiger, F. M. Precipitates of Al(III), Sc(III), and La(III) at the Muscovite–Water Interface. *The Journal of Physical Chemistry A* **2014**, *118* (46), 10974–10981.

(13) Hayes, P. L.; Malin, J. N.; Konek, C. T.; Geiger, F. M. Interaction of Nitrate, Barium, Strontium and Cadmium Ions with Fused Quartz/Water Interfaces Studied by Second Harmonic Generation. *J. Phys. Chem. A* **2008**, *112* (4), 660–668.

(14) Chandler, D. Interfaces and the Driving Force of Hydrophobic Assembly. *Nature* **2005**, *437* (7059), 640–647.

(15) Cameron, I. L.; Fullerton, G. D. Non-Bulk-Like Water on Cellular Interfaces. In *Water and the Cell*; Springer Netherlands, 2006; pp 315–324.

(16) Heyden, M. Resolving Anisotropic Distributions of Correlated Vibrational Motion in Protein Hydration Water. *The Journal of Chemical Physics* **2014**, *141* (22), 22D509.

(17) Grossman, M.; Born, B.; Heyden, M.; Tworowski, D.; Fields, G. B.; Sagi, I.; Havenith, M. Correlated Structural Kinetics and Retarded Solvent Dynamics at the Metalloprotease Active Site. *Nat. Struct. Mol. Biol.* **2011**, *18* (10), 1102–1108.

(18) Heyden, M.; Bründermann, E.; Heugen, U.; Niehues, G.; Leitner, D. M.; Havenith, M. Long-Range Influence of Carbohydrates on the Solvation Dynamics of Water--Answers From Terahertz Absorption Measurements and Molecular Modeling Simulations. *J. Am. Chem. Soc* **2008**, *130* (17), 5773–5779.

(19) King, J. T.; Arthur, E. J.; Brooks, C. L.; Kubarych, K. J. Crowding Induced Collective Hydration of Biological Macromolecules Over Extended Distances. *J. Am. Chem. Soc* **2013**.

(20) Callow, M. E.; Callow, J. E. Marine Biofouling: a Sticky Problem. *Biologist (London)* **2002**, *49* (1), 10–14.

(21) Lindholdt, A.; Dam-Johansen, K.; Olsen, S. M.; Yebra, D. M.; Kiil, S. Effects of Biofouling Development on Drag Forces of Hull Coatings for Ocean-Going Ships: a Review. *J Coat Technol Res* **2015**, *12* (3), 415–444.

(22) Zhang, H.; Chiao, M. Anti-Fouling Coatings of Poly(Dimethylsiloxane) Devices for Biological and Biomedical Applications. *J. Med. Biol. Eng.* **2015**, *35* (2), 143–155.

(23) Drekonja, D. M.; Kuskowski, M. A.; Wilt, T. J.; Johnson, J. R. Antimicrobial Urinary Catheters: a Systematic Review. *Expert Review of Medical Devices* **2008**, *5* (4), 495–506.

(24) Sousa, C.; Henriques, M.; Oliveira, R. Mini-Review: Antimicrobial Central Venous Catheters – Recent Advances and Strategies. *Biofouling* **2011**, *27* (6), 609–620.

(25) Grimaldi, J.; Imbrogno, J.; Kilduff, J. C.; Belfort, G. New Class of Synthetic Membranes: Organophilic Pervaporation Brushes for Organics Recovery. *Chem. Mater* **2015**, *27* (11), 4142–4148.

(26) Khalid, A.; Al-Juhani, A. A.; Al-Hamouz, O. C.; Laoui, T.; Khan, Z.; Atieh, M. A. Preparation and Properties of Nanocomposite Polysulfone/Multi-Walled Carbon Nanotubes Membranes for Desalination. *Desalination* **2015**, *367*, 134–144.

(27) Ostuni, E.; Chapman, R. G.; Holmlin, R. E.; Takayama, S.; Whitesides, G. M. A Survey of Structure−Property Relationships of Surfaces That Resist the Adsorption of Protein. *Langmuir* **2001**, *17* (18), 5605–5620.

(28) Banerjee, I.; Pangule, R. C.; Kane, R. S. Antifouling Coatings: Recent Developments in the Design of Surfaces That Prevent Fouling by Proteins, Bacteria, and Marine Organisms. *Adv. Mater. Weinheim* **2011**, *23* (6), 690–718.

(29) Katsikogianni, M.; Missirlis, Y. F. Concise Review of Mechanisms of Bacterial Adhesion to Biomaterials and of Techniques Used in Estimating Bacteria-Material Interactions. *Eur Cell Mater* **2004**, *8*, 37–57.

(30) Tainter, C. J.; Ni, Y.; Shi, L.; Skinner, J. L. Hydrogen Bonding and OH-Stretch Spectroscopy in Water: Hexamer (Cage), Liquid Surface, Liquid, and Ice. *The Journal of Physical Chemistry Letters* **2013**, *4* (1), 12–17.

(31) Steiner, T. The Hydrogen Bond in the Solid State. *Angewandte Chemie International Edition in English* **2002**, *41* (1), 48–76.

(32) Novak, A. Hydrogen Bonding in Solids Correlation of Spectroscopic and Crystallographic Data; Springer Berlin Heidelberg, 1974; pp 177–216.

(33) Rey, R.; Møller, K. B.; Hynes, J. T. Hydrogen Bond Dynamics in Water and Ultrafast Infrared Spectroscopy. *J. Phys. Chem. A* **2002**, *106* (50), 11993–11996.

(34) Ashihara, S.; Huse, N.; Espagne, A.; Nibbering, E. T. J.; Elsaesser, T. Ultrafast Structural Dynamics of Water Induced by Dissipation of Vibrational Energy. *J. Phys. Chem. A* **2007**, *111* (5), 743–746.

(35) Ashihara, S.; Huse, N.; Espagne, A.; Nibbering, E. T. J.; Elsaesser, T. Vibrational Couplings and Ultrafast Relaxation of the O–H Bending Mode in Liquid H2O. *Chemical physics letters* **2006**, *424* (1-3), 66–70.

(36) Ramasesha, K.; De Marco, L.; Mandal, A.; Tokmakoff, A. Water Vibrations Have Strongly Mixed Intra- and Intermolecular Character. *Nature Chem* **2013**, *5* (11), 935–940.

(37) Woutersen, S.; Bakker, H. J. Resonant Intermolecular Transfer of Vibrational Energy in Liquid Water. *Nature* **1999**, *402* (6761), 507–509.

(38) Fecko, C. J.; Loparo, J. J.; Roberts, S. T.; Tokmakoff, A. Local Hydrogen Bonding Dynamics and Collective Reorganization in Water: Ultrafast Infrared Spectroscopy of HOD/D(2)O. *Journal of Chemical Physics* **2005**, *122* (5), 54506.

(39) Cowan, M. L.; Bruner, B. D.; Huse, N.; Dwyer, J. R.; Chugh, B.; Nibbering, E. T. J.; Elsaesser, T.; Miller, R. J. D. Ultrafast Memory Loss and Energy Redistribution in the Hydrogen Bond Network of Liquid H2O. *Nature* **2005**, *434* (7030), 199–202.

(40) Nicodemus, R. A.; Corcelli, S. A.; Skinner, J. L.; Tokmakoff, A. Collective Hydrogen Bond Reorganization in Water Studied with Temperature-Dependent Ultrafast Infrared Spectroscopy. *J Phys Chem B* **2011**, *115* (18), 5604–5616.

(41) Loparo, J.; Roberts, S.; Tokmakoff, A. Multidimensional infrared spectroscopy of water. I. Vibrational dynamics in two-dimensional IR line shapes. *The Journal of Chemical Physics* **2006**.

(42) Kraemer, D.; Cowan, M. L.; Paarmann, A.; Huse, N.; Nibbering, E. T. J.; Elsaesser, T.; Miller, R. J. D. Temperature Dependence of the Two-Dimensional Infrared Spectrum of Liquid H2O. *PNAS* **2008**, *105* (2), 437–442.

(43) Perakis, F.; Marco, L. D.; Shalit, A.; Tang, F.; Kann, Z. R.; Kühne, T. D.; Torre, R.; Bonn, M.; Nagata, Y. Vibrational Spectroscopy and Dynamics of Water. *Chem. Rev.* **2016**, *116* (13), 7590–7607.

(44) Laage, D.; Hynes, J. T. On the Molecular Mechanism of Water Reorientation. *J Phys Chem B* **2008**, *112* (45), 14230–14242.

(45) Bakker, H. J.; Rezus, Y. L. A.; Timmer, R. L. A. Molecular Reorientation of Liquid Water Studied with Femtosecond Midinfrared Spectroscopy. *J. Phys. Chem. A* **2008**, *112* (46), 11523–11534.

(46) Moilanen, D. E.; Levinger, N. E.; Spry, D. B.; Fayer, M. D. Confinement or the Nature of the Interface? Dynamics of Nanoscopic Water. *Journal of the American Chemical Society* **2007**, *129* (46), 14311–14318.

(47) Pieniazek, P. A.; Lin, Y.-S.; Chowdhary, J.; Ladanyi, B. M.; Skinner, J. L. Vibrational Spectroscopy and Dynamics of Water Confined Inside Reverse Micelles. *J Phys Chem B* **2009**, *113* (45), 15017–15028.

(48) Moilanen, D. E.; Fenn, E. E.; Wong, D.; Fayer, M. D. Geometry and Nanolength Scales Versus Interface Interactions: Water Dynamics in AOT Lamellar Structures and Reverse Micelles. *Journal of the American Chemical Society* **2009**, *131* (23), 8318–8328.

(49) van der Post, S. T.; Hsieh, C.-S.; Okuno, M.; Nagata, Y.; Bakker, H. J.; Bonn, M.; Hunger, J. Strong Frequency Dependence of Vibrational Relaxation in Bulk and Surface Water Reveals Sub-Picosecond Structural Heterogeneity. *Nat Commun* **2015**, *6 SP* -, 8384.

(50) Hsieh, C.-S.; Campen, R. K.; Okuno, M.; Backus, E. H. G.; Nagata, Y.; Bonn, M. Mechanism of Vibrational Energy Dissipation of Free OH Groups at the Air-Water Interface. *Proc. Natl. Acad. Sci. U.S.A.* **2013**, *110* (47), 18780–18785.

(51) Zhang, Z.; Piatkowski, L.; Bakker, H. J.; Bonn, M. Ultrafast Vibrational Energy Transfer at the Water/Air Interface Revealed by Two-Dimensional Surface Vibrational Spectroscopy. *Nature Chem* **2011**, *3* (11), 888–893.

(52) Ni, Y.; Gruenbaum, S. M.; Skinner, J. L. Slow Hydrogen-Bond Switching Dynamics at the Water Surface Revealed by Theoretical Two-Dimensional Sum-Frequency Spectroscopy. *Proc. Natl. Acad. Sci. U.S.A.* **2013**, *110* (6), 1992–1998.

(53) Hsieh, C.-S.; Campen, R.; Vila Verde, A.; Bolhuis, P.; Nienhuys, H.-K.; Bonn, M. Ultrafast Reorientation of Dangling OH Groups at the Air-Water Interface Using Femtosecond Vibrational Spectroscopy. *Physical Review Letters* **2011**, *107* (11), 116102.

(54) Stiopkin, I. V.; Weeraman, C.; Pieniazek, P. A.; Shalhout, F. Y.; Skinner, J. L.; Benderskii, A. V. Hydrogen Bonding at the Water Surface Revealed by Isotopic Dilution Spectroscopy. *Nature* **2011**, *474* (7350), 192–195.

(55) Roy, S.; Gruenbaum, S. M.; Skinner, J. L. Theoretical Vibrational Sum-Frequency Generation Spectroscopy of Water Near Lipid and Surfactant Monolayer Interfaces. *The Journal of Chemical Physics* **2014**, *141* (18), 18C502.

(56) Limmer, D. T.; Willard, A. P.; Madden, P.; Chandler, D. Hydration of Metal Surfaces Can Be Dynamically Heterogeneous and Hydrophobic. *PNAS* **2013**, *110* (11), 4200–4205.

(57) Bonn, M.; Nagata, Y.; Backus, E. H. G. Molecular Structure and Dynamics of Water at the Water-Air Interface Studied with Surface-Specific Vibrational Spectroscopy. *Angewandte Chemie International Edition in English* **2015**, *54* (19), 5560–5576.

(58) Lawrence, C. P.; Skinner, J. L. Vibrational Spectroscopy of HOD in Liquid D2O. VII. Temperature and Frequency Dependence of the OH Stretch Lifetime. *Journal of Chemical Physics* **2003**, *119* (7), 3840–3848.

(59) Pieniazek, P. A.; Tainter, C. J.; Skinner, J. L. Interpretation of the Water Surface Vibrational Sum-Frequency Spectrum. *The Journal of Chemical Physics* **2011**, *135* (4), 044701.

(60) Auer, B. M.; Skinner, J. L. Vibrational Sum-Frequency Spectroscopy of the Liquid/Vapor Interface for Dilute HOD in D2O. *Journal of Chemical Physics* **2008**, *129* (21), 214705.

(61) Brown, E. C.; Mucha, M.; Jungwirth, P.; Tobias, D. J. Structure and Vibrational Spectroscopy of Salt Water/Air Interfaces: Predictions From Classical Molecular Dynamics Simulations. *J Phys Chem B* **2005**, *109* (16), 7934–7940.

(62) Du, Q.; Freysz, E.; Shen, Y. R. Surface Vibrational Spectroscopic Studies of Hydrogen Bonding and Hydrophobicity. *Science* **1994**, *264* (5160), 826–828.

(63) Hopkins, A. J.; McFearin, C. L.; Richmond, G. L. SAMs Under Water: the Impact of Ions on the Behavior of Water at Soft Hydrophobic Surfaces. *The Journal of Physical Chemistry C* **2011**, *115* (22), 11192–11203.

(64) Du, Q.; Superfine, R.; Freysz, E.; Shen, Y. Vibrational Spectroscopy of Water at the Vapor/Water Interface. *Physical Review Letters* **1993**, *70* (15), 2313–2316.

(65) Tian, C. S.; Shen, Y. R. Sum-Frequency Vibrational Spectroscopic Studies of Water/Vapor Interfaces. *Chemical physics letters* **2009**, *470* (1-3), 1–6.

(66) Sovago, M.; Campen, R.; Wurpel, G.; Muller, M.; Bakker, H.; Bonn, M. Vibrational Response of Hydrogen-Bonded Interfacial Water Is Dominated by Intramolecular Coupling. *Physical Review Letters* **2008**, *100* (17), 173901.

(67) Ni, Y.; Skinner, J. L. IR and SFG Vibrational Spectroscopy of the Water Bend in the Bulk Liquid and at the Liquid-Vapor Interface, Respectively. *The Journal of Chemical Physics* **2015**, *143* (1), 014502.

(68) Tian, C. S.; Shen, Y. R. Isotopic Dilution Study of the Water/Vapor Interface by Phase-Sensitive Sum-Frequency Vibrational Spectroscopy. *Journal of the American Chemical Society* **2009**, *131* (8), 2790–2791.

(69) Singh, P. C.; Nihonyanagi, S.; Yamaguchi, S.; Tahara, T. Communication: Ultrafast Vibrational Dynamics of Hydrogen Bond Network Terminated at the Air/Water Interface: a Two-Dimensional Heterodyne-Detected Vibrational Sum Frequency Generation Study. *Journal of Chemical Physics* **2013**, *139* (16), 161101.

(70) Inoue, K.-I.; Nihonyanagi, S.; Singh, P. C.; Yamaguchi, S.; Tahara, T. 2D Heterodyne-Detected Sum Frequency Generation Study on the Ultrafast Vibrational Dynamics of H2O and HOD Water at Charged Interfaces. *The Journal of Chemical Physics* **2015**, *142* (21), 212431.

(71) Inoue, K.-I.; Ishiyama, T.; Nihonyanagi, S.; Yamaguchi, S.; Morita, A.; Tahara, T. Efficient Spectral Diffusion at the Air/Water Interface Revealed by Femtosecond Time-Resolved Heterodyne-Detected Vibrational Sum Frequency Generation Spectroscopy. *The Journal of Physical Chemistry Letters* **2016**, *7* (10), 1811–1815.

(72) Ong, S.; Zhao, X.; Eisenthal, K. B. Polarization of Water Molecules at a Charged Interface: Second Harmonic Studies of the Silica/Water Interface. *Chemical physics letters* **1992**, *191* (3-4), 327–335.

(73) Nihonyanagi, S.; Kusaka, R.; Inoue, K.-I.; Adhikari, A.; Yamaguchi, S.; Tahara, T. Accurate Determination of Complex X(2) Spectrum of the Air/Water Interface. *The Journal of Chemical Physics* **2015**, *143* (12), 124707.

(74) Ostroverkhov, V.; Waychunas, G. A.; Shen, Y. R. Vibrational Spectra of Water at Water/A-Quartz (0001) Interface. *Chemical physics letters* **2004**, *386* (1-3), 144–148.

(75) Yeganeh, M.; Dougal, S.; Pink, H. Vibrational Spectroscopy of Water at Liquid/Solid Interfaces: Crossing the Isoelectric Point of a Solid Surface. *Physical Review Letters* **1999**, *83* (6), 1179–1182.

(76) Zhang, L.; Tian, C.; Waychunas, G. A.; Shen, Y. R. Structures and Charging of A-Alumina (0001)/Water Interfaces Studied by Sum-Frequency Vibrational Spectroscopy. *J. Am. Chem. Soc* **2008**, *130* (24), 7686–7694.

(77) Sung, J.; Zhang, L.; Tian, C.; Shen, Y. R.; Waychunas, G. A. Effect of pH on the Water/A-Al2O3 (1$\bar{1}$02) Interface Structure Studied by Sum-Frequency Vibrational Spectroscopy. *J Phys Chem C* **2011**, *115* (28), 13887–13893.

(78) Kataoka, S.; Gurau, M. C.; Albertorio, F.; Holden, M. A.; Lim, S.-M.; Yang, R. D.; Cremer, P. S. Investigation of Water Structure at the TiO2/Aqueous Interface. *Langmuir* **2004**, *20* (5), 1662–1666.

(79) Becraft, K. A.; Richmond, G. L. In Situ Vibrational Spectroscopic Studies of the CaF 2/H 2O Interface. *Langmuir* **2001**, *17* (25), 7721–7724.

(80) Gopalakrishnan, S.; Jungwirth, P.; Tobias, D. J.; Allen, H. C. Air-Liquid Interfaces of Aqueous Solutions Containing Ammonium and Sulfate: Spectroscopic and Molecular Dynamics Studies. *J Phys Chem B* **2005**, *109* (18), 8861–8872.

(81) Jena, K. C.; Covert, P. A.; Hore, D. K. The Effect of Salt on the Water Structure at a Charged Solid Surface: Differentiating Second- and Third-Order Nonlinear Contributions. *The Journal of Physical Chemistry Letters* **2011**, *2* (9), 1056–1061.

(82) Nihonyanagi, S.; Yamaguchi, S.; Tahara, T. Direct Evidence for Orientational Flip-Flop of Water Molecules at Charged Interfaces: a Heterodyne-Detected Vibrational Sum Frequency Generation Study. *The Journal of Chemical Physics* **2009**, *130* (20), 204704.

(83) Ostroverkhov, V.; Waychunas, G. A.; Shen, Y. R. New Information on Water Interfacial Structure Revealed by Phase-Sensitive Surface Spectroscopy. *Physical Review Letters* **2005**, *94* (4), 046102.

(84) Chen, X.; Hua, W.; Huang, Z.; Allen, H. C. Interfacial Water Structure Associated with Phospholipid Membranes Studied by Phase-Sensitive Vibrational Sum Frequency Generation Spectroscopy. *J. Am. Chem. Soc* **2010**, *132* (32), 11336–11342.

(85) Mondal, J. A.; Nihonyanagi, S.; Yamaguchi, S.; Tahara, T. Three Distinct Water Structures at a Zwitterionic Lipid/Water Interface Revealed by Heterodyne-Detected Vibrational Sum Frequency Generation. *J. Am. Chem. Soc* **2012**, *134* (18), 7842–7850.

(86) Ohto, T.; Backus, E. H. G.; Hsieh, C.-S.; Sulpizi, M.; Bonn, M.; Nagata, Y. Lipid Carbonyl Groups Terminate the Hydrogen Bond Network of Membrane-Bound Water. *The Journal of Physical Chemistry Letters* **2015**, *6* (22), 4499–4503.

(87) Dewan, S.; Yeganeh, M. S.; Borguet, E. Experimental Correlation Between Interfacial Water Structure and Mineral Reactivity. *The Journal of Physical Chemistry Letters* **2013**, *4* (11), 1977–1982.

(88) Chen, X.; Flores, S. C.; Lim, S.-M.; Zhang, Y.; Yang, T.; Kherb, J.; Cremer, P. S. Specific Anion Effects on Water Structure Adjacent to Protein Monolayers. *Langmuir* **2010**, *26* (21), 16447–16454.

(89) Nihonyanagi, S.; Yamaguchi, S.; Tahara, T. Counterion Effect on Interfacial Water at Charged Interfaces and Its Relevance to the Hofmeister Series. *Journal of the American Chemical Society* **2014**, *136* (17), 6155–6158.

(90) Jungwirth, P.; Tobias, D. J. Specific Ion Effects at the Air/Water Interface. *Chem. Rev.* **2006**, *106* (4), 1259–1281.

(91) Hua, W.; Jubb, A. M.; Allen, H. C. Electric Field Reversal of Na 2SO 4, (NH 4) 2SO 4, and Na 2CO 3Relative to CaCl 2and NaCl at the Air/Aqueous Interface Revealed by Heterodyne

Detected Phase-Sensitive Sum Frequency. *The Journal of Physical Chemistry Letters* **2011**, *2* (20), 2515–2520.

(92) Long, J. A.; Rankin, B. M.; Ben-Amotz, D. Micelle Structure and Hydrophobic Hydration. *J. Am. Chem. Soc* **2015**, *137* (33), 10809–10815.

(93) Costard, R.; Levinger, N. E.; Nibbering, E. T. J.; Elsaesser, T. Ultrafast Vibrational Dynamics of Water Confined in Phospholipid Reverse Micelles. *J Phys Chem B* **2012**, *116* (19), 5752–5759.

(94) Guyot-Sionnest, P.; Superfine, R.; HUNT, J. H.; Shen, Y. R. Vibrational Spectroscopy of a Silane Monolayer at Air/Solid and Liquid/Solid Interfaces Using Sum-Frequency Generation. *Chemical physics letters* **1988**, *144* (1), 1–5.

(95) Rivera, C. A.; Fourkas, J. T. Reexamining the Interpretation of Vibrational Sum-Frequency Generation Spectra. *Int Rev Phys Chem* **2011**, *30* (4), 409–443.

(96) Moad, A. J.; Simpson, G. J. A Unified Treatment of Selection Rules and Symmetry Relations for Sum-Frequency and Second Harmonic Spectroscopies. *J Phys Chem B* **2004**, *108* (11), 3548–3562.

(97) Wang, H.-F.; Velarde, L.; Gan, W.; Fu, L. Quantitative Sum-Frequency Generation Vibrational Spectroscopy of Molecular Surfaces and Interfaces: Lineshape, Polarization, and Orientation. *Annual Review of Physical Chemistry* **2015**, *66* (1), 189–216.

(98) Wei, X.; Hong, S.-C.; Lvovsky, A. I.; Held, H.; Shen, Y. R. Evaluation of Surface vs Bulk Contributions in Sum-Frequency Vibrational Spectroscopy Using Reflection and Transmission Geometries †. *J Phys Chem B* **2000**, *104* (14), 3349–3354.

(99) Held, H.; Lvovsky, A. I.; Wei, X.; Shen, Y. R. Bulk Contribution From Isotropic Media in Surface Sum-Frequency Generation. *Physical Review B* **2002**, *66* (20), 205110.

(100) Tian, C. S.; Shen, Y. R. Recent Progress on Sum-Frequency Spectroscopy. *Surface Science Reports* **2014**, *69* (2-3), 105–131.

(101) Vanselous, H.; Petersen, P. B. Extending the Capabilities of Heterodyne-Detected Sum-Frequency Generation Spectroscopy: Probing Any Interface in Any Polarization Combination. *The Journal of Physical Chemistry C* **2016**.

(102) Shen, Y. R. *The Principles of Nonlinear Optics*; Wiley: New York, 1984.

(103) Boyd, R. W. The Nonlinear Optical Susceptibility. In *Nonlinear Optics*; Elsevier, 2003; pp 1–65.

(104) Zheng, R.-H.; Wei, W.-M.; Shi, Q. Theoretical Investigation of Quadrupole Contributions to Surface Sum-Frequency Vibrational Spectroscopy. *Phys. Chem. Chem. Phys.* **2015**, *17* (14), 9068–9073.

(105) Kawaguchi, T.; Shiratori, K.; Henmi, Y.; Ishiyama, T.; Morita, A. Mechanisms of Sum Frequency Generation From Liquid Benzene: Symmetry Breaking at Interface and Bulk Contribution. *The Journal of Physical Chemistry C* **2012**, *116* (24), 13169–13182.

(106) Morita, A.; Hynes, J. T. A Theoretical Analysis of the Sum Frequency Generation Spectrum of the Water Surface. *Chemical Physics* **2000**, *258* (2-3), 371–390.

(107) Auer, B. M.; Skinner, J. L. Vibrational Sum-Frequency Spectroscopy of the Water Liquid/Vapor Interface. *J Phys Chem B* **2009**, *113* (13), 4125–4130.

(108) Morita, A. Improved Computation of Sum Frequency Generation Spectrum of the Surface of Water. *J Phys Chem B* **2006**, *110* (7), 3158–3163.

(109) Walker, D. S.; Hore, D. K.; Richmond, G. L. Understanding the Population, Coordination, and Orientation of Water Species Contributing to the Nonlinear Optical Spectroscopy of the Vapor-Water Interface Through Molecular Dynamics Simulations. *J Phys Chem B* **2006**, *110* (41), 20451–20459.

(110) Medders, G. R.; Paesani, F. Dissecting the Molecular Structure of the Air/Water Interface From Quantum Simulations of the Sum-Frequency Generation Spectrum. *Journal of the American Chemical Society* **2016**, *138* (11), 3912–3919.

(111) Morita, A.; Ishiyama, T. Recent Progress in Theoretical Analysis of Vibrational Sum Frequency Generation Spectroscopy. *Physical Chemistry Chemical Physics* **2008**, *10* (38), 5801–5816.

(112) Hayes, P. L.; Malin, J. N.; Jordan, D. S.; Geiger, F. M. Get Charged Up: Nonlinear Optical Voltammetry for Quantifying the Thermodynamics and Electrostatics of Metal Cations at Aqueous/Oxide Interfaces. *Chemical physics letters* **2010**, *499* (4–6), 183–192.

(113) Covert, P. A.; Jena, K. C.; Hore, D. K. Throwing Salt Into the Mix: Altering Interfacial Water Structure by Electrolyte Addition. *The Journal of Physical Chemistry Letters* **2014**, *5* (1), 143–148.

(114) Adamson, A. W.; Gast, A. P. *Physical Chemistry of Surfaces*; Wiley: New York, 1997; Vol. 6th ed.

(115) Yan, E. C. Y.; Liu, Y.; Eisenthal, K. B. New Method for Determination of Surface Potential of Microscopic Particles by Second Harmonic Generation. *J Phys Chem B* **1998**, *102* (33), 6331–6336.

(116) Ong, T. H.; Davies, P. B.; Bain, C. D. Sum-Frequency Spectroscopy of Monolayers of Alkoxy-Terminated Alkanethiols in Contact with Liquids. *Langmuir* **1993**, *9* (7), 1836–1845.

(117) Flores, S. C.; Kherb, J.; Cremer, P. S. Direct and Reverse Hofmeister Effects on Interfacial Water Structure. *The Journal of Physical Chemistry C* **2012**, *116* (27), 14408–14413.

(118) Gomez, S. A. S.; Jordan, D. S.; Troiano, J. M.; Geiger, F. M. Uranyl Adsorption at the Muscovite (Mica)/Water Interface Studied by Second Harmonic Generation. *Environ. Sci. Technol.* **2012**, *46* (20), 11154–11161.

(119) Chen, X.; Yang, T.; Kataoka, S.; Cremer, P. S. Specific Ion Effects on Interfacial Water Structure Near Macromolecules. *Journal of the American Chemical Society* **2007**, *129* (40), 12272–12279.

(120) Shen, Y. R. Surface Contribution Versus Bulk Contribution in Surface Nonlinear Optical Spectroscopy. *Appl Phys B* **1999**, *68* (3), 295–300.

(121) Byrnes, S. J.; Geissler, P. L.; Shen, Y. R. Ambiguities in Surface Nonlinear Spectroscopy Calculations. *Chemical physics letters* **2011**, *516* (4–6), 115–124.

(122) Superfine, R.; Huang, J. Y.; Shen, Y. R. Nonlinear Optical Studies of the Pure Liquid/Vapor Interface: Vibrational Spectra and Polar Ordering. *Physical Review Letters* **1991**, *66* (8), 1066.

(123) Feng, R.-R.; Guo, Y.; Lü, R.; Velarde, L.; Wang, H.-F. Consistency in the Sum Frequency Generation Intensity and Phase Vibrational Spectra of the Air/Neat Water Interface. *J. Phys. Chem. A* **2011**, *115* (23), 6015–6027.

(124) Parikh, A. N.; Allara, D. L. Self-Assembled Monolayers. In *Handbook of Biofunctional Surfaces*; A Versatile Tool for Biofunctionalization of Surfaces; Pan Stanford Publishing, 2013; pp 3–29–29.

(125) Gooding, J. J.; Ciampi, S. The Molecular Level Modification of Surfaces: From Self-Assembled Monolayers to Complex Molecular Assemblies. *Chem. Soc. Rev.* **2011**, *40* (5), 2704–2718.

(126) Love, J. C.; Estroff, L. A.; Kriebel, J. K.; Nuzzo, R. G.; Whitesides, G. M. Self-Assembled Monolayers of Thiolates on Metals as a Form of Nanotechnology. *Chem. Rev.* **2005**, *105* (4), 1103–1169.

(127) Murugan, P.; Krishnamurthy, M.; Jaisankar, S. N.; Samanta, D.; Mandal, A. B. Controlled Decoration of the Surface with Macromolecules: Polymerization on a Self-Assembled Monolayer (SAM). *Chemical Society Reviews* **2015**, *44* (10), 3212–3243.

(128) Jalal, I. M.; Zografi, G.; Rakshit, A. K.; Gunstone, F. D. Monolayer Properties of Fatty Acids. I. Thermodynamics of Spreading. *Journal of Colloid and Interface Science* **1980**, *76* (1), 146–156.

(129) Kaganer, V. M.; Osipov, M. A.; Peterson, I. R. A Molecular Model for Tilting Phase Transitions Between Condensed Phases of Langmuir Monolayers. *The Journal of Chemical Physics* **1993**, *98* (4), 3512.

(130) Brzoska, J. B.; Azouz, I. B.; Rondelez, F. Silanization of Solid Substrates: a Step Toward Reproducibility. *Langmuir* **1994**, *10* (11), 4367–4373.

(131) Carraro, C.; Yauw, O. W.; Sung, M. M.; Maboudian, R. Observation of Three Growth Mechanisms in Self-Assembled Monolayers. *J Phys Chem B* **1998**, *102* (23), 4441–4445.

(132) Vericat, C.; Vela, M. E.; Salvarezza, R. C. Self-Assembled Monolayers of Alkanethiols on Au(111): Surface Structures, Defects and Dynamics. *Physical Chemistry Chemical Physics* **2005**, *7* (18), 3258–3268.

(133) Pflaum, J.; Bracco, G.; Schreiber, F.; Colorado, R., Jr.; Shmakova, O. E.; Lee, T. R.; Scoles, G.; Kahn, A. Structure and Electronic Properties of CH3- and CF3-Terminated Alkanethiol Monolayers on Au(): a Scanning Tunneling Microscopy, Surface X-Ray and Helium Scattering Study. *Surface Science* **2002**, *498* (1-2), 89–104.

(134) Evenson, S. A.; Badyal, J. P. S.; Pearson, C.; Petty, M. C. Variation in Intermolecular Spacing with Dipping Pressure for Arachidic Acid LB Films. *J. Phys. Chem* **1996**, *100* (28), 11672–11674.

(135) Poirier, G. E.; Tarlov, M. J. The C(4X2) Superlattice of N-Alkanethiol Monolayers Self-Assembled on Au(111). *Langmuir* **1994**, *10* (9), 2853–2856.

(136) Allara, D. L.; Parikh, A. N.; Rondelez, F. Evidence for a Unique Chain Organization in Long Chain Silane Monolayers Deposited on Two Widely Different Solid Substrates. *Langmuir* **1995**, *11* (7), 2357–2360.

(137) Dynarowicz-Łątka, P.; Dhanabalan, A.; Oliveira, O. N., Jr. Modern Physicochemical Research on Langmuir Monolayers. *Advances in Colloid and Interface Science* **2001**, *91* (2), 221–293.

(138) Onclin, S.; Ravoo, B. J.; Reinhoudt, D. N. Engineering Silicon Oxide Surfaces Using Self-Assembled Monolayers. *Angew. Chem. Int. Ed. Engl.* **2005**, *44* (39), 6282–6304.

(139) Haensch, C.; Ott, C.; Hoeppener, S.; Schubert, U. S. Combination of Different Chemical Surface Reactions for the Fabrication of Chemically Versatile Building Blocks Onto Silicon Surfaces. *Langmuir* **2008**, *24* (18), 10222–10227.

(140) Wasserman, S. R.; Tao, Y. T.; Whitesides, G. M. Structure and Reactivity of Alkylsiloxane Monolayers Formed by Reaction of Alkyltrichlorosilanes on Silicon Substrates. *Langmuir* **1989**, *5* (4), 1074–1087.

(141) Haensch, C.; Hoeppener, S.; Schubert, U. S. Chemical Surface Reactions by Click Chemistry: Coumarin Dye Modification of 11-Bromoundecyltrichlorosilane Monolayers. *Nanotechnology* **2007**, *19* (3), 035703.

(142) Drexler, K.; Smirnova, J.; Galetskaya, M.; Voss, S.; Fonin, M.; Boneberg, J.; Rüdiger, U.; Leiderer, P.; Steiner, U. E. X-Ray Photoelectron Spectroscopy- and Surface Plasmon Resonance-Detected Photo Release of Photolabile Protecting Groups From Nucleoside Self-Assembled Monolayers on Gold Surfaces. *Langmuir* **2009**, *25* (18), 10794–10801.

(143) Haensch, C.; Hoeppener, S.; Schubert, U. S. Chemical Modification of Self-Assembled Silane Based Monolayers by Surface Reactions. *Chemical Society Reviews* **2010**, *39* (6), 2323.

(144) Kurth, D. G.; Bein, T. Surface Reactions on Thin Layers of Silane Coupling Agents. *Langmuir* **1993**, *9* (11), 2965–2973.

(145) Vaidya, B.; Chen, J.; Porter, M. D.; Angelici, R. J. Effects of Packing and Orientation on the Hydrolysis of Ester Monolayers on Gold. *Langmuir* **2001**, *17* (21), 6569–6576.

(146) Barbara Dordi; Holger Schönherr, A.; Vancso, G. J. Reactivity in the Confinement of Self-Assembled Monolayers: Chain Length Effects on the Hydrolysis of N-Hydroxysuccinimide Ester Disulfides on Gold. *Langmuir* **2003**, *19* (14), 5780–5786.

(147) Holger Schönherr; Chuanliang Feng, A.; Shovsky, A. *Interfacial Reactions in Confinement: Kinetics and Temperature Dependence of Reactions in Self-Assembled Monolayers Compared to Ultrathin Polymer Films*; American Chemical Society, 2003; Vol. 19, pp 10843–10851.

2. Design projects

2.1. Laser table enclosure

The laser table serves as a vibrationally-dampened platform for the laser, optics, and detectors. An enclosure serves several purposes. It isolates the setup from air currents, which reduces noise and improves the laser's phase stability. It is a safety measure, blocking unexpected/uncontrolled reflections. It also allows the path of the IR beam to be purged of water vapor and CO_2. SFG spectra of weakly hydrogen-bonded OH stretching modes and OD and carbonyl stretches are all obscured in room air due to atmospheric absorption.

Since the walls must be taken down often for alignment, setup of experiments, and insertion of samples, they are assembled from removable panels fastened to stationary posts by magnet. Brackets secure the posts to the breadboard plate (Figure 2.1). Posts are constructed from rectangular steel tubing (Online Metals, A513 hot-rolled mild steel, 0.5" × 1", thickness 0.065") cut in to 12" lengths. Brackets attach with 10-32 screws to the posts and 1/4-20 screws to the breadboard plate. They are machined from aluminum angle stock (Online Metals, 6061-T6 extruded structural angle, 2" ×2" ×0.25") with large tolerances. The wide, 1.5" slots for attachment to the table allow each bracket (and therefore, each post) to be secured at any point on the table. Panels were finished from 12"×24" aluminum sheets (Online Metals, 6061-T6, 0.040" thick) and painted with latex primer and matte paint to prevent light reflection. The magnets (K&J Magnetics D61-N52 3/8" dia × 1/16" N52, 2.62 lb pull force, and B842-N52 1/2" × 1/4" × 1/8", N52, 5.54 lb pull force) on the panels were applied by epoxy to the outer (red) side of the panels to minimize strain on the adhesive and form a tight seal against the posts. Posts

and brackets are interchangeable and can be used at straight sections or inside or outside corners. Panels often need to be modified, and are easily cut, bent, and perforated for the passage of wires, tubing, and light. The enclosure is covered using corrugated polypropylene sheeting (48” 24”, 4 mm thick, super clear), which is light, rigid, and easily modified. It can be cut to size by razor, and hinged by cutting only one ply of the sheet.

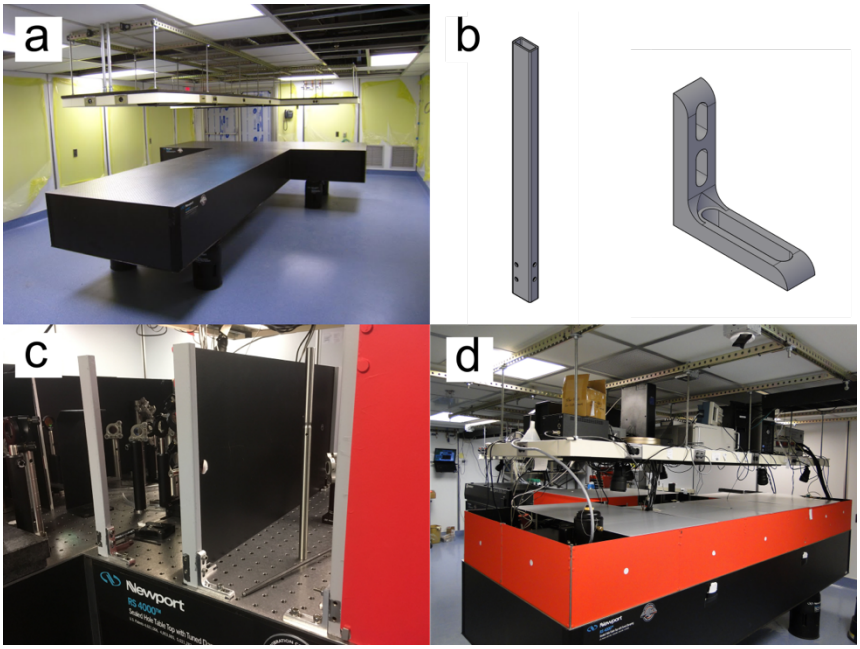

Figure 2.1 Laser table and enclosure: (a) bare optical table with pneumatic isolating legs, (b) post and bracket design for enclosure (not to scale), (c) posts and panels, and (d) assembled enclosure with lid.

The areas requiring purging were divided into three sealed compartments which can be individually perfused. These cover (1) the IR beam as it leaves the OPA and a telescope (to adjust beam diameter) and periscope (to raise beam height), (2) The continuum IR setup, and (3) the interferometer and SFG/2DIR setup. Scrubbed air with CO_2 and H_2O removed is produced in the lab with a CO_2 absorber (Purgas) and enters the laser enclosure through flexible tubing. This scrubbed air is separated into three streams, one for each compartment. Each branch is fitted with a quick disconnect valve at the manifold, allowing air to be routed only to the compartments

needing purging. Each compartment is evenly flushed with scrubbed air a system of branching tubes of decreasing diameter. H_2O vapor and CO_2 are largely removed after 15 minutes of purging (Figure 2.2).

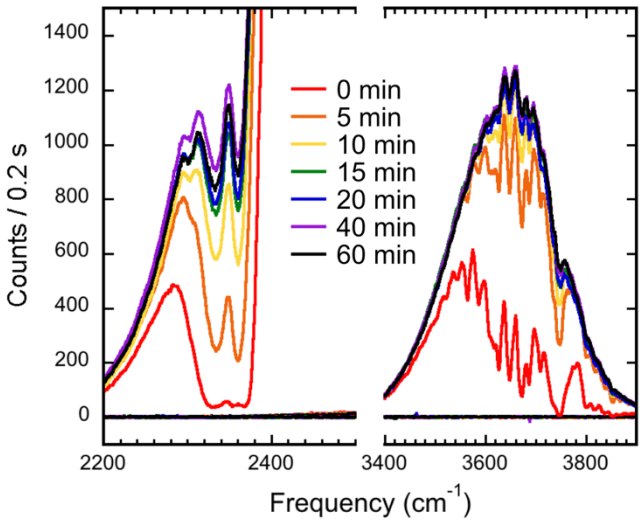

Figure 2.2 Reduction of IR adsorption with time due to CO_2 (2350 cm^{-1}) and water vapor (3700 cm^{-1}).

2.2. Contact angle goniometer

Contact angle goniometry is a sensitive technique for characterizing surfaces which relates the contact angle θ of a liquid droplet at a solid to the free energy of the solid surface (Figure 2.3). The work of adhesion between the liquid and solid w_{SL} is the difference between the surface tension at the solid/vapor interface (γ_{SL}) and the surface tension at the solid/liquid and liquid/vapor interfaces (γ_{SL} and γ_{LV}), along with a term dependent on the contact angle. That angle is dependent on the adhesivity between molecules in the liquid versus liquid molecules and the solid.[1–3]

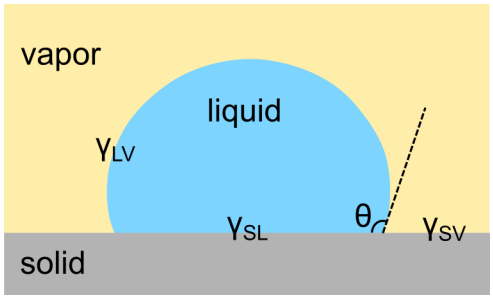

Figure 2.3 Liquid droplet at solid interface

$$w_{SL} = \gamma_{SV} - (\gamma_{SL} + \gamma_{LV}\cos(\theta)) = 0. \quad \textbf{(2.1)}$$

Water contact angle is sensitive to surface polarity and roughness, allowing partial monolayers to be detected or small differences in monolayer ordering to be discerned. In Figure 2.4, for instance, we see the contact angle of water at C18 (octadecylsiloxane) monolayers adsorbed from toluene solutions with different moisture contents. Water contact angle is plotted versus the frequency of the asymmetric methylene stretch of the monolayer, which is sensitive to monolayer packing.[4] The most highly packed and ordered monolayers, those with the lowest frequency, also have the highest contact angle.

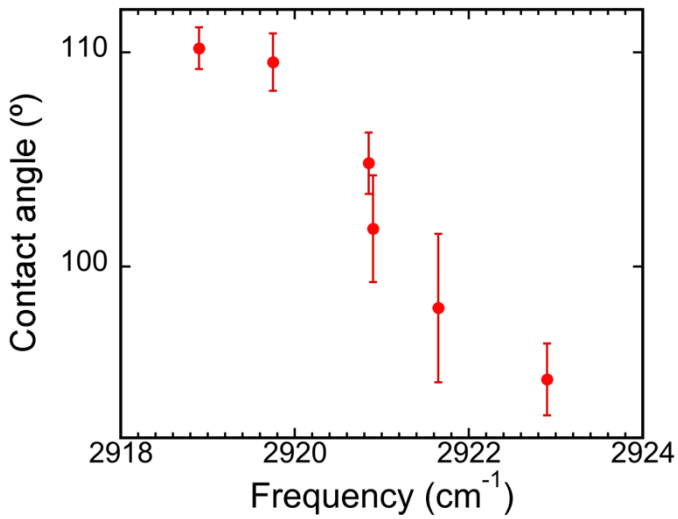

Figure 2.4 Contact angle and frequency of the asymmetric methylene stretch as measured by IR spectroscopy for C18 monolayers adsorbed from toluene solutions with different moisture contents.

The contact angle goniometer (Figure 2.5 a) consists of a collimated white light source (tungsten-halogen lamp, ThorLabs QTH10), a level platform for the substrate, a syringe (25 μL, Hamilton) and syringe mount for dispensing water, a microscope objective for focusing the image on the camera (5x, Zeiss), and several filters (neutral density filter, ND20 and blue dichroic filter FD1B both Thorlabs) between the lens and camera (1280x1024 monochrome CMOS camera, ThorLabs DCC1545M). The syringe mount is easily removed and replaced for refilling of the syringe. The position of the water droplet can be finely adjusted in x, y, and z to place it in the focus. The neutral density filter reduces the intensity of the light onto the sensor, and a blue filter increases the image resolution on the monochrome CMOS sensor by reducing the effect of chromatic aberration due mainly to the large condenser lens after the light source.

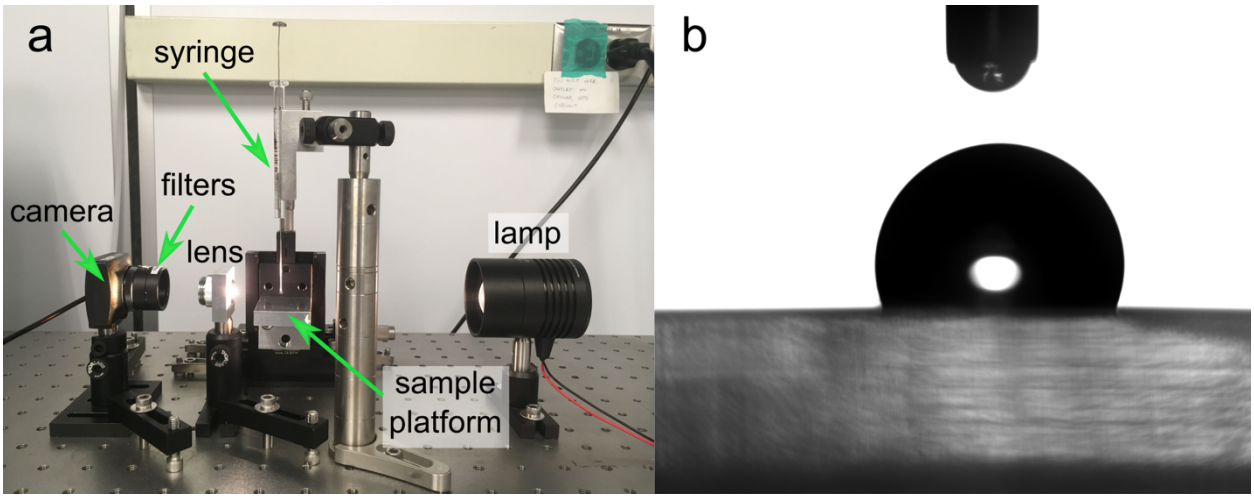

Figure 2.5 Measuring contact angles: (a) contact angle goniometer. (b) Image of water droplet on C18 monolayer

Images (Figure 2.5 b) are collected by UC480 Camera Manager in 8 bit monochrome and analyzed by the DropSnake plugin[5] in ImageJ. This plugin fits the droplet outline and calculates the contact angle with the substrate at the left and right sides. To determine the water contact angle at a sample, the syringe is flushed and filled with ultrapure water (18.2 MΩ · cm @25 ºC, 5 ppm TOC). The syringe assembly is replaced and aligned so that the tip of the needle is at the focus, and the sample is rinsed and dried and placed on the platform. A droplet of 3 μL is formed at the needle. The platform is raised towards the needle, and the hanging drop at the needle is slowly brought into contact with the sample. The platform is then lowered to release the drop from the needle, and an image is collected of the droplet on the sample surface. Images of at least three droplets are collected at each sample, and these contact angles are averaged to give the contact angle.

2.3. White cell

FTIR characterization allows the chemical structure and ordering of a monolayer to be determined. However, monolayers have a low IR absorbance (~0.003 OD) in transmission, which makes analysis of spectra difficult. One strategy to amplify IR signal is to pass through the sample multiple times. Multipass schemes include linear cavities (as in cavity ringdown spectroscopy),[6] off-axis cavities,[7–10] and parallel mirrors. Parallel mirror systems are extremely sensitive to alignment and only work with highly reflective samples, and linear cavities require end mirrors with expensive broadband IR reflective coatings. However, off-axis cavities generally use standard spherical mirrors and can easily accommodate transparent samples. I built a White cell,[7,8,11] an off-axis cavity which passes the IR beam through the sample eight times.

My setup consists of three gold spherical mirrors of the same focal length *f:* two 0.5" in diameter (Thorlabs CM127-050-M01) in one plane, and a larger 2.0" mirror (Thorlabs M508-050-M01) above in a parallel plane (Figure 2.6). One flat mirror routes light from the IR source into the cell, and another routes the light back out and to the detector. To ensure the mirrors were parallel and make optimization of the cavity length easier, the mirrors were set into plates compatible with a cage system. Each plate (Thorlabs LCP03 (lower) and LCP06 (upper)) can slide up and down four parallel 6 mm shafts. The 1" diameter windows with monolayers are placed in a depression just above the two small mirrors, where the IR beams are close together. Initial adjustment was difficult due to the multiple passes, but does not have to be repeated.

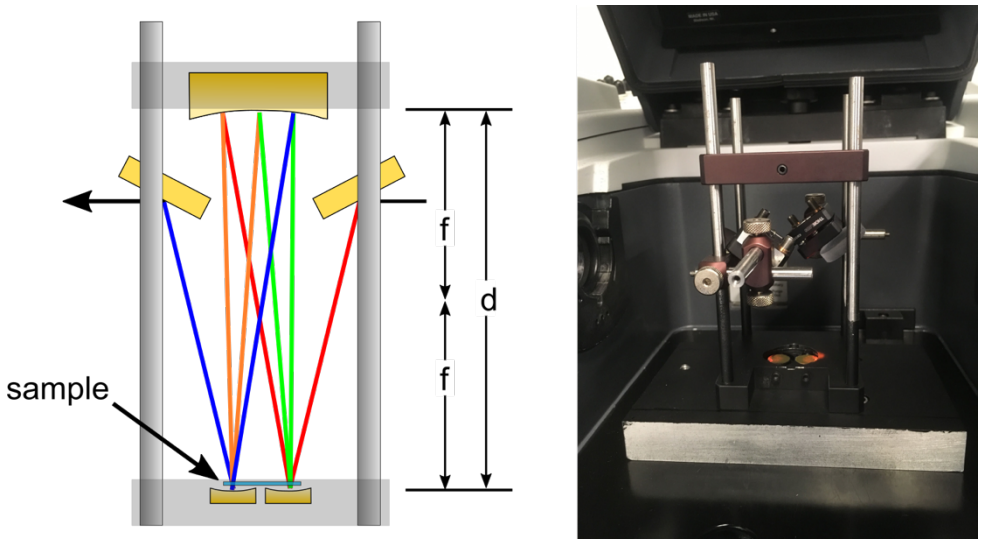

Figure 2.6 White cell. Left: diagram indicates focal length f of mirrors and distance between mirrors, d. The path of the IR beam is indicated by red, orange, green, and blue lines. Right: photograph of White cell.

The White cell increases the IR absorption of a monolayer on SiO_2-coated CaF_2 by eight times (Figure 2.7). Total IR throughput is reduced to 22% compared to simple transmission, mainly due to clipping by the routing mirrors. However, the IR source is bright enough and the detector is sensitive enough that this is not a limitation.

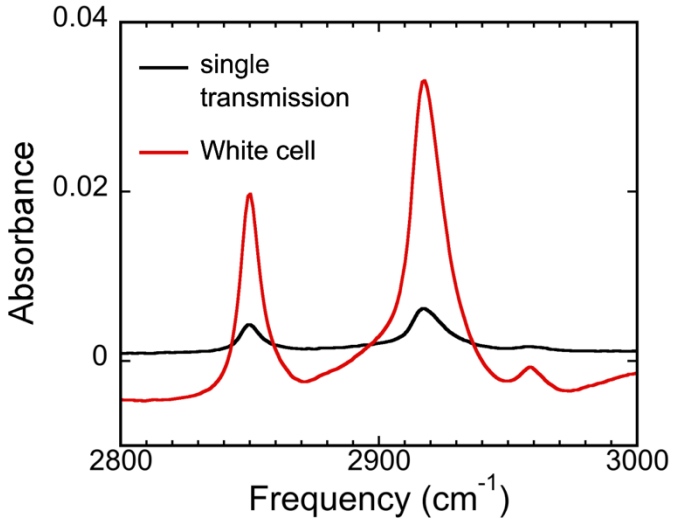

Figure 2.7 FTIR spectrum of a C18 monolayer taken in simple transmission (black) and with the White cell (red). Y-offsets are due to small differences in absorption between sample and bare substrate (background).

2.4. Liquid cell

A liquid cell was design for SFG study of buried interfaces at aqueous solutions. The cell must have an appropriate geometry: it must form a good seal with the sample and provide clearance for the beams to enter and exit. All the components of the cell must be chemically compatible with our cleaning procedure. We use an aggressive cleaning solution of Nochromix powder ($(NH_4)_2S_2O_8$, an oxidizer) dissolved in concentrated sulfuric acid, which is compatible with few materials aside from PTFE, glass, and ceramic. Thorough cleaning is essential because we are looking at surfaces, where contaminants tend to collect from the bulk.

A modular system was created which can accommodate circular 1" diameter windows, right angle prisms (10 mm tall, 10 mm each leg), and equilateral prisms (10 mm tall, 10 mm each side) in the same optical mount. For the windows, the cell is assembled like a sandwich with the sample window at the front, a Viton or PTFE-encapsulated o-ring in the middle, and a glass-filled PTFE plate at the back. Holes in the back plate are fitted with short sections of PTFE tubing (18 gauge, Cole Parmer), over which larger 14 gauge PTFE tubing is slipped. This tubing leads to a syringe (1 mL gaslight glass syringe, Hamilton Company 81301, or 1 mL disposable polypropylene/polyethylene Norm-ject) via a slip Luer hub adaptor (Hamilton Company 90614), (Figure 2.8). The window, o-ring, and back plate are squeezed together in a 1" optical rotation mount. The setup is similar for the prisms, except that prisms are wedged into a glass-filled PTFE or Delrin front plate and sealed with a smaller o-ring (Figure 2.9). When assembled, solutions can be added or exchanged without disturbing the sample position.

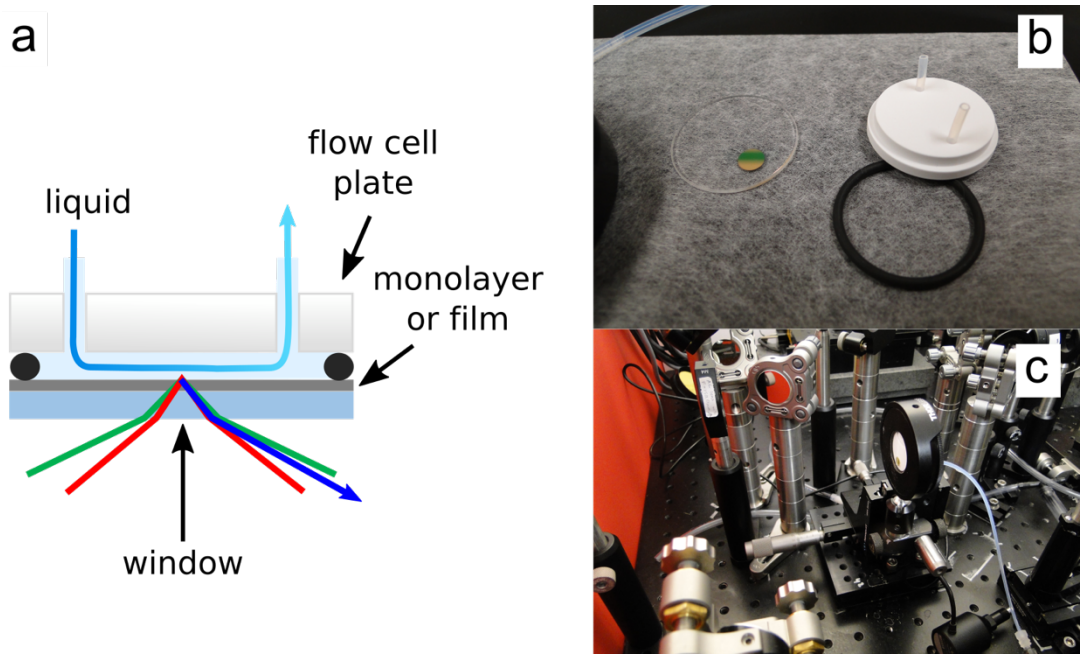

Figure 2.8 Liquid cell (a) schematic and (b) assembly

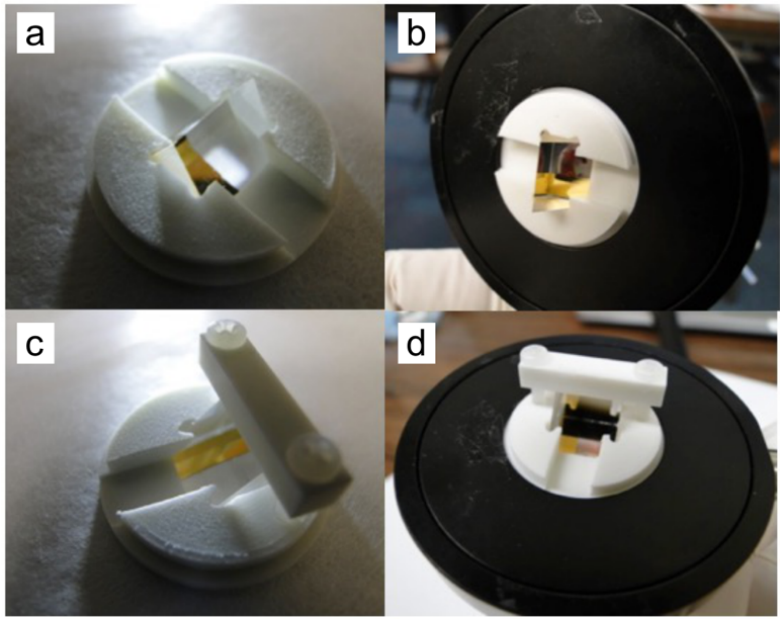

Figure 2.9 Prism mounting for (a) and (b) equilateral prisms, and (c) and (d) right angle prisms.

2.5. Substrates

2.5.1. Substrate materials

Substrate materials must be compatible with the chemistry of the monolayer or film and be transparent at the IR, visible, and SFG wavelengths. In order to probe the water structure, the IR frequency is tuned to be resonant with the OH stretching mode. This means that passing through even a thin layer of water is not feasible; the IR beam will be entirely absorbed. Instead, the interface is approached by passing through the substrate and reflecting off the backside (Figure 2.10).

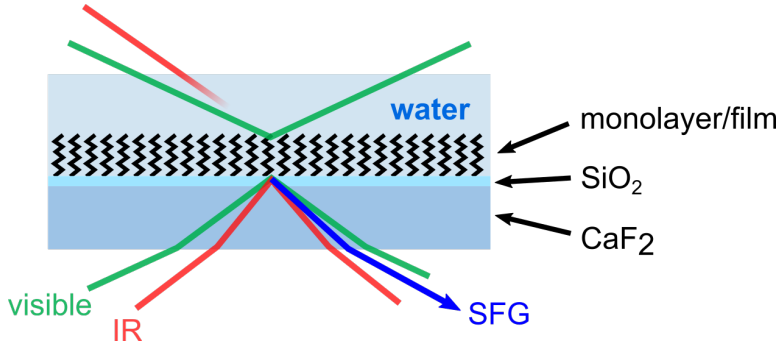

Figure 2.10 Accessing the water/sample interface: passing through the IR-transparent substrate and reflecting off the back side avoids absorption of the IR beam by water.

Trichlorosilane monolayers such as the twelve and eighteen carbon alkane monolayers C12 and C18 studied in the mixed monolayer project bind to silica. The chlorines are hydrolyzed by the thin layer of water adsorbed to the silica, and the silanol forms a siloxane (Si-O-Si) bond to the substrate.[12] These monolayers can be applied to UV fused silica, which is also transparent in the visible wavelengths and the CH stretch region in the IR (Figure 2.11), allowing examination of those modes by SFG. IR fused silica eliminates the absorption between 3400 and 3800 cm^{-1}, allowing OH stretch modes of water to be probed as well, but like UV fused silica, cannot be used below 2500 cm^{-1}. The OD stretch of D_2O is obscured, as are cyanate and thiocyanate CN

and carbonyl CO stretching modes. The solution is to deposit a thin layer of SiO_2 on CaF_2, which is transparent in the visible range and in the IR down to 1000 cm^{-1}. CaF_2 also has low group velocity dispersion, a property which is desirable particularly when the path length through the substrate is long (such as in a prism). Group velocity dispersion is a measure of the delay of short wavelengths relative to long wavelengths in an optical pulse as it passes through material.[13] It increases the temporal length of pulse and causes the center frequency to shift over its duration. This reduces the efficiency of sum frequency generation and causes difficulty in normalizing spectra to the IR power.

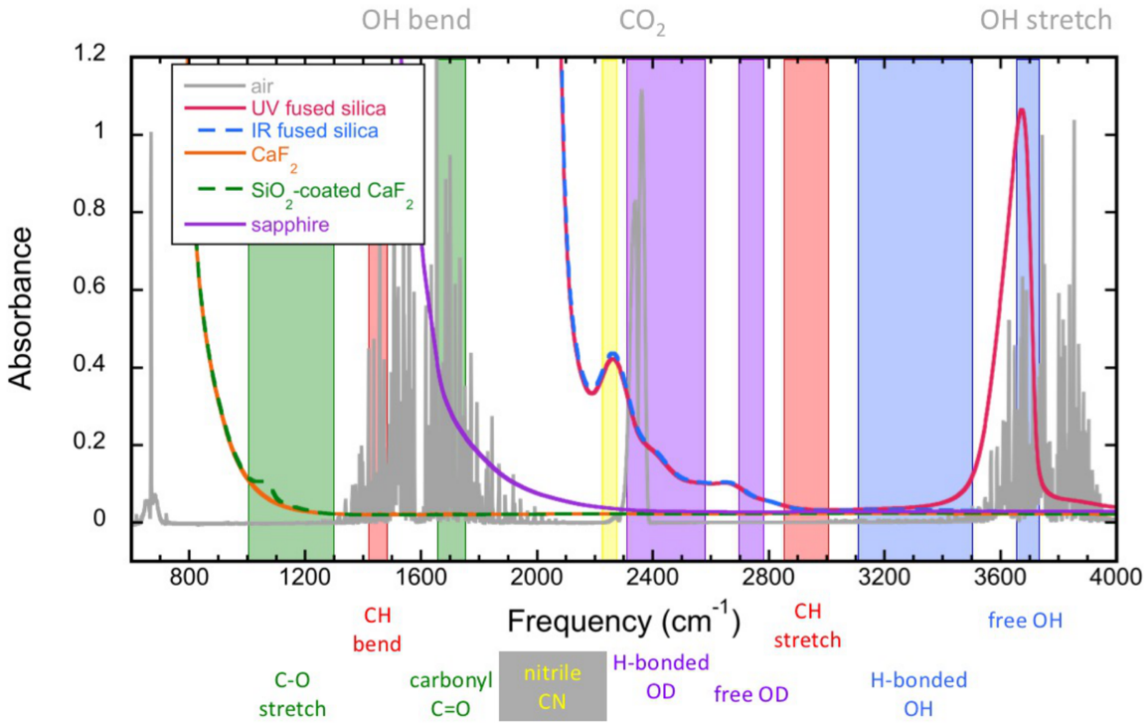

Figure 2.11 IR absorption frequencies of air (gray), substrates, and chromophores of interest (colored bands).

Table 2.1 Optical and chemical properties of materials used as SFG substrates: IR transmission range in mid IR, refractive index n_{IR} at 3000 cm^{-1}, n_{vis} at 793 nm, group velocity dispersion (GVD) at 3000 cm^{-1}, and compatible cleaning method.

Material	IR range (cm^{-1})	n_{IR}	n_{vis}	GVD* (fs^2/mm)	Cleaning
UV fused silica[14]	2500-3400	1.411	1.453	-845	piranha or Nochromix soln
IR fused silica[15]	2500-4000	1.450	1.451	-4.23	piranha or Nochromix soln
CaF_2 [16]	1000-4000	1.415	1.431	-153	KOH in EtOH
SiO_2-coated CaF_2	1000-4000	---	---	---	UV ozone, solvent rinse, or >500ºC
Sapphire[17]	2000-4000	1.701	1.760	-806	piranha or Nochromix soln

*GVD $= \frac{\lambda_0^3}{2\pi c_0^2}\left(\frac{\partial^2 n}{\partial \lambda^2}\right)_{\lambda=\lambda_0}$

2.5.2. SiO_2-coated CaF_2

Silica is applied to CaF_2 windows (diameter 25.4 mm, 1 mm thick, CeNing Optics or Crystran Ltd.) and prisms (equilateral, 10×10×10 mm, CeNing Optics) by atomic layer deposition (Oxford FlexAL system). Substrates are coated with a 120 nm layer of SiO_2 in 110 ºC plasma and then annealed in a vacuum furnace (~1 × 10^{-6} torr) at 800 ºC to prevent delamination of the silica layer. An air-free or dry environment is necessary to prevent frosting of the CaF_2, which becomes water soluble at high temperatures. ALD is a gas phase process and so substrates are coated equally on all sides. Coating can be limited to a single window surface by first applying a low outgassing film. For this purpose, FSC-M (Microposit) mask is spin-coated on one side and baked at 110 ºC for at least twelve hours to drive off all solvent. After SiO_2 coating, the

photoresist can be removed by soaking the substrate in photoresist removal solvent (Microposit Remover 1165).

A spot of gold is also applied by DC magnetron argon sputtering through a stainless steel mask (Figure 2.12). SFG of gold in the *ppp* polarization (all beams perpendicular, 'p,' to the sample) produces a nonresonant signal, which is used to normalize sample spectra to the frequency envelope of the broadband IR pulse. The strong signal from the gold also makes it easier to optimize the sample position at the overlap of the visible and IR beams. An adhesion layer of titanium (5 nm, DC power 118 W/365 V) is deposited before the gold (150 nm, 70 W/375 V) in 5 mTorr argon. With a skin depth of 16.2 nm for 792.5 nm light and 33.5 nm for 3400 nm light, the titanium adhesion layer does not influence the gold nonresonant SFG response.

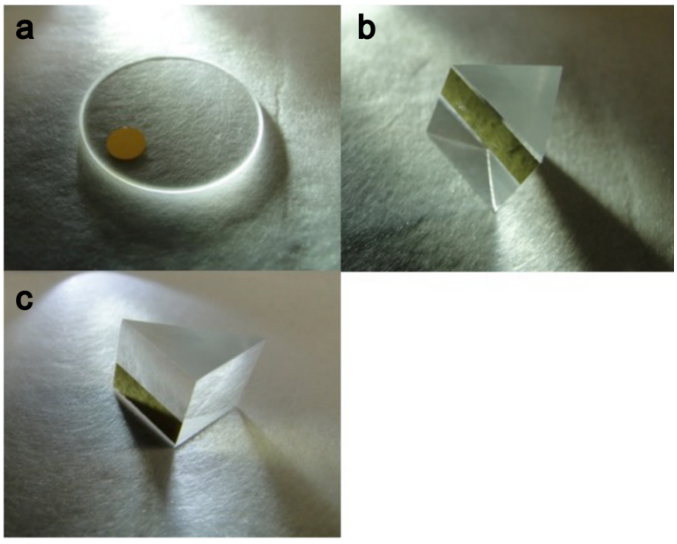

Figure 2.12 Substrates with gold applied: (a) window, (b) equilateral prism, and (c) right angle prism.

The layer of silica is thin enough to have little effect on IR transmission (Figure 2.11), while still allowing for trichlorosilane monolayer adsorption. Monolayers on the coated CaF_2 are indistinguishable from those grown on glass. The combination of CaF_2 and silica does complicate substrate cleaning, however, as piranha and Nochromix solutions etch the CaF_2, and

KOH (base bath) removes the silica. Clean substrates are essential for successful monolayer application. The best solution is to coat the CaF_2 just before they are needed, so that cleaning is not necessary. UV ozone cleaning, solvent rinsing, and heat treatment (800 ºC in vacuum furnace) are other options. Sonicating the substrates in polar solvents can remove the silica.

2.5.3. Substrate geometry

The shape of the substrate is another consideration, as it has a large effect on the intensity (I_{SFG}) and form of the SFG signal. Refraction of the laser beams through the substrate changes the angles of incidence (θ_{SFG}, θ_{vis}, and θ_{IR}) at the interface (Figure 2.13).

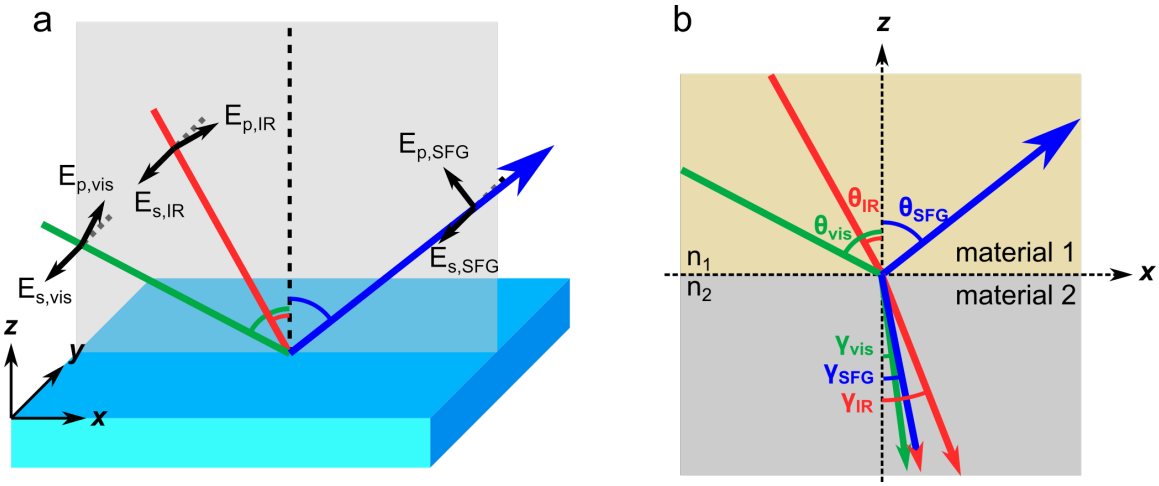

Figure 2.13 Geometry of SFG spectroscopy: (a) laboratory (polarization) frame and (b) sample (xyz) frame. E refers to the electric field produced by each beam, either in the s or p polarization (E_s or E_p).

SFG intensity at frequency ω_{SFG} is proportional to the absolute square of the effective nonlinear susceptibility, $\chi_{eff}^{(2)}$:[18–21]

$$I_{SFG}(\omega_{SFG}) = \frac{8\pi^3 \omega_{SFG}^2 \sec\ \theta_{SFG}}{c^3 n_1(\omega_{SFG}) n_1(\omega_{vis}) n_1(\omega_{IR})} |\chi_{eff}^{(2)}|^2 I_{vis}(\omega_{vis}) I_{IR}(\omega_{IR}) \quad \textbf{(2.2)}$$

where I_{vis} and I_{IR} are the intensities of the visible and IR beams, and $n_1(\omega_i)$ is the frequency-dependent refractive index. The effective nonlinear susceptibility depends both on the polarization ($\hat{\mathrm{e}}(\omega_i)$ is the unit polarization vector) and Fresnel factor ($L(\omega_i)$) of each beam in addition to the nonlinear susceptibility $\chi^{(2)}$. The SFG intensity dependence on beam angle comes mainly from these Fresnel factors.

$$\chi_{\text{eff}}^{(2)} = [\hat{\mathbf{e}}(\omega_{\text{SFG}}) \cdot \mathbf{L}(\omega_{\text{SFG}})] \cdot \chi^{(2)} : [\mathbf{L}(\omega_{\text{vis}})\hat{\mathbf{e}}(\omega_{\text{vis}})][\mathbf{L}(\omega_{\text{IR}})\hat{\mathbf{e}}(\omega_{\text{IR}})] \quad \textbf{(2.3)}$$

For a sample which is isotropic in the plane of the sample (in xy), there are only four non-zero and unique components of $\chi_{\text{eff}}^{(2)}$: $\chi_{\text{eff},ssp}^{(2)}$, $\chi_{\text{eff},sps}^{(2)}$, $\chi_{\text{eff},pss}^{(2)}$, and $\chi_{\text{eff},ppp}^{(2)}$.[22] The s and p indices refer to the polarization of the SFG, visible, and IR beams, in that order: s means the beam polarization is parallel to the sample plane, and p means that it is perpendicular to s and to the direction of beam propagation. The choice of beam polarization combination determines which vibrational modes are probed, since only chromophores in the proper orientation relative to the polarization and angle of the beams will appear in the spectra (Figure 2.14). Molecular orientation can be determined from spectra in multiple polarizations and by taking into account the symmetry of the chromophores.[19,20,23]

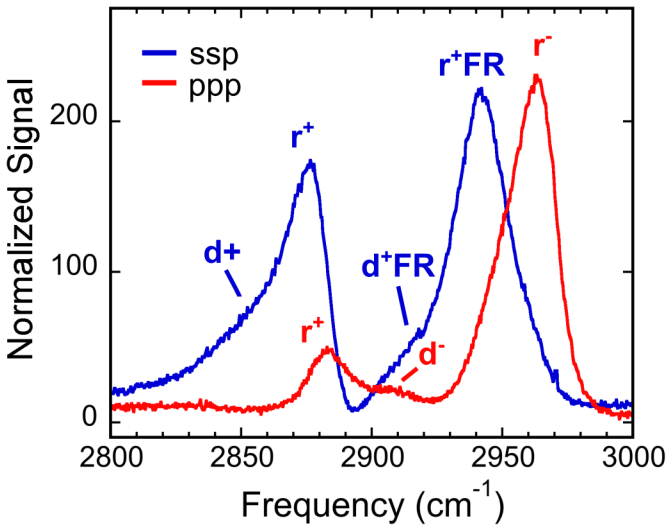

Figure 2.14 SFG spectrum of a C18 monolayer using *ssp* and *ppp* polarizations. Modes are indicated above peaks. Methylene modes are indicated with a 'd', methyl with an 'r', symmetric with a '+', asymmetric with a '-', and Fermi resonances with 'FR'

In order to calculate SFG response, the $\chi^{(2)}$ elements expressed in lab (beam polarization) coordinates are re-expressed in terms of the sample coordinates *xyz* (Figure 2.13). All but $\chi^{(2)}_{\text{eff},ppp}$ are a function of only one element, making them simple to calculate qualitatively without knowing any details about molecular symmetry or orientation. The relations for $\chi^{(2)}_{\text{eff},ssp}$ and $\chi^{(2)}_{\text{eff},ppp}$, the most commonly used polarizations, are given below.

$$\chi^{(2)}_{\text{eff},ssp} = L_{yy}(\omega_{\text{SFG}})L_{yy}(\omega_{\text{vis}})L_{zz}(\omega_{\text{IR}})\sin\ \theta_{IR}\chi^{(2)}_{yyz} \tag{2.4}$$

$$\begin{aligned}\chi^{(2)}_{\text{eff},ppp} = &-L_{xx}(\omega_{\text{SFG}})L_{xx}(\omega_{\text{vis}})L_{zz}(\omega_{\text{IR}}) \\ &- L_{xx}(\omega_{\text{SFG}})L_{zz}(\omega_{\text{vis}})L_{xx}(\omega_{\text{IR}})\cos\theta_{\text{SFG}}\sin\theta_{\text{vis}}\cos\theta_{\text{IR}}\chi^{(2)}_{xzx} \\ &+ L_{zz}(\omega_{\text{SFG}})L_{xx}(\omega_{\text{vis}})L_{xx}(\omega_{\text{IR}})\sin\theta_{\text{SFG}}\cos\theta_{\text{vis}}\cos\theta_{\text{IR}}\chi^{(2)}_{zxx} \\ &+ L_{zz}(\omega_{\text{SFG}})L_{zz}(\omega_{\text{vis}})L_{zz}(\omega_{\text{IR}})\sin\theta_{\text{SFG}}\sin\theta_{\text{vis}}\sin\theta_{\text{IR}}\chi^{(2)}_{zzz}\end{aligned} \tag{2.5}$$

In Equations 2.4 and 2.5, L_{ii} are the diagonal elements of $L(\omega_i)$, the nonlinear Fresnel tensor. The angles and beam angles are named according to the scheme in Figure 2.13 b.

$$L_{xx}(\omega_i) = \frac{2n_1(\omega_i)\cos\ \gamma_i}{n_1(\omega_i)\cos\ \gamma_i + n_2(\omega_i)\cos\ \theta_i} \quad \textbf{(2.6)}$$

$$L_{yy}(\omega_i) = \frac{2n_1(\omega_i)\cos\ \theta_i}{n_1(\omega_i)\cos\ \theta_i + n_2(\omega_i)\cos\ \gamma_i} \quad \textbf{(2.7)}$$

$$L_{zz}(\omega_i) = \frac{2n_1^2(\omega_i)n_2(\omega_i)\cos\ \theta_i}{n_1(\omega_i)\cos\ \gamma_i + n_2(\omega_i)\cos\ \theta_i}\left(\frac{n_1(\omega_i)}{n'(\omega_i)}\right)^2 \quad \textbf{(2.8)}$$

The refractive index $n'(\omega_i)$ is the refractive index of the interfacial region. It can be estimated as:[21]

$$n'(\omega_i) = \sqrt{\frac{n_2^2(\omega_i)(n_2^2(\omega_i)+5)}{4n_2^2(\omega_i)+2}} \quad \textbf{(2.9)}$$

I_{SFG} can be calculated in a qualitative way for any single– $\chi^{(2)}$ element, such as for $I_{ssp}(\omega_{\mathrm{SFG}})$, by leaving out all but $\chi_{\mathrm{eff}}^{(2)}$ from Equation 2.2 (Figure 2.15). Only the substrate geometry (e.g., flat window, prism, hemicylinder), beam angles, frequencies, and refractive indices must be known. Transmission efficiencies of the visible and IR beams to the interface, SFG transmission efficiency from the interface, and beam overlap are included in calculations of I_{SFG} at buried interfaces. Observation confirms the strong effect of beam angle and sample geometry on SFG intensity (Figure 2.16), which we see in the calculations. It is also important to consider the effect of adding water to the buried interface. Since the difference in refractive index between a substrate (n~1.45) and water (n~1.33) is much smaller than that between a substrate and air (n=1.0), the efficiency of SFG reflection is much lower at the wet interface. This typically results in a reduction in intensity by a factor of five. Sample and beam geometries should be chosen to maximize intensity at the wet interface, where intensity is weakest. I wrote a script to calculate

SFG intensity and coherence length as a function of initial beam angle, IR and visible frequencies, and sample geometry, with frequency dependent refractive index functions for various optical materials.

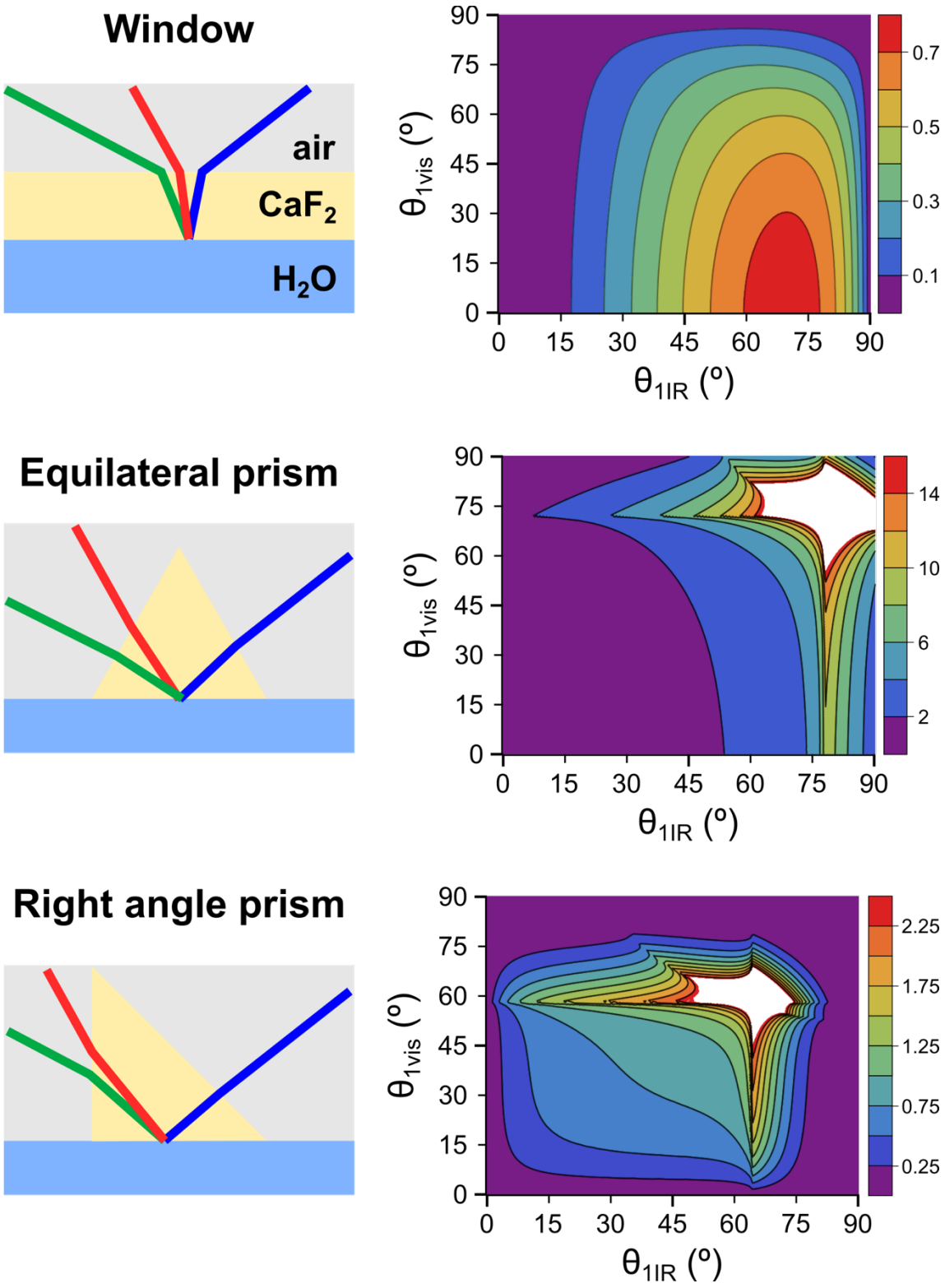

Figure 2.15 Calculated I_{ssp} intensity as a function of visible and IR beam angles in air for the CaF_2/H_2O interface: window, equilateral prism, and right angle prism.

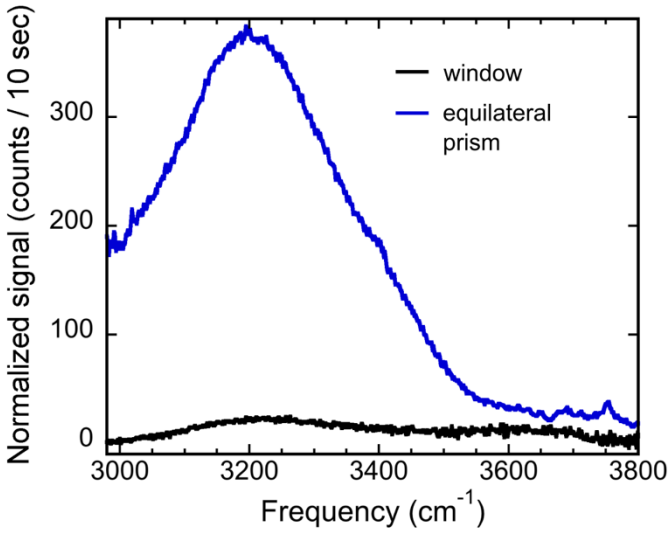

Figure 2.16 SFG spectra of H_2O at two IR fused silica substrates under the same conditions: a window and an equilateral prism.

The relative intensity of different vibrational modes is also affected by the beam angles, accounting for differences in SFG spectra of the same samples after large changes to the SFG setup, and between spectra of the front versus the back side of the same sample. The effect of changing beam angles is dramatic when comparing spectra of OTS at the backside of a window versus a prism. While the beams encounter the sample at the same angle, refraction through the substrate results in very difference incident angles at the interface; the IR and visible are 26.8º and 34.9º at the interface using the window, and 46.4º and 56.6º using the equilateral prism (Figure 2.17).

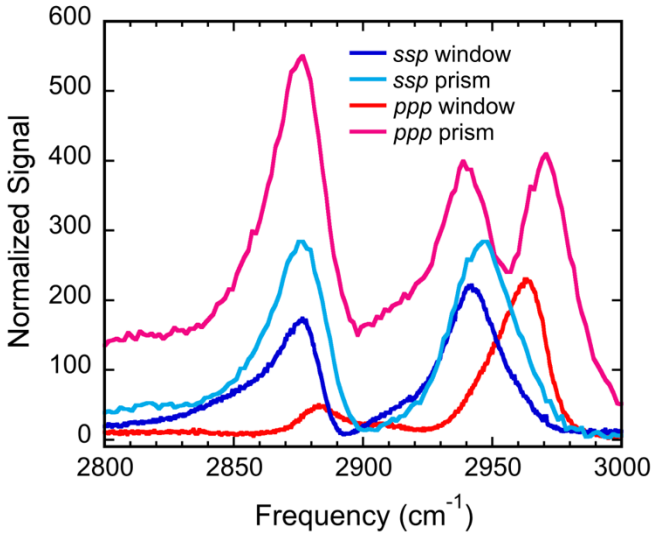

Figure 2.17 Effect of beam angle on SFG spectra of a C18 monolayer in the *ssp* and *ppp* polarizations: window and prism.

While a higher SFG intensity can be achieved by using an equilateral prism instead of a flat window, the prisms have some challenges. They are more difficult to align at the IR/visible overlap, more difficult to mount, cause more "chirp" (or group velocity dispersion), and are roughly ten times more expensive than windows. The last issue can be mitigated by reusing the prisms. Old sample material can be removed from a prism by polishing with a lapping wheel and diamond lapping compound (600 mesh diamond powder). A single prism can be used with multiple samples on flat windows by mating the prism and window with an index matching liquid. The back face of the prism is squeezed against the front side of a window so that light travels uninterrupted through the prism and to the back of the window, the surface of interest. It is necessary to add a material between the prism and the window to prevent reflections at the contact. The bonding material must be thin in consistency, so there is little material to absorb IR light, and not be volatile. KL leak sealant (Kurt Lesker, KL-5) works well.

References

(1) Adamson, A. W.; Gast, A. P. Physical Chemistry of Surfaces. **1997**, *6th ed*.

(2) Tredgold, R. H. Order in Thin Organic Films. **2009**.

(3) Ulman, A. Part One: Analytical Tools. *An Introduction to Ultrathin Organic Films* **1991**, 1–99.

(4) MacPhail, R. A.; Strauss, H. L.; Snyder, R. G.; Elliger, C. A. Carbon-Hydrogen Stretching Modes and the Structure of N-Alkyl Chains. 2. Long, All-Trans Chains. *J. Phys. Chem* **1984**, *88*, 334–341.

(5) Stalder, A. F.; Kulik, G.; Sage, D.; Barbieri, L.; Hoffmann, P. A Snake-Based Approach to Accurate Determination of Both Contact Points and Contact Angles. *Colloids and Surfaces A: Physicochemical and Engineering Aspects* **2006**, *286*, 92–103.

(6) Scherer, J. J.; Paul, J. B.; O'keefe, A.; Saykally, R. J. Cavity Ringdown Laser Absorption Spectroscopy: History, Development, and Application to Pulsed Molecular Beams. *Chem. Rev* **1997**, *97*, 25–51.

(7) White, J. U. Long Optical Paths of Large Aperture. *JOSA* **1942**, *32*, 285–288.

(8) Doussin, J. F.; Dominique, R.; Patrick, C. Multiple-Pass Cell for Very-Long-Path Infrared Spectrometry. *Applied optics* **1999**, *38*, 4145–4150.

(9) Altmann, J.; Baumgart, R.; Weitkamp, C. Two-Mirror Multipass Absorption Cell. *Applied optics* **1981**, *20*, 995–999.

(10) Herriott, D.; Kompfner, R.; Kogelnik, H. Off-Axis Paths in Spherical Mirror Interferometers. *Applied optics* **1964**, *3*, 523.

(11) Greenler, R. G. Reflection Method for Obtaining the Infrared Spectrum of a Thin Layer on a Metal Surface. *Journal of Chemical Physics* **1969**, *50*, 1963–1968.

(12) Balgar, T.; Bautista, R.; Hartmann, N.; Hasselbrink, E. An AFM Study of the Growth Kinetics of the Self-Assembled Octadecylsiloxane Monolayer on Oxidized Silicon. *Surface Science* **2003**, *532-535*, 963–969.

(13) Boyd, R. W. Processes Resulting from the Intensity-Dependent Refractive Index. *Nonlinear Optics* **2008**, 329–390.

(14) Malitson, I. H. Interspecimen Comparison of the Refractive Index of Fused Silica. *Journal of the Optical Society of America* **1965**, *55*, 1205–1209.

(15) Heraeus. Quartz Glass for Optics Data and Properties http://heraeus-quarzglas.com/media/webmedia_local/downloads/broschren_mo/dataandproperties_optics_fused silica.pdf.

(16) Malitson, I. H. A Redetermination of Some Optical Properties of Calcium Fluoride. *Applied optics* **1963**, *2*, 1103–1107.

(17) Dodge, M. J. Handbook of Laser Science and Technology, Volume IV. **1986**, *Optical Materials, Part 2*, 30.

(18) Rivera, C. A.; Fourkas, J. T. Reexamining the Interpretation of Vibrational Sum-Frequency Generation Spectra. *International Reviews In Physical Chemistry* **2011**, *30*, 409–443.

(19) Hirose, C.; Akamatsu, N.; Domen, K. Formulas for the Analysis of Surface Sum-Frequency Generation Spectrum by CH Stretching Modes of Methyl and Methylene Groups. *The Journal of Chemical Physics* **1992**, *96*, 997.

(20) Wang, H.; Velarde, L.; Gan, W.; Fu, L. Quantitative Sum-Frequency Generation Vibrational Spectroscopy of Molecular Surfaces and Interfaces: Lineshape, Polarization, and Orientation. *Annual Review of Physical Chemistry* **2015**, *66*, 189–216.

(21) Zhuang, X.; Miranda, P.; Kim, D.; Shen, Y. Mapping Molecular Orientation and Conformation at Interfaces by Surface Nonlinear Optics. *Physical Review B* **1999**, *59*, 12632–12640.

(22) Boyd, R. W. Nonlinear Optics. **2008**, 1–613.

(23) Wang, H. F.; Gan, W.; Lu, R.; Rao, Y.; Wu, B. H. Quantitative Spectral and Orientational Analysis in Surface Sum Frequency Generation Vibrational Spectroscopy (SFG-VS). *International Reviews In Physical Chemistry* **2005**, *24*, 191–256.

3. Mixed monolayers

3.1. Introduction

Self-assembled monolayers (SAMs) are powerful structures for modifying surfaces.[1–6] A SAM consists of individual monomers, each having a reactive head group that binds to the substrate, a spacer section, and a tail group. The monomers pack together to form a carpet-like structure with the tail group facing away from the substrate. The functional group on the tail can be used to tune the chemical properties of the monolayer, and the length and structure of the spacer helps determine the density and order of the monolayer as well as the orientation of the tail group.[7–12] Monolayers composed of monomers with different lengths can be used create textured surfaces at molecular length scales.[13]

Monolayers are commonly deposited through the adsorption of alkanethiols onto gold, lipids onto a water subphase, and trichloro- or trimethoxysilanes onto silica. Silane monolayers are chemically and thermally robust and can be applied to a wide range of silicate and aluminate materials.[14] Sum frequency generation (SFG) spectroscopy is an ideal technique to characterize SAMs, because it is sensitive to order and surface-specific. By coating a calcium fluoride window with a thin film of SiO_2, we create a substrate which can support the formation of a silane monolayer, while also being transparent to the visible and IR beams of the SFG experiment.[15] A SAM applied to the SiO_2-coated CaF_2 may be probed through the substrate so the buried interface of the SAM and another material, such as water, may be studied.

In the present study, a series of mixed-length alkylsilane monolayers were deposited to create hydrophobic surfaces with smoothly varying disorder. Short chain (dodecyltrichlorosilane, C12)

and long chain (octadecyltrichlorosilane, C18) n-alkane monolayers were formed on SiO_2-coated CaF_2 substrates (Figure 3.1). Fourier-transform infrared spectroscopy (FTIR) was used to characterize the dry monolayers and sum frequency generation (SFG) was used to study the monolayers both in contact with air and with water. Fitting of the C-H stretch region revealed that the pure C18 monolayer is essentially completely ordered, while the pure C12 monolayer exhibits a low amount of disorder, and the mixed monolayers exhibit a large amount of disorder. Furthermore, we observed that the order of the monolayers is unperturbed by contact with water. The intensity of the non-hydrogen-bonded OD stretch was correlated with monolayer surface area, but not order or composition.

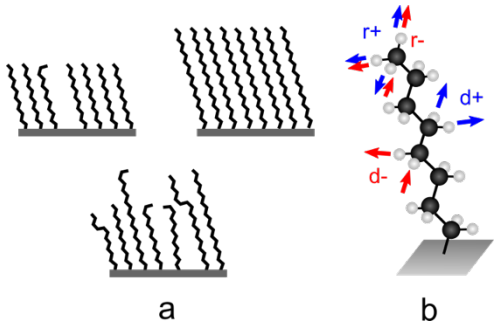

Figure 3.1 (a) Schematic of C12, C18 and mixed C18/C12 monolayers (clockwise). (b) Alkane monomer in trans conformation displaying the methylene and methyl stretching modes probed by FTIR and SFG spectroscopy. Symmetric stretching modes are indicated in blue, and asymmetric modes are indicated in red. Both methylene and methyl modes are FTIR active but only the methyl modes are SFG active in the all-trans conformation.

3.2. Methods

3.2.1. Materials

Octadecyltrichlorosilane (C18, ≥95.0%) and dodecyltrichlorosilane (C12, ≥90%) from Sigma-Aldrich, and hexanes (HPLC grade) from Fisher Scientific, were used as received. Ultra pure

water (18.2 MΩ·cm @25 °C, 5 ppb TOC) was generated in-house using a Milli-Q Advantage A10 system (EMD Millipore). Nochromix cleaning solution was prepared by dissolving Nochromix cleaning reagent (Godax Laboratories) in concentrated sulfuric acid (Fisher Scientific, certified ACS Plus).

3.2.2. Substrates

Optical windows (diameter 25.4 mm, 1 mm thick) of CaF_2 were acquired from CeNing Optics and similarly dimensioned IR fused silica windows were purchased from Crystran Ltd. The CaF_2 windows were coated with 125 nm SiO_2 using an Oxford Instruments ALD FlexAL atomic layer deposition system (110 °C plasma). The substrates were annealed at 800 °C in a high vacuum furnace. A spot of gold was added to both the CaF_2 and IR fused silica substrates to serve as a reference for SFG by first applying a 5 nm thick titanium adhesion layer and then a 150 nm thick gold layer by magnetron argon sputtering through a stainless steel mask. With a skin depth of 16.2 nm for 792.5 nm light and 33.5 nm for 3400 nm light, the titanium adhesion layer does not greatly affect the gold non-resonant SFG response. Microscope slides (VWR) were cut into 25.4 mm square segments.

3.2.3. Monolayer formation

Prior to monolayer deposition, all glassware was soaked in Nochromix solution for at least 45 minutes, rinsed exhaustively with Milli-Q water, and dried, covered, in a 150°C oven for at least an hour. IR fused silica substrates and microscope slide segments were cleaned by the same method. CaF_2 substrates were treated for 10 minutes in a UV/ozone cleaner, rinsed with Milli-Q water, and dried with compressed nitrogen.

Seven solutions of C18 and C12 trichlorosilane monomer mixtures were prepared in hexanes. The total concentration of monomers was kept constant at 2 mM while the mole fraction of C18 was varied from 0 to 1. The trichlorosilanes were added volumetrically by 25-μL glass gastight syringes and mixed thoroughly with the solvent. Substrates were submerged in the solutions and sealed in jars with PTFE-lined caps. After 90 minutes of soaking at room temperature, the substrates (IR fused silica, SiO_2-coated CaF_2, and microscope slide sections) were rinsed with hexanes and then sonicated 15 minutes in hexanes and 15 minutes in Milli-Q water.

3.2.4. Fourier-transform infrared (FTIR) spectroscopy

Initial characterization of the monolayers on microscope slides, IR fused silica, and SiO_2-coated CaF_2 was made using FTIR spectroscopy (Thermo Fisher Nicolet 8700). The monolayer signal was amplified using the White cell described in Chapter 2.3.

All FTIR spectra were fit with four Lorentzian peaks, for the d+ (2850-2855 cm^{-1}), d- (2918-2924 cm^{-1}), r-op (~2958 cm^{-1}), and r-ip (~2963 cm^{-1}) modes and a linear baseline according to Equation 3.1:

$$I_{\mathrm{IR}} = \sum_q \frac{A_q(\Gamma_q/2)^2}{(\omega_{\mathrm{IR}} - \omega_q)^2 + (\Gamma_q/2)^2} + m\omega + b, \qquad \textbf{(3.1)}$$

where A_q is the amplitude, Γ_q the linewidth, and ω_q is resonance frequency for each peak. These parameters were allowed to vary between bounds and fit using a least-squares algorithm. The same starting values and boundary values were used in the fitting of all FTIR spectra.

In Figure 3.2 is the fitting of a pure C18 monolayer showing each peak as well as the overall fit. There appears to be a feature around 2890 cm^{-1} in some of the spectra which may be a r+ or

d+FR mode, but it is too weak and too close to the large d- peak at 2918 cm^{-1} to be included in the fit.

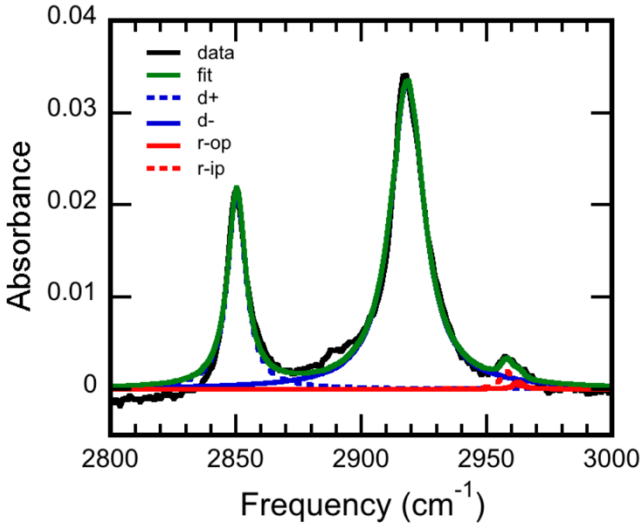

Figure 3.2 FTIR spectrum of 100/0 C18/C12 monolayer showing data and fit

3.2.5. Sum frequency generation (SFG) spectroscopy

The SFG spectrometer consists of a Micra (Coherent) oscillator (800 nm, 80 MHz, 75 nm FWHM, 440 mW) seeding a Legend Elite Duo (Coherent) amplifier (793 nm, 1 kHz, 38 nm FWHM, 25 fs). Before compression, the 5 mJ output of the amplifier was split into three separate beams, each equipped with a compressor. One 800 nm beam (1 mJ) was passed through an etalon (TecOpics, 795 nm, 0.6 nm (10 cm^{-1}) FWHM) and a bandpass filter (Thorlabs, 800 nm, 10 nm FWHM) to produce the upconversion pulse for SFG. A second beam from the amplifier, 3 mJ, was sent to an OPerA Solo (Coherent, tunable 2.6-20 μm, ~230 cm^{-1} FWHM, 30 μJ at 3300 nm) to generate the broadband IR pulse by optical parametric amplification and difference frequency generation with perpendicularly polarized signal and idler in a non-collinear geometry. A 3000 nm longpass filter (Spectrogon) was used for removal of residual signal and idler. The IR (5 μJ) and visible (5 μJ) beams were focused onto the sample at 40° and 55°, respectively, and

overlapped in time to generate the SFG signal. The signal was dispersed by an Acton SP-2500i monochromater (Princeton Instruments, 1800 grooves/mm grating blazed at 500 nm) and collected by a liquid nitrogen cooled Spec-10 CCD camera (Princeton Instruments, 1340×400 pixels). Polarization of the visible and SFG beams could be adjusted by means of a waveplate and polarizer in both beams. Beam polarizations are indicated relative to the sample surface, where a parallel polarization to the surface is 's' and perpendicular is 'p,' and the polarization of the SFG, visible, and IR beams are listed in that order. The *ppp* polarization was used for reference signals on gold, and the *ssp* polarization was used for all samples.

The SFG data was collected for 10-50 averages for the dry and 32-56 averages for the wet of 20 second exposures, alternating sample and background by inserting a 20 ps time delay between the IR and 793 nm upconversion pulse. The optical alignment was optimized using the non-resonant gold signal from the gold spot on each sample. The sample signal was normalized to the gold signal to account for the spectral profile of the IR pulse. The SFG spectra of the dry monolayers were taken at the front surface that the laser beams are incident on, and the SFG spectra of the wet monolayers were taken at the back surface of the monolayer-coated CaF_2 window with the monolayer in contact with either H_2O or D_2O using the liquid cell described in Chapter 2.4. (The front surface SFG spectrum of the 0/100 C18/C12 monolayer was taken of the IR fused silica substrate instead.) The liquids were introduced through PTFE tubing fitted in the holes, and contained between the front and back windows.

All SFG spectra were fit using Equation 3.2,

$$I_{\mathrm{SFG}} = \left| \chi_{\mathrm{NR}}^{(2)} + \sum_{q} \frac{A_q}{\omega_q - \omega_{\mathrm{IR}} - i\Gamma_q} \right|^2 \quad \textbf{(3.2)}$$

where $\chi_{NR}^{(2)}$ is the non-resonant second order susceptibility, A_q is the peak amplitude, ω_q is the resonance frequency, and Γ_q is the line width. A least-squares algorithm was used which allowed the amplitude, frequency, and width of each peak to vary within upper and lower boundaries. Peak amplitudes were allowed to have a positive or negative sign. SFG spectra of mixed monolayers at the dry and H_2O interfaces were fitted with four peaks: d+ (~2852 cm^{-1}, positive), r+ (~2875 cm^{-1}, positive), d+FR (2915 cm^{-1}, positive), and r+FR (2935 cm^{-1}, positive). Spectra of monolayers at the interface with D_2O (Figure 3.3) were fitted with two additional peaks: the H-bonded OD stretch (~2580 cm-1, positive), and the free OD stretch (~2722 cm-1, negative). All spectra of mixed monolayers at each single interface (air, D_2O, or H_2O) were fit simultaneously so that the starting values and upper and lower bounds for each variable were the same. However, the fitting conditions were slightly different between different interfaces. Confidence intervals for each fitted value were calculated from the Jacobian and propagated to find the 95% confidence intervals for peak areas.

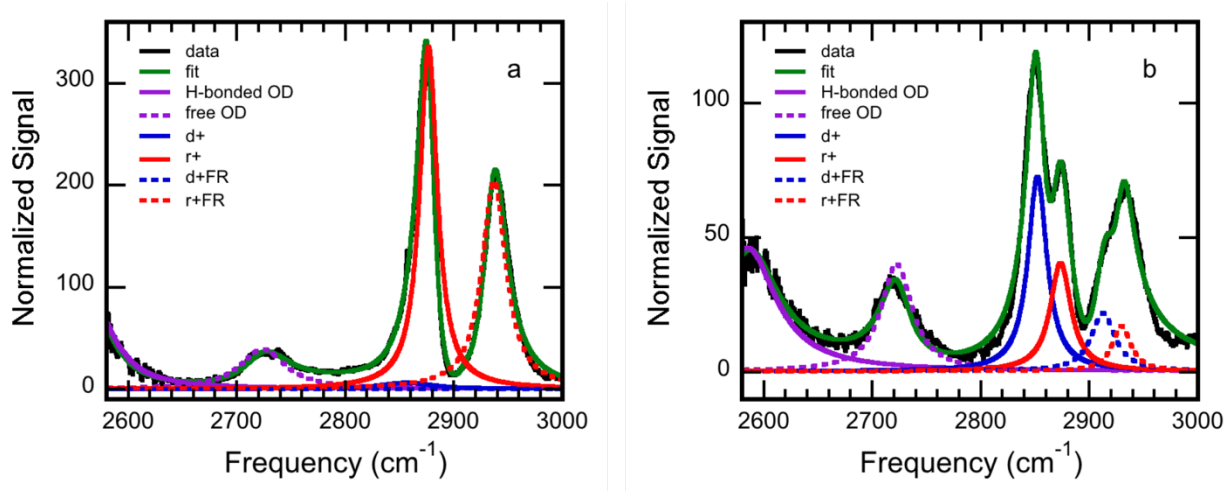

Figure 3.3 SFG spectra of C18/C12 mixed monolayers at the interface with D_2O showing data, fit, and individual peaks: (a) 100/0, and (b) 50/50.

3.2.6. Atomic force microscopy (AFM)

AFM was used to characterize the surface structure of the monolayers. A Digital Instruments Dimension 3100 microscope was used with MikroMasch probes (HQ:NSC15/Al BS, 325 kHz, 40 N/m) in tapping mode. Images were collected for 1 μm and 10 μm square regions. NanoScope Analysis v1.40 software (Bruker) was used to process the images and calculate root mean square (RMS) roughness and surface area (SA) difference values. Image statistics were computed using the 10 μm square scans. Height values above 3 nm were excluded from the calculations to improve consistency, but the same trends in roughness and surface area were observed without thresholding.

3.3. Results

3.3.7. FTIR

The FTIR transmission spectra of the dry monolayers, shown in Figure 3.4, are dominated by the methylene symmetric stretching (d+, 2850 cm^{-1}) and methylene asymmetric stretching (d-, 2918

cm^{-1}) modes. The methyl asymmetric stretching modes r- out of plane (r-op, 2958 cm^{-1}) and r- in plane (r-ip, 2963 cm^{-1}) are also clearly resolved, but the methylene symmetric Fermi resonance (d+FR, 2895 cm^{-1}) and methyl symmetric stretching (r+, 2870 cm^{-1} and r+FR, 2935 cm^{-1}) modes are not visible.[16–18] FTIR spectra were consistent for each C18/C12 composition regardless of the substrate (microscope slide, SiO_2-coated CaF_2, and IR fused silica). The most obvious change in the FTIR spectra is a reduction in the overall intensity as the C18 fraction decreases, particularly in the methylene modes. As the fraction of C18 monomers decreases, the average number of methylene units per monomer decreases. However, there is still one methyl unit per chain. A decrease in the r- peak height with decrease in C18 fraction indicates that the monolayer density is decreasing and/or that the orientation of the monomers is changing as a function of composition.

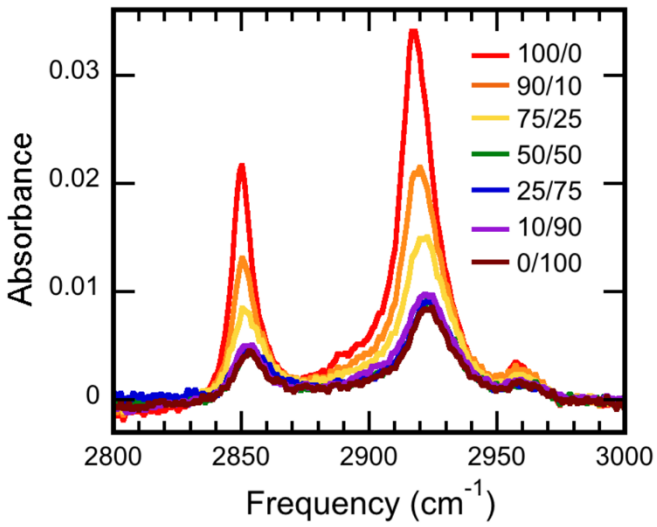

Figure 3.4 FTIR transmission spectra of mixed monolayers with different C18/C12 percentages.

Accompanying the changes in the peak intensities are red shifts of the methylene peaks by up to 5 cm^{-1} (Figure 3.5). An increase in the d+ and d- frequencies is a signature of a higher occurrence of gauche defects in the monolayer and thus indicates disorder.[18–22] The d+ and d- frequencies

are lowest for the pure C18 monolayer, reach a maximum for the mixed C18/C12 monolayers, and exhibit another local minimum for the pure C12 monolayer. This suggests that the disorder is highest for the mixed monolayers.

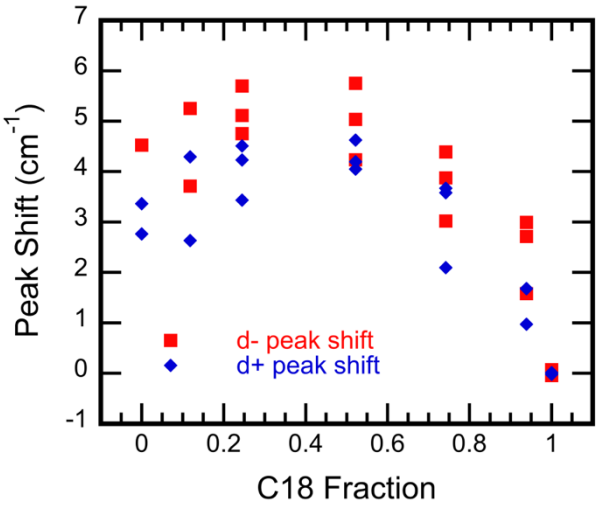

Figure 3.5 Peak shift of methylene stretch modes in the FTIR spectra, relative to the mean peak frequency of C18.

The peak areas of the fitted FTIR spectra as a function of C18 fraction are shown in Figure 3.6. The combined peak areas of the r-ip and r-op modes were calculated by integrating from 2951-2975 cm^{-1} in the FTIR spectra, setting the baseline to zero at the same endpoints to remove overlap from the d- peak. Methylene modes areas were taken from the fitting described above. All peak areas are normalized to the corresponding peak area for the pure C18 monolayer (Figure 3.6 a), and d+ and d- are then additionally normalized to the average number of methylene groups per monomer (Figure 3.6 b). That is, the normalized d+ and d- values in Figure 3.6 b represent the peak area per methylene group relative to the C18 monomer. All modes follow the same trend, decreasing sharply in intensity with decreasing C18 fraction, coming to a slight minimum around a C18 fraction of 0.5, and increasing slightly towards pure

C12. The peak area fraction for r- does not stay at one as the C18 fraction decreases, indicating a change in average chain tilt or monolayer density.

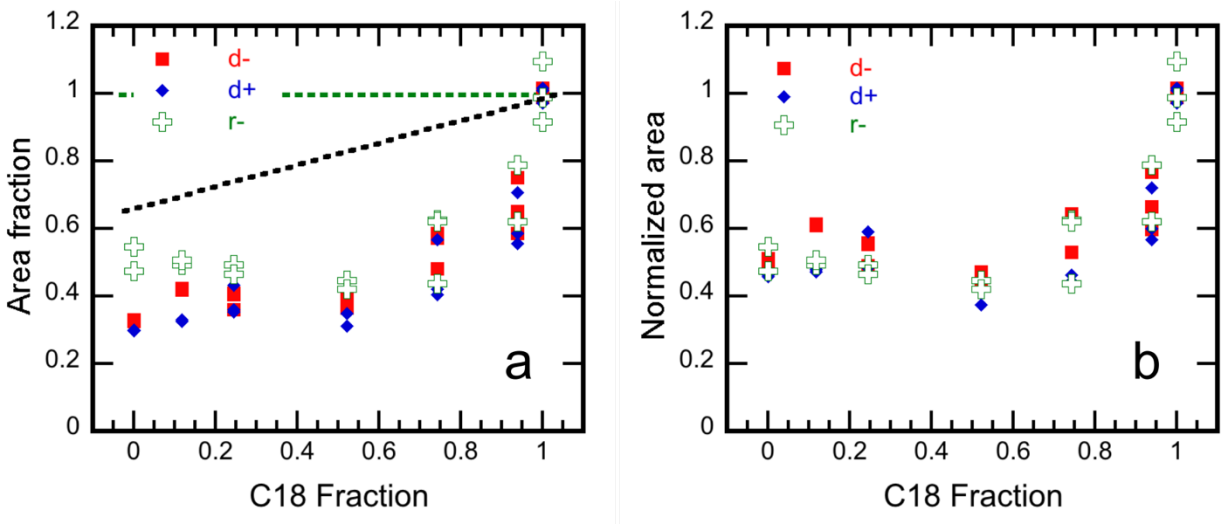

Figure 3.6 FTIR mode areas normalized to average area for pure C18 (a) The black dotted line indicates the average number of CH_2 groups per monomer normalized to C18, and the green dotted line indicates the number of CH_3 groups per monomer. (b) Methylene mode areas are additionally divided by average number of CH_2 groups per monomer.

3.3.8. SFG

3.3.8.1. Monolayers

The CH vibrational region of both dry and wet monolayers were studied in the *ssp* and *ppp* polarization with SFG, shown in Figure 3.7 and Figure 3.8. Each spectrum can be interpreted as a convolution of a non-resonant signal and Lorentzian peaks for the CH vibrational modes: d+ (2853 cm^{-1}), r+ (2878 cm^{-1}), d- (2885 cm^{-1}), d+FR (2918 cm^{-1}), r+FR (2941 cm^{-1}), and r- (2960 cm^{-1}).[23–25] The peak assigned as d+FR[26] is sometimes attributed to the d-(π) or d- resonance instead.[23,27] In either case, it is a methylene mode and the specific assignment does not change the analysis. Four modes are prominent in the *ssp* polarization, and all have a positive sign: d+, r+, d+FR, and r+FR. The *ppp* spectra are more difficult to fit with five modes visible, and these have a mixture of positive and negative signs: d+ (+), r+ (+), d- (–), d+FR (+), and r- (–).

Although an analysis of the *ppp* spectra leads to the same conclusions, only the *ssp* spectra will be discussed as the quality of the fit is better.

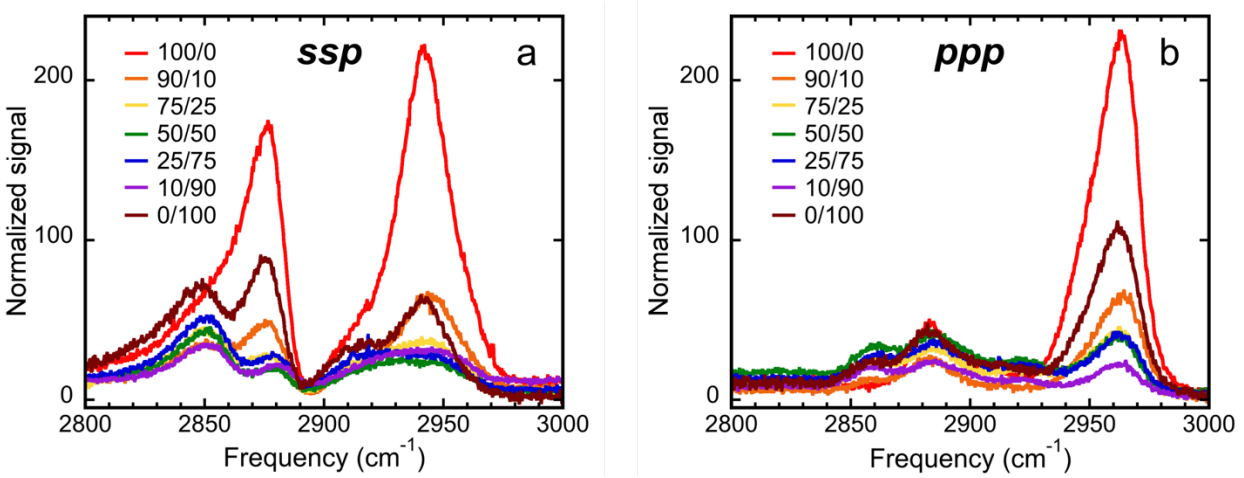

Figure 3.7 SFG spectra of dry monolayers with different C18/C12 percentages with the (a) *ssp* and (b) *ppp* polarization. Spectra were taken at the front side, monolayer/air interface.

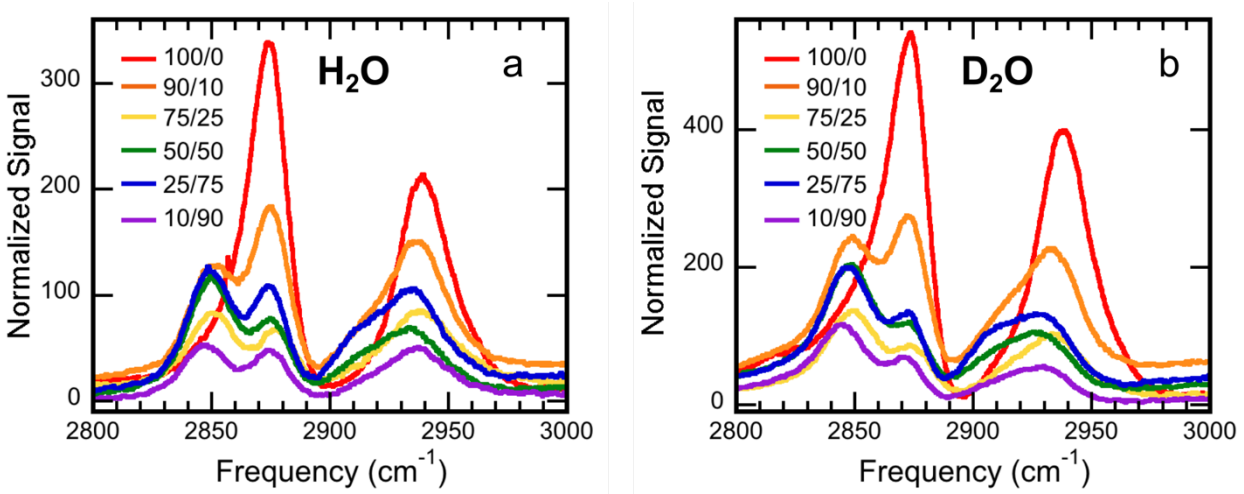

Figure 3.8 SFG spectra of mixed C18/C12 monolayers at the buried interface in the *ssp* polarization: (a) wetted with D_2O, and (b) wetted with H_2O.

We further quantify the disorder of the monolayers with SFG that, by symmetry, is very sensitive to the disorder of the monolayer, and can be used to probe both dry and wet monolayers. SFG is interface-specific due to two symmetry requirements. Firstly, a vibrational mode must be both IR and Raman active to act as a SFG emitter. This requires the molecular structure participating in

the vibrational mode to lack inversion symmetry. Secondly, the second order susceptibility must add constructively within the coherence length to generate a signal. This requires the distribution of SFG emitters to be non-centrosymmetric to create an overall SFG signal. The symmetric methyl stretch is SFG allowed for each molecule because it has a nonzero transition dipole moment and polarizability and is thus both IR and Raman active.[28] In a well ordered monolayer, all the methyl groups point up in the same direction. Therefore, the r+ second order susceptibilities add constructively giving rise to an overall large SFG signal. The d+ mode is also allowed by the molecular requirement. However, for a monomer in the all-trans configuration, each methylene group on an alkane chain faces away from the adjacent one (Figure 3.1 b). Consequently, the methylene signals cancel out pairwise and no overall SFG signal is observed. However, if there is a gauche defect in the alkane chain, there is an incomplete cancelation of the d+ mode and it will appear on the SFG spectrum. Furthermore, a gauche defect causes the methyl group on the tip of a monomer to change orientation leading to a partial cancelation of the r+ and the r+FR signals.[29] A single gauche defect flips the orientation of the methyl group by roughly 140 °. Characterizing the methyl and methylene intensities in the SFG spectrum thus gives a direct measure of the disorder of the monolayer.[13,29–31]

The pure C18 monolayers have the strongest r+ and r+FR peaks and almost no intensity for the methylene modes. This is consistent with a highly ordered monolayer with negligible gauche defects. As the C12 fraction increases, however, we see the r+ modes decrease and the methylene modes appear due to disordering of the monolayer. The results of the spectral fitting are shown in Figure 3.8. If we define the disorder parameter as the fraction of peak area from methylene modes out of all the CH stretches, we see that the disorder is minimal for the pure C18 monolayer and limited for the pure C12 monolayer, while a large disorder is observed for most

of the mixed monolayers. Furthermore, the monolayer disorder is the same for monolayers in contact with air, H_2O and D_2O. Although there is no significant difference between the wet and dry monolayers in ordering, the wetted monolayers have a higher intensity in the r+ compared to the to the r+FR peak. We note that the monolayer disorder also affects the overall SFG intensity. SFG is a coherent spectroscopy with a remarkable sensitivity to order, as described above. For disordered monolayers there is a large cancelation of overall SFG intensity due to the destructive interference among the differently orientated transition dipoles. In the limit of a completely disordered monolayer exhibiting inversion symmetry, no SFG intensity is observed. Accordingly, the drop in overall SFG intensity moving from pure C18 to the mixed monolayers is due to an increase in disorder. SFG intensity rises again for the pure C12 monolayer as some order is recovered.

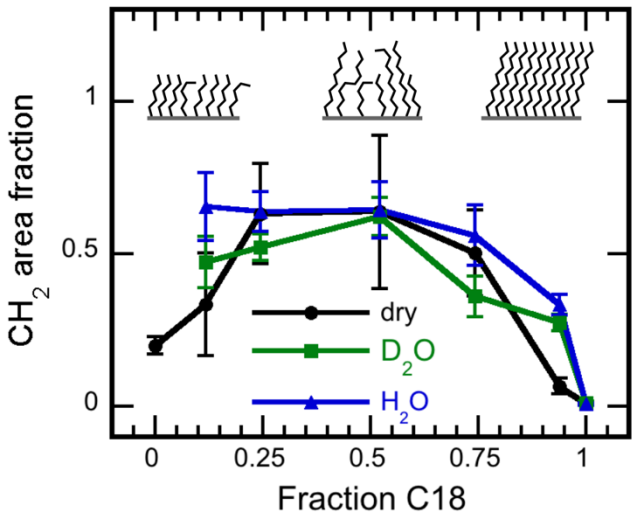

Figure 3.9 Area of CH_2 peaks as a fraction of total CH stretch mode area for different C18 mole fractions. Areas were determined from fits of SFG spectra of dry and wet monolayers. Error bars are ± 95% confidence intervals

We also observe significant red shifts of the CH stretching modes due to the change in dielectric environment: the r+FR mode is red-shifted by 10 cm^{-1}, the r+ mode by 4 cm^{-1}, the d+FR mode by 7 cm^{-1}, and the d+ mode by 2 cm^{-1}.

3.3.8.2. Water at monolayers

Perturbation of water structure by the C18/C12 monolayers was observed. The buried monolayer/D_2O interface was probed by SFG down to 2600 cm^{-1} in *ssp* to cover the free (not hydrogen-bonded) OD stretch at ~2750 cm^{-1} (Figure 3.10). The tail of the H-bonded OD stretch can be seen at lower frequencies. Free OH bonds are characteristic of water at hydrophobic surfaces, where the H-bonded structure of bulk water must terminate, but where water cannot form hydrogen bonds to the other phase. The non-hydrogen bonded OH stretching mode is well documented for the water interface with air, hydrophobic liquids, and hydrophobic monolayers.[8,29,32–35] While all of the C18/C12 monolayers are hydrophobic, there is a large variation in the intensity of the free OD peak, and this intensity is not correlated with C18 fraction or with monolayer order (Figure 3.11). An SFG study of C18 monolayers with varying degrees of order did observe a correlation, finding that the strength of the free OH peak increased with monolayer disorder.[29] It is plausible that, for pure C18 monolayers, order and surface roughness are correlated and therefore it only appeared that the two were directly linked.

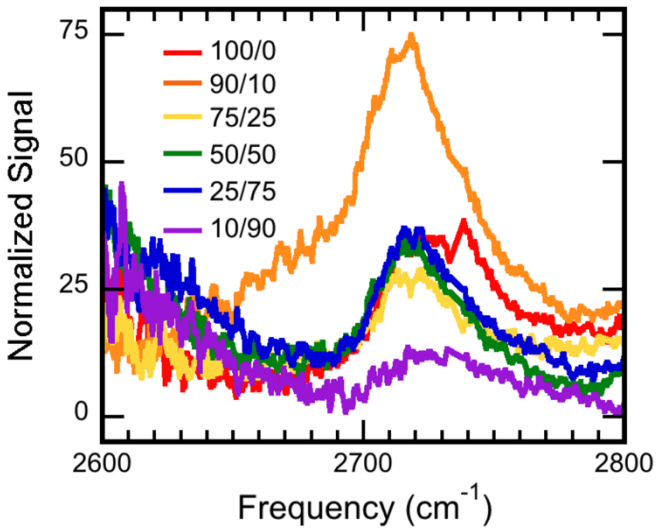

Figure 3.10 SFG spectra of free OD peak (D_2O) at mixed monolayers, *ssp* polarization.

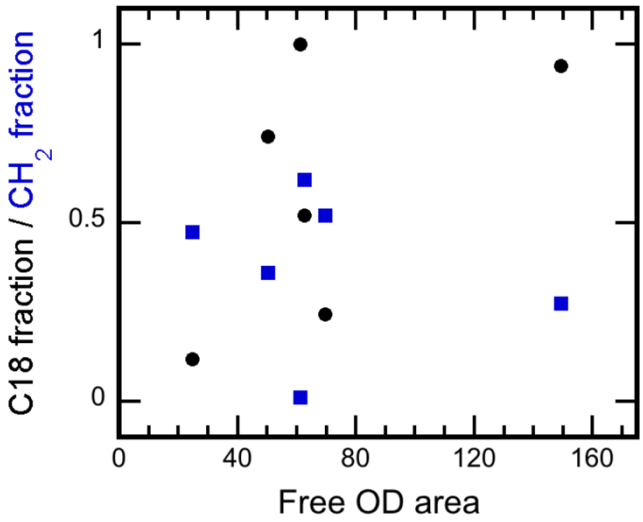

Figure 3.11 C18 fraction and monolayer order parameter (CH_2 area fraction) as a function of free OD peak area.

3.3.9. AFM

The AFM images in Figure 3.12 a and d show the texture of clean IR fused silica substrate without a monolayer. We see scratches of less than 1 nm in depth, digs (pits) of around 1 nm, as well as several round features much more than 3 nm in height. The scratches and digs are present on some of the monolayers as well. They may be dust particles or polishing debris. Figure 3.12 b

and e show an IR fused silica window with a pure C18 monolayer adsorbed. The scratches and round features from the underlying substrate are visible. In addition, the monolayer has depressions of 3 nm in depth (shown in green), some round and some elongated. These pits may be defects in the monolayer where monomers are absent, since 3 nm is approximately the height of an extended C18 monomer. This value is close to the thickness of a C18 siloxane monolayer as determined by ellipsometry, 2.7 nm,[36] grazing-angle X-ray reflectivity, 2.6 nm,[37] and the calculated maximum thickness, 2.6 nm.[22] In Figure 3.12 c and f we see a mixed monolayer of half C18 and half C12 (50/50 C18/C12). It looks similar to the pure C18 monolayer, but there are more depressions of 3 nm in depth, and there are also smaller, round depression of ~ 1 nm in depth and ~20 nm in diameter. It is possible that the later indicate isolated pockets of C12 monomers surrounded by C18, but no extensive domain boundaries are apparent: lines at which the height abruptly changes by around 1 nm, the height difference between C18 and C12 monomers.[36] On the length scale of ~25 nm to 10 μm, there do not appear to be discrete C12 and C18 domains.

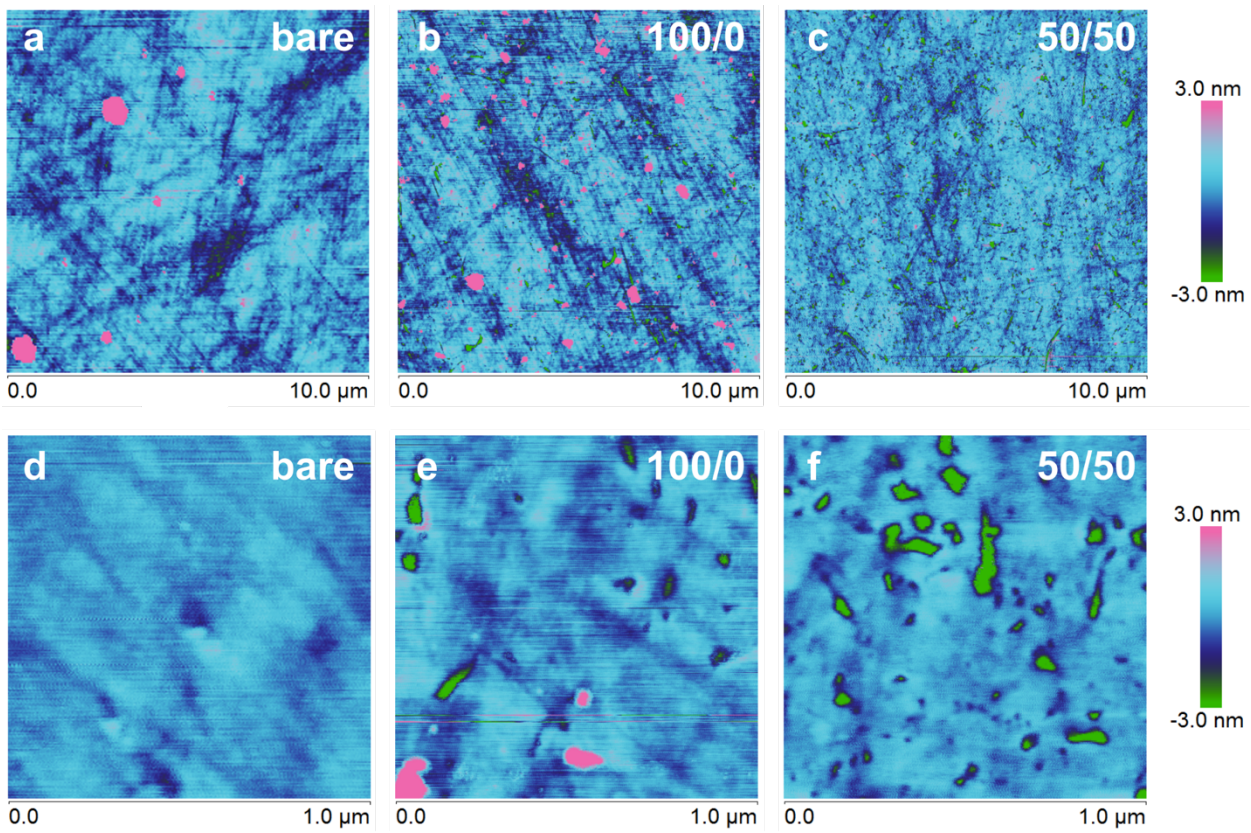

Figure 3.12 AFM images of clean IR fused silica substrate with no monolayer (a and d), with pure C18 monolayer (b and e) and 50/50 C18/C12 mixed monolayer (c and f). Images were acquired at two length scales: (a-c) 10 × 10 µm, and (d-f) 1 × 1 µm.

All three 10 μm images of the 100/0 monolayer have a repeating feature in the height distribution which appears in none of the other monolayers (Figure 3.13). (This feature is too small to have a significant effect on the roughness values.) Peaks in the height distribution occur at heights of 5, 10, and 16 nm and decrease in intensity with height. The peaks may indicate the presence of C18 bilayer stacks. Unbound C18 monomers are amphiphilic, having a hydrophobic tail with an affinity for other alkane chains, and hydrophilic silane group which can crosslink with other silanes. The positions of the peaks in the height distribution can be explained by stacks of C18 bilayers adsorbed to the substrate, as shown in Figure 3.14, with a bilayer thickness of 5.3 nm and a monolayer thickness of 2.7 nm. This height is consistent with both the thickness of C18 monolayers in the literature[22,36,37] and the depressions seen in Figure 3.12 b and

e. Bilayers may form directly at the substrate, or sheets of cross-linked monolayer sheets may assemble in solution and later adsorb at the substrate. The later was proposed as a mechanism for C18 monolayer assembly.[38]

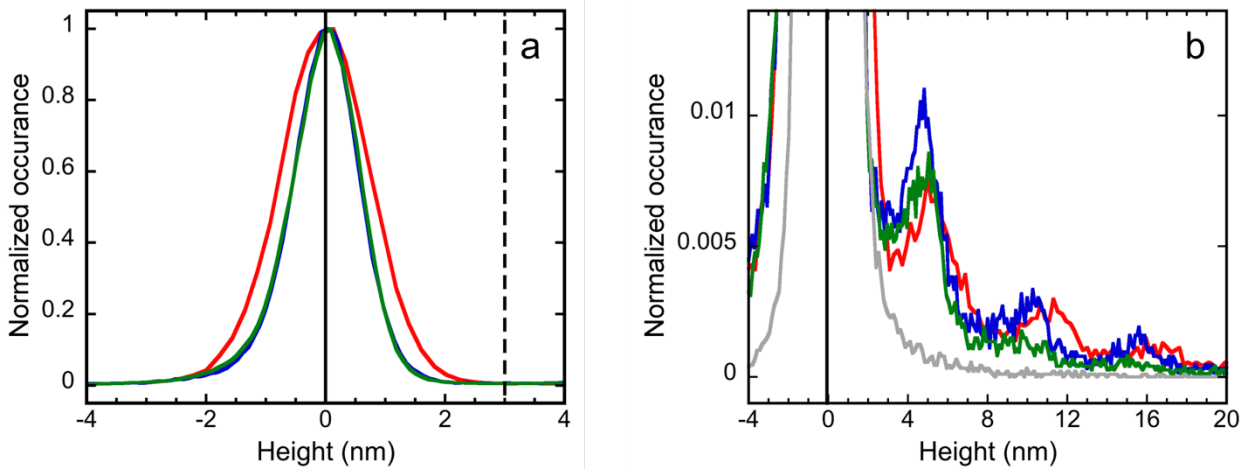

Figure 3.13 Height distribution of 100/0 monolayers from 10 × 10 μm AFM images. (a) Distributions from three different spots, compared to average (solid line, height=0) and 3 nm cutoff (dotted line). (b) Height distributions of same 100/0 samples (red, blue, green) showing multilayers. Compare with 75/25 monolayer (gray) lacking this feature.

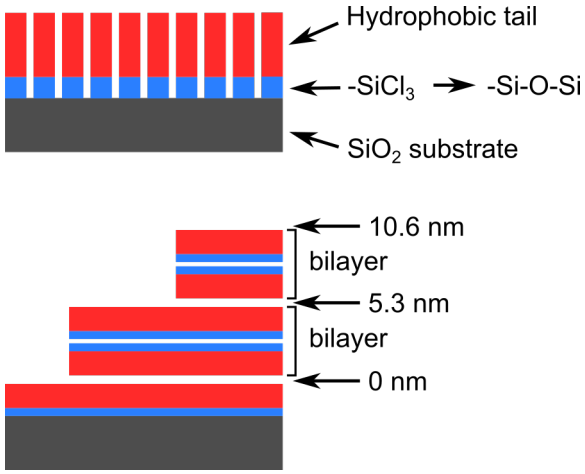

Figure 3.14 Proposed C18 bilayer stacking and height of features.

While neither C18 fraction nor monolayer order are correlated with the area of the free OD peak, there is a positive relationship between the free OD and both roughness and surface area as

determined by AFM (Figure 3.15). As the surfaces are very smooth, the surface area is given as the surface area (SA) difference, the difference between actual and projected surface area as a fraction of the imaging plane area. Data were acquired in two time periods: just before SFG characterization, and several months later. Calculations of roughness and surface area from these times are consistent except for the 90/10 monolayer, which has the highest free OD area. For this sample, the single early measurement of roughness was correspondingly high, and we find a linear relationship between roughness and peak area. Later measurements repeatedly found a much lower roughness. It is possible that the monolayer annealed somewhat in the interim, or that the surface was heterogenous. The positive trend remains without this point, however.

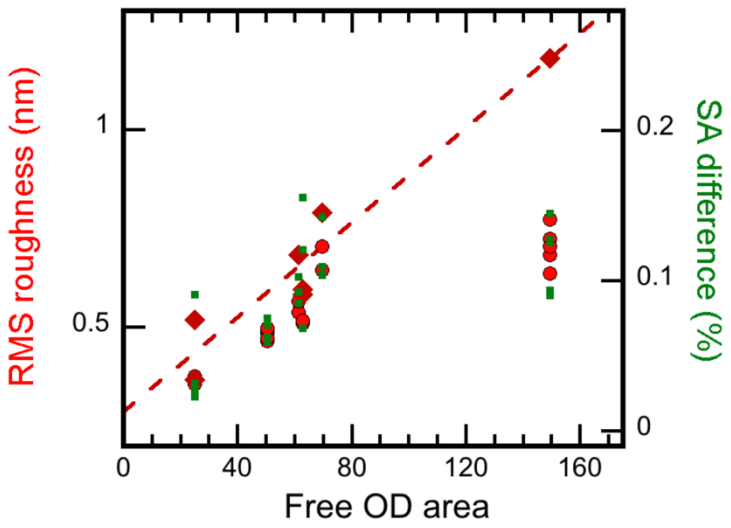

Figure 3.15 Root mean square (RMS) roughness and surface area (SA) difference of monolayers as a function of free OD peak area. Roughness measurements taken just before SFG spectra shown as dark red diamonds, those three months after as bright red circles. Red dotted line is a linear fit to early roughness values. SA difference shown as small green squares. One point (OD area 149, SA difference 0.67) is off the scale.

3.4. Discussion

The goal of this study was to determine the relationship between the composition of the C18/C12 mixed monolayer and monolayer disorder, and the effect of that disorder on water structure. Since the monolayers were deposited by competitive adsorption from solution, one cannot automatically assume that the solution and monolayers have the same C18/C12 fraction. Multiple studies have found that, for mixed n-alkanethiol monolayers on gold, the longer chains are preferentially adsorbed.[39–41] Alkylsilane monolayers do not appear to follow the same trend, however. A study of mixed monolayers of methyltrichlorosilane (C1) and octadecyltrichlorosilane (C18) found that the monolayer was enriched in C1 over the entire range of composition.[13] However, this is a very large difference in chain length. A study more applicable to ours investigated binary n-C4/C8, n-C4/C12, n-C4/C16, and n-C4/C18 silane monolayers.[12] No preference in chain length was detected. When an analogous series of monolayers using t-butyltrichlorosilane (t-C4) instead of n-C4 was prepared, there was a deficiency of t-C4 in the monolayers. It seems that, apart from systems involving extreme chain length differences such as C1 and C18, the relevant factor in determining alkylsilane monolayer composition is monomer cross-section, not length. It is reasonable to expect C18/C12 monomers to adsorb at approximately the same ratio as in the parent solution.

The disorder of silane monolayers depends critically on the deposition conditions, with particular sensitivity to solution temperature and substrate moisture content.[11,38,42,43] When a hydrated substrate is used, it will be coated with several layers of water molecules which will hydrolyze the chlorines in the trichlorosilane.[44] The water can act similarly to the bulk water subphase supporting a Langmuir-Blodgett film.[11,14] Since the water molecules in the topmost layer are only weakly coupled to the silica substrate, monomers are initially free to diffuse along the

surface. Eventually the silane groups will crosslink, essentially freezing the monomers in place. Depending on deposition temperature and monomer density, the films can exist in gas (G), liquid expanded (LE), and liquid condensed (LC) phases, in order of increasing density. LC phases are characterized by trans conformations of the alkane chain, while rarer LE and G phases have more gauche defects. At deposition temperatures above a monomer's critical temperature (T_C), the film progresses from G to coexisting LE+G to homogeneous LE. The film may not progress to coexisting LC+LE before siloxane bond formation to substrate and neighboring silanes, locking in the structure. At lower deposition temperatures, below T_C, LC and G phases initially coexist before becoming fully LC.[11,22,45,46] As a result, monolayers deposited below T_C exhibit a higher order than monolayers deposited above it.[11] The T_C of C12 and C18 are about 18 °C and 30 °C, respectively, which are below and above the temperature of deposition.[45] The fact that C12 was deposited at a temperature above its T_C, while C18 was deposited below its T_C, explains the higher degree of disorder observed for the C12 monolayer.

The overall intensity of the FTIR spectrum drops significantly from pure C18 to about 50/50 mole fraction and then stays approximately constant to pure C12. If there were no change in the monolayer density or average chain tilt, then the r- modes should stay constant and the d+ and d- modes should drop linearly by a factor of 11/17 from pure C18 to pure C12. The observed intensity drop for all modes is larger than this prediction, indicating either a change in monolayer density or average chain tilt. For an ordered monolayer with monomers nearly perpendicular to the surface, as in the C18 case, the transition dipole moments of the CH_2 stretching modes (d- and d+) as well as the asymmetric CH_3 stretching mode (r-) are all nearly parallel with the surface. Therefore, an orientational change of the monomers will decrease the peak areas of the CH_2 and asymmetric CH_3 modes. If the CH_2 peak areas are normalized to compensate for the

average number of methylene groups per monomer (i.e. a drop by 11/17 from pure C18 to pure C12), then the dependence on the composition mirrors that of the r- areas (Figure 3.6). Either a change in monolayer density or a change in orientation could explain the observed change in intensity. However, there is a cosine-squared dependence between signal intensity and the change in the orientational angle of the monomer. For a chain oriented near normal, as the case of the pure C18 monolayer, a 45º change in chain tilt would be necessary to explain the observed change in peak area. Such an orientational change would also result in a significant r+ peak, which has a transition dipole moment parallel to the chain axis and would not be visible for a chain normal to the substrate. Since an r+ peak is not observed it strongly indicates that the intensity change is not due to a large orientational change. Lastly, studies examining Langmuir-Blodgett films of fatty acids and alcohols at different liquid phases suggests that the reduction in FTIR signal[47,48] and SFG methyl stretch peak intensity[49] accompanying a transition to a less dense phase is primarily due to presence of fewer molecules (lower density), not a change in orientation. Therefore, density is more likely to be responsible for the drop in intensity, especially considering that the lower melting point of C12 should result in a less condensed phase. We interpret the drop in the peak intensities in the FTIR spectra from pure C18 to 50/50 as resulting mainly from a change in monomer density that then stays fairly constant to pure C12.

While the pure C12 monolayer is slightly more disordered than the pure C18 monolayer, the mixed monolayers exhibit a much higher degree of disorder that appears weakly dependent on the composition. Monolayer order can vary between synthesis runs,[29] and so can the exact shape of the disorder curve with respect to composition. However, the disorder of the mixed monolayers is always greater than that of the pure monolayers. The greater disorder for the

mixed monolayers is likely caused by the reduction of lateral chain-chain interaction for the upper half of C18 monomers which are adjacent to C12, instead of other C18, monomers. Since there is a smaller free energy penalty for the protruding end of the C18 chain to assume a gauche conformation, there is a higher occurrence of disorder in regions of chain length mismatch.[50,51] This configuration would be rare for a mixed monolayer separated into macroscopic domains of pure C12 and C18, because the number of monomers at domain boundaries would be so small. If the domains were large, then a linear relationship between disorder and C18 mole fraction would be expected. Our SFG and AFM results are consistent with complete mixing or small scale domains. Order is partially recovered for the pure C12 monolayers as there is no longer any length mismatch and the occurrence of chain kinks is less favorable.

A study of fatty acid Langmuir-Blodgett films found that binary mixtures of tetradecanoic (C14) and eicosanoic (C20) acid on water are highly nonideal and immiscible in many proportions.[52] Taken together with data from other binary systems, the study suggests there is a large positive free energy of mixing for a 1:1 mole ratio of tetradecanoic and eicosanoic acid, which should lead to domain formation. Two studies of mixed monolayers have in fact found evidence for partitioning.[39,53] An AFM study of a 1:1 mixed C18/C12 alkylsilane monolayer (formed by the drawing-up method from a Langmuir-Blodgett film at 293K) shows domains of LC C18 appearing in round islands around 2 μm in diameter, with the C12 in a more expanded state surrounding them.[53] However, given domains of this size and shape, only about 0.1% of C18 monomers would lie at a domain boundary. Other mixed monolayer studies have not found evidence of discrete domains, or could not distinguish between small domains and complete mixing.[12,13,40]

Our AFM images of the C18/C12 mixed monolayers support the conclusion that there are no large C18 domains in the monolayers prepared here. No domain boundaries can be resolved at a length scale between 10 μm and 25 nm. The discrepancy between the Langmuir-Blodgett films and the results of this and other studies is not too surprising. The free energy of mixing is highly dependent on temperature and surface pressure/monolayer density.[52,54,55] Also, while alkylsilane monolayers and Langmuir-Blodgett films have some similarities, the formation of the alkylsilane monolayers is time limited by the cross-linking of the silane groups. There may not be enough time for the monolayer to come to equilibrium.

Previous studies of well-ordered alkanethiol and alkylsilane monolayers have found that there is little disorder induced upon bringing the monolayers into contact with water,[29,56–58] but that if the monolayer was disordered to begin with, wetting increased the disorder.[30,59,60] We observe no significant change in the disorder of the monolayers when wetted with H_2O or D_2O across all C18 fractions. The large redshift of r+FR by ~ 10 cm^{-1} and a smaller shift of r+ by ~4 cm^{-1} observed in the wetted monolayers is consistent with previous FTIR,[56] SFG,[29,30,58,59,61] and DFT[58] studies, which found a redshift of as much as 15 cm^{-1} in the CH_3 stretch frequencies as water was brought closer to the terminal methyl groups.[58] Redshifting of the CH_3 modes occurs to a similar extent in solvents over a range of polarities (e.g., water, acetonitrile, CCl_4, d-hexadecane) pointing to a dispersion interaction rather than a dielectric effect.[29,30,56,61]

Free OD peak intensity is linear with monolayer roughness and surface area, suggesting that the extent of interface, rather than the nature of the water/monolayer interaction, determines the strength of the mode. This interpretation is further supported by the free OD peak frequency. The frequency of a free OH peak is related to the strength of the dipole-dipole interaction with the hydrophobic phase, a stronger interaction leading to a lower frequency. For instance, the free OH

mode has a frequency of 3706 cm^{-1} at air, where there is no interaction, but decreases to 3673 cm^{-1} at a C18 monolayer (shift of ~30 cm^{-1}).[8] For D_2O at C18/C12 mixed monolayers, the free OD peak appears at ~2719 cm^{-1}, which is redshifted from the free OD at air (~2750 cm^{-1})[62,63] by a similar amount. That the frequency of the free OD is the same for all monolayers indicates that the degree of water interaction with the monolayer is insensitive to the differences between the monolayer series.

3.5. Conclusions

In this project we have examined the disorder of mixed-length monolayers deposited on IR- and visible-transparent substrates as a function of the composition. The disorder of the dry and wet monolayers was characterized by FTIR (dry) and SFG (dry and wet) spectroscopy. While the pure C18 monolayer contained virtually no disorder, the pure C12 monolayer exhibited a small degree of disorder. This is likely because the monolayers were prepared at a temperature which was below the T_C of the C18, but above the T_C of the C12 monomers. The mixed-length monolayers, on the other hand, were found to be much more disordered than the pure monolayers. This is likely due to the higher conformational freedom (and therefore greater number of gauche defects) of the termini of C18 monomers adjacent to C12 monomers or pinhole defects. This in turn suggests a monolayer structure not composed of large macro-scale domains of pure C18 and pure C12, but either small domains or homogeneous mixing. AFM images confirm that such domains, if they exist, must be smaller than 25 nm. We further found that wetting the monolayers with H_2O and D_2O did not affect monolayer disorder over most of the C18/C12 mixtures.

A large variation was observed in the intensity but not the frequency of the non-hydrogen-bonded "free" OD peak of D_2O at different C18/C12 monolayers. Free OD intensity was correlated with surface roughness rather than monolayer disorder. Taken together, the fact that monolayer order was not affected by wetting, and free OD intensity and frequency was invariant with monolayer order, indicates that there is only a weak interaction between the water and the monolayer. The response of the non-hydrogen-bonded OD groups at the monolayers is governed only by the size of the interface.

References

(1) Rozkiewicz, D. I.; Jańczewski, D.; Verboom, W.; Ravoo, B. J.; Reinhoudt, D. N. 'Click' Chemistry by Microcontact Printing. *Angewandte Chemie International Edition* **2006**, *45*, 5292–5296.

(2) Stokes, G. Y.; Buchbinder, A. M.; Gibbs-Davis, J. M.; Scheidt, K. A.; Geiger, F. M. Chemically Diverse Environmental Interfaces and Their Reactions with Ozone Studied by Sum Frequency Generation. *Vibrational Spectroscopy* **2009**, *50*, 86–98.

(3) Love, J. C.; Estroff, L. A.; Kriebel, J. K.; Nuzzo, R. G.; Whitesides, G. M. Self-Assembled Monolayers of Thiolates on Metals as a Form of Nanotechnology. *Chemical Reviews* **2005**, *105*, 1103–1169.

(4) Schreiber, F. Structure and Growth of Self-Assembling Monolayers. *Progress in surface science* **2000**, *65*, 151–257.

(5) Heydari, G.; Thormann, E.; Järn, M.; Tyrode, E.; Claesson, P. M. Hydrophobic Surfaces: Topography Effects on Wetting by Supercooled Water and Freezing Delay. *The Journal of Physical Chemistry C* **2013**, *117*, 21752–21762.

(6) Liu, Y.; Ogorzalek, T. L.; Yang, P.; Schroeder, M. M.; Marsh, E. N. G.; Chen, Z. Molecular Orientation of Enzymes Attached to Surfaces through Defined Chemical Linkages at the Solid-Liquid Interface. *J. Am. Chem. Soc* **2013**, *135*, 12660–12669.

(7) Zhuang, Y. X.; Hansen, O.; Knieling, T.; Wang, C.; Rombach, P.; Lang, W.; Benecke, W.; Kehlenbeck, M.; Koblitz, Jö. Vapor-Phase Self-Assembled Monolayers for Anti-Stiction Applications in MEMS. *Journal of Microelectromechanical Systems* **2007**, *16*, 1451–1460.

(8) Hopkins, A. J.; McFearin, C. L.; Richmond, G. L. SAMs under Water: The Impact of Ions on the Behavior of Water at Soft Hydrophobic Surfaces. *The Journal of Physical Chemistry C* **2011**, *115*, 11192–11203.

(9) Lee, D. H.; Oh, T.; Cho, K. Combined Effect of Chain Length and Phase State on Adhesion/friction Behavior of Self-Assembled Monolayers. *The Journal of Physical Chemistry B* **2005**, *109*, 11301–11306.

(10) Haensch, C.; Hoeppener, S.; Schubert, U. S. Chemical Modification of Self-Assembled Silane Based Monolayers by Surface Reactions. *Chemical Society Reviews* **2010**, *39*, 2323.

(11) Brzoska, J. B.; Azouz, I. B.; Rondelez, F. Silanization of Solid Substrates: A Step Toward Reproducibility. *Langmuir* **1994**, *10*, 4367–4373.

(12) Offord, D. A.; Griffin, J. H. Kinetic Control in the Formation of Self-Assembled Mixed Monolayers on Planar Silica Substrates. *Langmuir* **1993**, *9*, 3015–3025.

(13) Pizzolatto, R. L.; Yang, Y. J.; Wolf, L. K.; Messmer, M. C. Conformational Aspects of Model Chromatographic Surfaces Studied by Sum-Frequency Generation (vol 397, Pg 81, 1999). *Analytica chimica acta* **2000**, *406*, 333–334.

(14) Onclin, S.; Ravoo, B. J.; Reinhoudt, D. N. Engineering Silicon Oxide Surfaces Using Self-Assembled Monolayers. *Angewandte Chemie (International ed. in English)* **2005**, *44*, 6282–6304.

(15) Padermshoke, A.; Konishi, S.; Ara, M.; Tada, H.; Ishibashi, T.-A. Novel SiO₂-Deposited CaF₂ Substrate for Vibrational Sum-Frequency Generation (SFG) Measurements of Chemisorbed Monolayers in an Aqueous Environment. *Applied Spectroscopy* **2012**, *66*, 711–718.

(16) Snyder, R. G.; Hsu, S. L.; Krimm, S. Vibrational Spectra in the C H Stretching Region and the Structure of the Polymethylene Chain. *Spectrochimica Acta Part A: Molecular Spectroscopy* **1978**, *34*, 395–406.

(17) MacPhail, R. A.; Strauss, H. L.; Snyder, R. G.; Elliger, C. A. Carbon-Hydrogen Stretching Modes and the Structure of N-Alkyl Chains. 2. Long, All-Trans Chains. *J. Phys. Chem* **1984**, *88*, 334–341.

(18) Snyder, R. G.; Strauss, H. L.; Elliger, C. A. Carbon-Hydrogen Stretching Modes and the Structure of N-Alkyl Chains. 1. Long, Disordered Chains. **1982**, *86*, 5145–5150.

(19) Osman, M. A.; Ernst, M.; Meier, B. H.; Suter, U. W. Structure and Molecular Dynamics of Alkane Monolayers Self-Assembled on Mica Platelets. *The Journal of Physical Chemistry B* **2002**, *106*, 653–662.

(20) Allara, D. L.; Parikh, A. N.; Judge, E. The Existence of Structure Progressions and Wetting Transitions in Intermediately Disordered Monolayer Alkyl Chain Assemblies. *The Journal of Chemical Physics* **1994**, *100*, 1761–1764.

(21) Buontempo, J. T.; Rice, S. A.; Karaborni, S.; Siepmann, J. I. Differences in the Structures of Relaxed and Unrelaxed Langmuir Monolayers of Heneicosanol: Dependence of Collective Molecular Tilt on Chain Conformation. *Langmuir* **1993**, *9*, 1604–1607.

(22) Parikh, A. N.; Allara, D. L.; Azouz, I. B.; Rondelez, F. An Intrinsic Relationship between Molecular Structure in Self-Assembled N-Alkylsiloxane Monolayers and Deposition Temperature. *J. Phys. Chem* **1994**, *98*, 7577–7590.

(23) Nihonyanagi, S.; Eftekhari-Bafrooei, A.; Borguet, E. Ultrafast Vibrational Dynamics and Spectroscopy of a Siloxane Self-Assembled Monolayer. *The Journal of Chemical Physics* **2011**, *134*, 084701.

(24) Liu, J.; Conboy, J. C. Structure of a Gel Phase Lipid Bilayer Prepared by the Langmuir-Blodgett/Langmuir-Schaefer Method Characterized by Sum-Frequency Vibrational Spectroscopy. *Langmuir* **2005**, *21*, 9091–9097.

(25) Tyrode, E.; Hedberg, J. A Comparative Study of the CD and CH Stretching Spectral Regions of Typical Surfactants Systems Using VSFS: Orientation Analysis of the Terminal CH 3and CD 3Groups. *The Journal of Physical Chemistry C* **2012**, *116*, 1080–1091.

(26) Lü, R.; Gan, W.; Wu, B.; Zhang, Z.; Guo, Y.; Wang, H. C−H Stretching Vibrations of Methyl, Methylene and Methine Groups at the Vapor/Alcohol (N= 1−8) Interfaces. *The Journal of Physical Chemistry B* **2005**, *109*, 14118–14129.

(27) Chow, B. C.; Ehler, T. T.; Furtak, T. E. High-Resolution Sum-Frequency Generation from Alkylsiloxane Monolayers. *Applied Physics B: Lasers and Optics* **2002**, *74*, 395–399.

(28) Wang, H. F.; Gan, W.; Lu, R.; Rao, Y.; Wu, B. H. Quantitative Spectral and Orientational Analysis in Surface Sum Frequency Generation Vibrational Spectroscopy (SFG-VS). *International Reviews In Physical Chemistry* **2005**, *24*, 191–256.

(29) Tyrode, E.; Liljeblad, J. F. D. Water Structure Next to Ordered and Disordered Hydrophobic Silane Monolayers: A Vibrational Sum Frequency Spectroscopy Study. *The Journal of Physical Chemistry C* **2013**, *117*, 1780–1790.

(30) Wolf, L. K.; Yang, Y. J.; Pizzolatto, R. L.; Messmer, M. C. Microscopic Structure of Chromatographic Interfaces as Studied by Sum-Frequency Generation Spectroscopy. **2001**, *781*, 293–305.

(31) Liu, Y.; Wolf, L. K.; Messmer, M. C. A Study of Alkyl Chain Conformational Changes in Self-Assembled N-Octadecyltrichlorosilane Monolayers on Fused Silica Surfaces. *Langmuir* **2001**, *17*, 4329–4335.

(32) Du, Q.; Superfine, R.; Freysz, E.; Shen, Y. R. Vibrational Spectroscopy of Water at the Vapor/water Interface. *Physical Review Letters* **1993**, *70*, 2313–2316.

(33) Allen, H. C.; Casillas-Ituarte, N. N.; Sierra-Hernández, M. R.; Chen, X.; Tang, C. Y. Shedding Light on Water Structure at Air–aqueous Interfaces: Ions, Lipids , and Hydration. *Physical Chemistry Chemical Physics* **2009**, *11*, 5538–5549.

(34) Ye, S.; Nihonyanagi, S.; Uosaki, K. Sum Frequency Generation (SFG) Study of the pH-Dependent Water Structure on a Fused Quartz Surface Modified by an Octadecyltrichlorosilane (OTS) Monolayer. *Phys. Chem. Chem. Phys.* **2001**, *3*, 3463–3469.

(35) McFearin, C. L.; Richmond, G. L. The Unique Molecular Behavior of Water at the Chloroform-Water Interface. *Applied Spectroscopy* **2010**, *64*, 986–994.

(36) Wasserman, S. R.; Tao, Y. T.; Whitesides, G. M. Structure and Reactivity of Alkylsiloxane Monolayers Formed by Reaction of Alkyltrichlorosilanes on Silicon Substrates. *Langmuir* **1989**, *5*, 1074–1087.

(37) Wasserman, S. R.; Whitesides, G. M.; Tidswell, I. M.; Ocko, B. M.; Pershan, P. S.; Axe, J. D. The Structure of Self-Assembled Monolayers of Alkylsiloxanes on Silicon: A Comparison of Results from Ellipsometry and Low-Angle X-Ray Reflectivity. *Journal of the American Chemical Society* **1989**, *111*, 5852–5861.

(38) Glaser, A.; Foisner, J.; Hoffman, H.; Friedbacher, G. Investigation of the Role of the Interplay between Water and Temperature on the Growth of Alkylsiloxane Submonolayers on Silicon. *Langmuir* **2004**, *20*, 5599–5604.

(39) Folkers, J.; Laibinis, P. Self-Assembled Monolayers of Alkanethiols on Gold: Comparisons of Monolayers Containing Mixtures of Short-and Long-Chain Constituents with Methyl and Hydroxymethyl Terminal Groups. *Langmuir* **1992**, *8*, 1330–1341.

(40) Laibinis, P. E.; Nuzzo, R. G.; Whitesides, G. M. Structure of Monolayers Formed by Coadsorption of Two N-Alkanethiols of Different Chain Lengths on Gold and Its Relation to Wetting. *J. Phys. Chem* **1992**, *96*, 5097–5105.

(41) Offord, D. A.; John, C. M.; Griffin, J. H. Contact Angle Goniometry, Ellipsometry, XPS, and TOF-SIMS Analysis of Gold-Supported, Mixed Self-Assembled Monolayers Formed from Mixed Dialkyl Disulfides. *Langmuir* **1994**, *10*, 761–766.

(42) Tripp, C. P.; Hair, M. L. An Infrared Study of the Reaction of Octadecyltrichlorosilane with Silica. *Langmuir* **1992**, *8*, 1120–1126.

(43) Allara, D. L.; Parikh, A. N.; Rondelez, F. Evidence for a Unique Chain Organization in Long Chain Silane Monolayers Deposited on Two Widely Different Solid Substrates. *Langmuir* **1995**, *11*, 2357–2360.

(44) Balgar, T.; Bautista, R.; Hartmann, N.; Hasselbrink, E. An AFM Study of the Growth Kinetics of the Self-Assembled Octadecylsiloxane Monolayer on Oxidized Silicon. *Surface Science* **2003**, *532-535*, 963–969.

(45) Brzoska, J. B.; Shahidzadeh, N.; Rondelez, F. Evidence of a Transition Temperature for the Optimum Deposition of Grafted Monolayer Coatings. *Nature* **1992**, *360*, 719–721.

(46) Carraro, C.; Yauw, O. W.; Sung, M. M.; Maboudian, R. Observation of Three Growth Mechanisms in Self-Assembled Monolayers. *The Journal of Physical Chemistry B* **1998**, *102*, 4441–4445.

(47) Sakai, H.; Umemura, J. Infrared External Reflection Spectra of Langmuir Films of Stearic Acid and Cadmium Stearate. *Chemistry Letters* **1993**, 2167–2170.

(48) Sakai, H.; Umemura, J. Molecular-Orientation Change in Langmuir Films of Stearic Acid and Cadmium Stearate upon Surface Compression, as Studied by Infrared External-Reflection Spectroscopy. *Bulletin of the Chemical Society of Japan* **1997**, *70*, 1027–1032.

(49) Sefler, G. A.; Du, Q.; Miranda, P. B.; Shen, Y. R. Surface Crystallization of Liquid N-Alkanes and Alcohol Monolayers Studied by Surface Vibrational Spectroscopy. *Chemical physics letters* **1995**, *235*, 347–354.

(50) Maroncelli, M.; Strauss, H. L.; Snyder, R. G. Structure of the N-Alkane Binary Solid N-C19H40/n-C21H44 by Infrared Spectroscopy and Calorimetry. *J. Phys. Chem* **1985**, *89*, 5260–5267.

(51) Kim, Y.; Strauss, H. L.; Snyder, R. G. Conformational Disorder in the Binary Mixture Pentacontane/hexatetracontane: A Vibrational Spectroscopic Study. *J. Phys. Chem* **1989**, *93*, 485–490.

(52) Rakshit, A. K.; Zografi, G. Monolayer Properties of Fatty Acids. *Journal of Colloid and Interface Science* **1981**, *80*, 474–481.

(53) Kajiyama, T.; Ge, S.; Kojio, K.; Takahara, A. Scanning Force Microscopic Study of Surface Structure and Properties of (alkylsilane/ Fluoroalkylsilane) Mixed Monolayers. *Supramolecular Science* **1996**, *3*, 123–130.

(54) Dynarowicz-Łątka, P.; Dhanabalan, A.; Oliveira, O. N., Jr. Modern Physicochemical Research on Langmuir Monolayers. *Advances in Colloid and Interface Science* **2001**, *91*, 221–293.

(55) Chattoraj, D. K.; Birdi, K. S. Adsorption and the Gibbs Surface Excess. **1984**, 179–232.

(56) Stole, S. M.; Porter, M. D. In Situ Infrared External Reflection Spectroscopy as a Probe of the Interactions at the Liquid-Solid Interface of Long-Chain Alkanethiol Monolayers at Gold. *Langmuir* **2012**, *6*, 1199–1202.

(57) Thompson, W. R.; Pemberton, J. E. Raman Spectroscopy of Covalently Bonded Alkylsilane Layers on Thin Silica Films Immobilized on Silver Substrates. *Analytical Chemistry* **1994**, *66*, 3362–3370.

(58) Howell, C.; Maul, R.; Wenzel, W.; Koelsch, P. Interactions of Hydrophobic and Hydrophilic Self-Assembled Monolayers with Water as Probed by Sum-Frequency-Generation Spectroscopy. *Chemical physics letters* **2010**, *494*, 193–197.

(59) Rangwalla, H.; Schwab, A. D.; Yurdumakan, B.; Yablon, D. G.; Yeganeh, M. S.; Dhinojwala, A. Molecular Structure of an Alkyl-Side-Chain Polymer-Water Interface: Origins of Contact Angle Hysteresis. *Langmuir* **2004**, *20*, 8625–8633.

(60) Henry, M. C.; Wolf, L. K.; Messmer, M. C. In Situ Examination of the Structure of Model Reversed-Phase Chromatographic Interfaces by Sum-Frequency Generation Spectroscopy. *The Journal of Physical Chemistry B* **2003**, *107*, 2765–2770.

(61) Ong, T. H.; Davies, P. B.; Bain, C. D. Sum-Frequency Spectroscopy of Monolayers of Alkoxy-Terminated Alkanethiols in Contact with Liquids. *Langmuir* **1993**, *9*, 1836–1845.

(62) Tian, C. S.; Shen, Y. R. Isotopic Dilution Study of the Water/vapor Interface by Phase-Sensitive Sum-Frequency Vibrational Spectroscopy. *Journal of the American Chemical Society* **2009**, *131*, 2790–2791.

(63) Sovago, M.; Campen, R. K.; Bakker, H. J.; Bonn, M. Hydrogen Bonding Strength of Interfacial Water Determined with Surface Sum-Frequency Generation. *Chemical physics letters* **2009**, *470*, 7–12.

4. Hydrophilic monolayers

4.1. Introduction

Water-surface interactions range widely in strength from weak dipole-dipole interactions at hydrophobic surfaces,[1,2] such as the monolayers discussed in the previous chapter, to strong hydrogen bonding with a material such as tin oxide, where the water adlayer is more strongly associated with the mineral surface than other water molecules.[3] Hydrophilic surfaces like alcohols occupy a middle ground where surface-water and water-water hydrogen-bonding are of similar strengths,[4] and water is neither decoupled from the surface due to absent or weak interactions,[5,6] nor decoupled from a strongly surface-bound water adlayer.[3,7,8] Development of a hydrophilic monolayer compatible with a silica-coated CaF_2 substrate would increase the range of water-surface interactions that could be observed at the buried interface by SFG spectroscopy. Hydrophobic and hydrophilic monomers could be mixed to create surfaces varying in both polarity and texture. For example, a monolayer composed of OH terminated chains interspersed with shorter methyl-terminated chains would create hydrophobic pockets in imitation of nonpolar pores in a protein.[9]

The reactivity of trichlorisilanes towards many hydrophilic moieties necessitates an indirect approach to introducing functional groups such as OH and carboxylic acid which are not compatible with the binding group.[10–13] Carboxylic acid and OH-terminated siloxane monolayers have previously been prepared by post-monolayer deposition hydrolysis[14–17] and oxidation.[18,19] However, solution-based modifications like these are generally inhibited at interfaces compared to bulk reactions and can be difficult to bring to completion without damaging the monolayer.[20–

[23] A dry technique like thermal deprotection is attractive because it avoids solvent and steric issues of solution-based methods,[23] without the need for a bulky photo-labile group which may reduce monolayer density. Conditions of thermal decomposition - temperature, pressure, and gas type - are also easily controlled. However, no studies have been published which use this strategy to prepare simple hydrophilic monolayers.

In this project, I attempted to functionalize SiO_2-coated CaF_2 substrates with OH and COOH terminated monolayers by applying *tert*-butoxy carbonyl (Boc) and t-butyl ester siloxane monolayers, respectively, and removing the protecting groups with heat (Figure 4.1). The monolayers were first applied to fumed silica, a material with a large surface area, which allowed the monolayers to be characterized using bulk techniques. Monolayers on fumed silica were analyzed by thermogravimetry to determine the temperature at which the heat labile groups are removed without disturbing the alkane spacer. IR spectroscopy confirmed that the intended functional groups were retained or removed, but water contact angles did not decrease after treatment, and moreover SFG spectra indicated that the correct surface functionality was not obtained. Premature acid-catalyzed cleavage of the Boc and t-butyl groups during deposition may have led to the formation of multilayer films instead of monolayers. As the heat deprotection scheme looks promising, replacement of the trichlorosilane binding group with less reactive trimethoxysilane might allow the preparation to be successful.

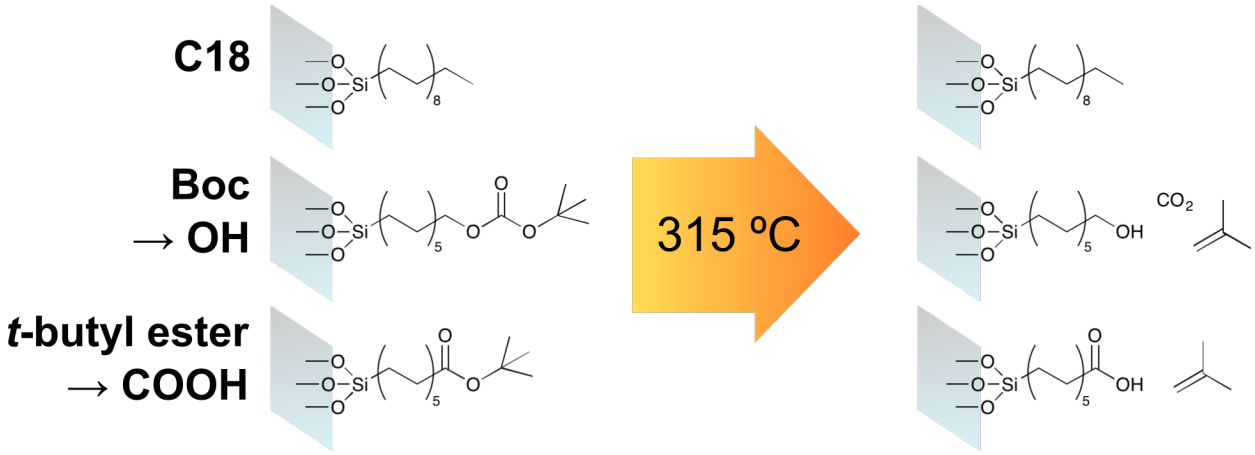

Figure 4.1 Scheme for creation of hydrophilic monolayers by post-deposition removal of heat-labile protecting groups

4.2. Methods

4.2.1. Synthesis

4.2.1.1. Boc-protected trichlorosilane

***tert*-butyl undec-10-enyl carbonate:** 10-Undecen-1-ol (Aldrich, 98%, 12 mL), di-*tert*-butyl dicarbonate (Alfa Aesar, 97%, 10 g), and Zn(OAc)•2H_2O (Sigma Aldrich, 89%, 1.3 g) were dissolved in dichloromethane and refluxed at 50 ºC overnight.[24] The resulting solution was washed with brine, and the Boc alkene was extracted into dichloromethane (DCM), dried over $MgSO_4$, and distilled to remove DCM. Flash chromatography removed excess undecenol (95% hexanes, 5% EtOAc). ^{1}H NMR (400 MHz, $CDCl_3$): 5.8 (1H, ddt), 5.0 (1H, m), 4.9 (1H, t), 4.1 (2H, t), 2.1 (2H, q) 1.7 (2H, quin), 1.5 (9H, s), 1.4-1.2 (12H, m).

***tert*-butyl (11-trichlorosilyl)undecyl) carbonate:** On a vacuum line, platinum on activated carbon (Sigma Aldrich, 1% Pt, 0.10 g), 2.95 g alkene product, and $HSiCl_3$ (Sigma Aldrich, 99%, 3 mL) were degassed and stirred under Ar for 2 days at room temperature. Excess $HSiCl_3$ (bp 32 ºC) was boiled off, and Pt was filtered out with Celite. The structure of the t-butyl trichlorosilane

was verified by ^{1}H NMR (300 MHz, $CDCl_3$): 4.1 (2H, t), 1.7-1.5 (2H, m), 1.5 (9H, s), 1.4-1.2 (18H, m)) and FTIR (Figure 4.3).

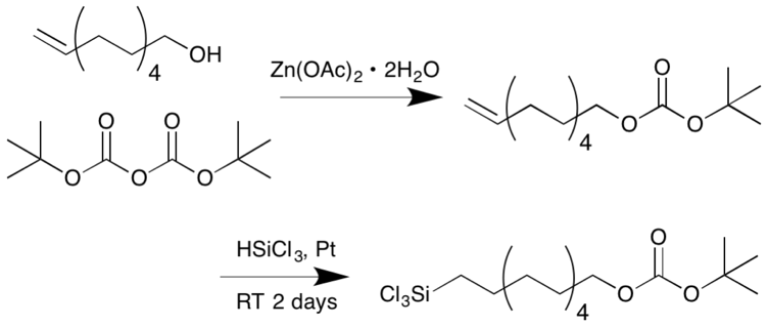

Figure 4.2 Boc-protected trichlorosilane synthesis scheme

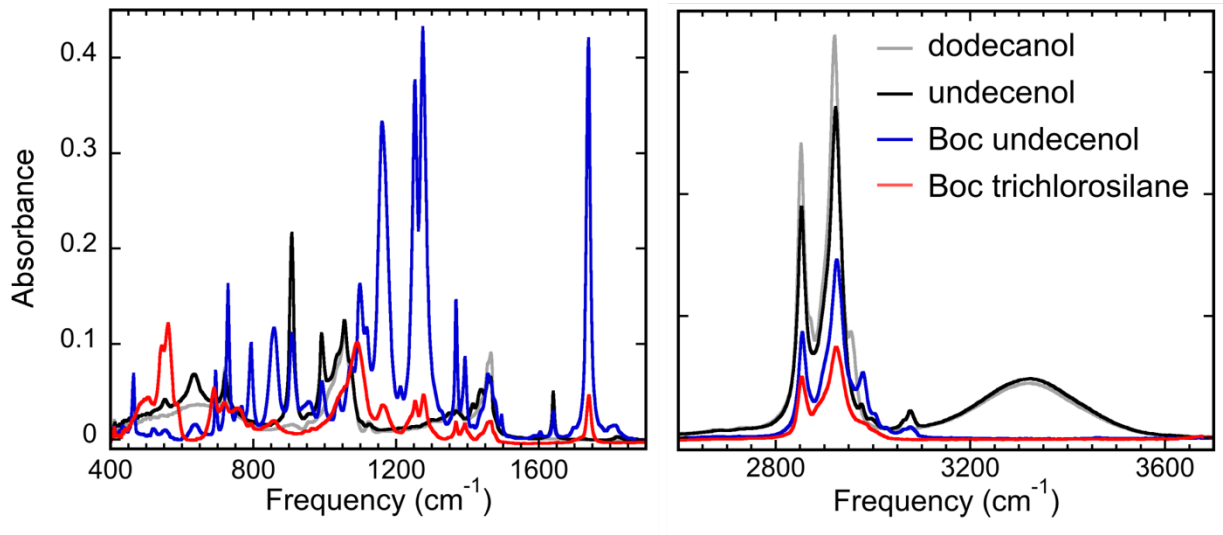

Figure 4.3 IR spectra of compounds in synthesis of Boc protected tricholosilane, with dodecanol for reference

4.2.1.2. t-butyl ester protected trichlorosilane

***tert*-butyl undec-10-enoate:** 10-Undecenoic acid (Sigma Aldrich, 98%, 20 g) was refluxed with thionyl chloride (Sigma Aldrich, 99%, 30 mL) under N_2 flow for 1.5 hours at 75 ºC, then overnight at room temperature. The acid chloride (red-brown liquid) was dissolved in toluene and distilled to remove $SOCl_2$. Product was added dropwise to chilled *tert*-butanol (Fisher Scientific, 50 mL), and stirred for 4 hours under Ar. Excess acid chloride was quenched over ice

and deprotonated by addition of saturated Na_2CO_3. The ester was extracted with three washes of dichloromethane and dried with $MgSO_4$ and further purified by silica column with DCM. Product is orange-brown liquid. ^{1}H NMR (300 MHz, $CDCl_3$): 5.80 (1H, ddt), 4.99 (1H, t), 4.92 (1H, m), 2.18 (2H, t), 2.05 (2H, q), 1.56 (2H, t), 1.43 (9H, s), 1.4-1.2 (10H, m)

***tert*-butyl 11-(trichlorosilyl)undecanoate:** t-butyl ester protected alkene (2 g) was added to dry Pt on C (Sigma Aldrich, 1% Pt by weight) and flushed with N_2. Trichlorosilane (Sigma Aldrich, 99%, 1.5 mL) was added under positive N_2 flow. Solution was degassed and then stirred at room temperature for one day under N_2. $HSiCl_3$ was driven off by water bath, and product was filtered over Celite to remove catalyst. Verified structure of alkene and trichlorosilane by ^{1}H NMR (300 MHz, $CDCl_3$): 2.20 (2H, t), 1.57 (4H, m), 1.44 (9, s), 1.43-1.22 (12, m) and FTIR (Figure 4.5). The t-butyl ester trichlorosilane was hydrolyzed by sonication in water prior to IR spectroscopy.

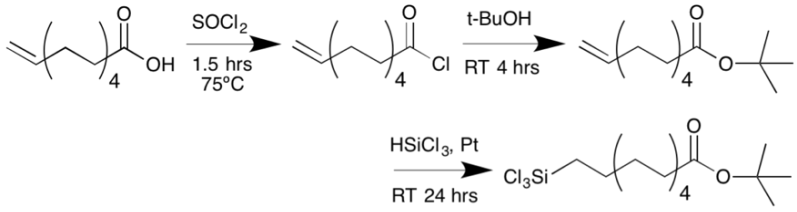

Figure 4.4 t-Butyl ester synthesis scheme

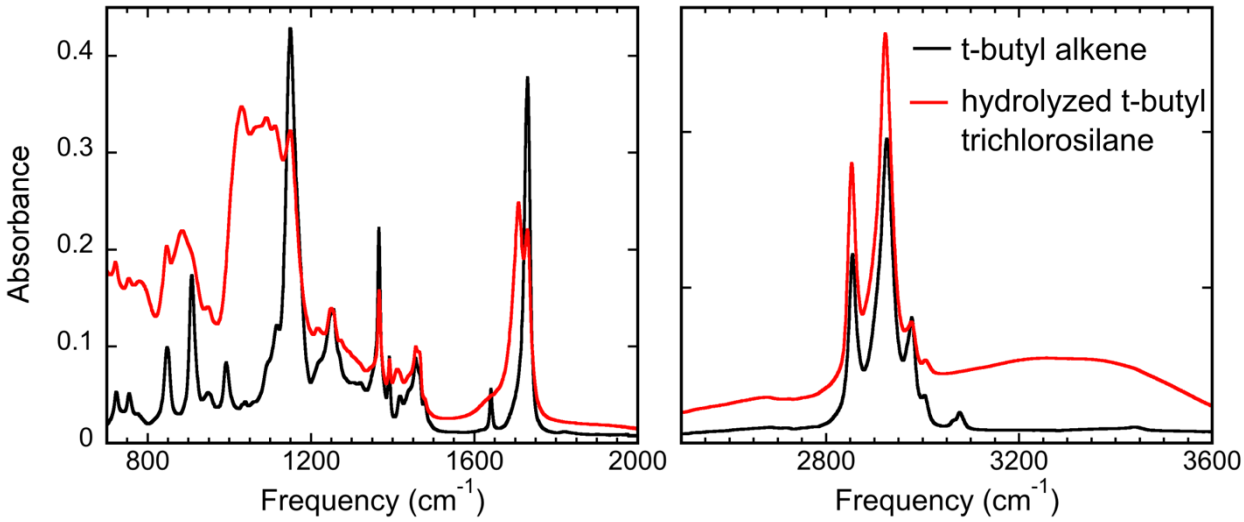

Figure 4.5 IR spectra of compounds in synthesis of t-butyl ester trichlorosilane

4.2.2. Monolayer application

4.2.2.3. Monolayers on fumed silica

The preparation of monolayers on fumed silica detailed here largely follows procedures established for bulk Raman[25] and solid-state NMR studies.[26,27] Fumed silica (Sigma, 0.2-0.3 μm particle size, 200 m^2/g, 0.2 g or 1 equivalent) was placed in a flask and evacuated and flushed with N_2. Toluene (Macron, ACS grade, 20 mL), dried over molecular sieves, was added to the fumed silica to suspend the particles. Five equivalents of trichlorosilane monomer (octadecyltrichlorosilane (C18), Boc trichlorosilane, or t-butyl ester trichlorosilane) was added to the suspension and stirred under N_2 at room temperature for 12 hours. The trichlorosilane was quenched with triethylamine (Sigma Aldrich, 99%, 10 equivalents) and stirred for 30 minutes. Unbound monomer was then rinsed from the fumed silica. The fumed silica suspension was removed from the flask by syringe and centrifuged, and the supernatant was decanted. Fresh dry toluene was added back to the fumed silica, the fumed silica was re-dispersed in solution, centrifuged, and decanted again. The rinsing procedure was repeated at least four times. Trimethylamine was removed by three rinses of hexanes (Fisher Scientific, HPLC grade) in the

same way. Coated fumed silica was characterized by FTIR with a diamond attenuated total reflectance (ATR) accessory.

Figure 4.6 Fumed silica

4.2.2.4. Monolayers on flat silica substrates

C18, C12, t-butyl ester, and Boc monolayers were applied to flat silica substrates (microscope slides and silica-coated CaF_2) by adsorption from solution. Glass substrates and glassware were cleaned in a solution prepared by dissolving Nochromix powder (Godax Laboratories) in concentrated sulfuric acid (Fisher Scientific, certified ACS plus). Silica-coated CaF_2 windows were baked in a vacuum furnace to 750 ºC to remove surface impurities. All substrates and implements were rinsed in ultra pure water (18.2 MΩ·cm @25 °C, 5 ppm total organic content) and dried. Substrates were soaked, covered, in deposition solutions of 2 mM trichlorosilane monomer in hexanes (Fisher Scientific, HPLC grade) for 90 minutes. Unbound monomer was removed by sonication in hexanes and ultra pure water. Monolayers were characterized by FTIR: ATR for glass substrates, and 8x transmission with White cell (Chapter 1.3) for monolayers on silica-coated CaF_2. A contact angle goniometer (described in Chapter 1.2) was used to measure water contact angle.

4.2.3. Deprotection

4.2.3.5. Heat

Monolayers on fumed silica were characterized by thermogravimetric analysis (TGA) under N_2 to determine the temperatures at which they decomposed. Samples were equilibrated at 100 ºC and heated to 700 ºC at a rate of 3-10 ºC/min while the weight of the sample was monitored. To remove the heat-labile protecting groups of the Boc and t-butyl ester monolayers on fumed silica and flat substrates, monolayers were heated to 315 ºC in a vacuum or N_2 furnace for at least an hour with a temperature ramp of 3 ºC/min. Fumed silica samples were characterized by FTIR (ATR) before and after heat treatment; samples on flat substrates were additionally characterized by water contact angle.

4.2.3.6. Solution

Deprotection of Boc monolayers on glass slides was also attempted in solution and monitored by FTIR and contact angle. Monolayer removal was tracked by the amplitude of the asymmetric CH_2 stretch (d-). A reduction in contact angle but not IR intensity meant successful deprotection, while a reduction in both meant that the monolayer was being removed. Reagents were used as received: hydrochloric acid (BDH, ACS grade, 38%), trifluoroacetic acid (TFA, Sigma-Aldrich, 99%), trimethylsilyl iodide (Sigma-Aldrich, 97%), chloroform (Macron, ACS grade), potassium hydroxide (Mallinckrodt, ACS), acetic anhydride (Sigma-Aldrich, 98%), iron (III) chloride (Sigma-Aldrich, 97%), diethyl ether (Fisher Scientific), triethylamine (Sigma-Aldrich, 99%), lithium bromide (Aldrich, 99%), and acetonitrile (Mallinckrodt, ACS). Details given in Table 4.1, with room temperature abbreviated as rt.

Table 4.1 Boc deprotection methods and results. The average contact angle before any treatment was 85º. The triethylamine/LiBr solution removed the monolayer, so final IR and contact angle measurements were not collected.

Solution	Conditions	Time (h)	d- Amplitude $x10^{-4}$		Contact angle (º) final
			Initial	Final	
2.4 M HCl	rt	70	5.7	4.6	58
2.4 M HCl	reflux 85 ºC	11	4.6	6.5	25
neat TFA	rt, then reflux 60 ºC	0.8 1	4.2	4.0	87
0.1 M Me_3SiI in $CHCl_3$	under N_2: rt 0.5 hr, then 60 ºC	3	7.4	8.8	81
1 M aq KOH	rt	1	8.5	3.1	43
Ac_2O $FeCl_3$ in Et_2O	2 mL Ac_2O+0.1 g $FeCl_3$ in 20 mL Et_2O, rt	4	8.1	8.8	77
Et_3N LiBr in CH_3CN	3.2 mL Et_3N+2 g LiBr in CH_3CN+H_2O, reflux 70 ºC	1	16	---	---

4.1. Results

The complete ineffectiveness of trifluoroacetic acid (TFA) in removing the Boc group from Boc-protected monolayers was unexpected, as a 50% solution of TFA in dichloromethane is a standard means of removing a Boc group.[28–30] A previous attempt with the 50% solution failed, as did neat TFA at room temperature and at 60 ºC described above. Only the 85 ºC HCl solution

significantly reduced the monolayer contact angle without removing the monolayer. In Figure 4.7, the CH_2 symmetric stretch (d-) intensity and water contact angle are shown for the KOH and hot HCl treatments. An OH or COOH-terminated monolayer should have a water contact angle less than 10º.[31] The drop in d- strength for KOH means that the monolayer was being destroyed, and so the drop in contact angle is likely due to exposure of the hydrophilic silica substrate. After 5 hours of treatment with 85 ºC 2.4 M HCl, the intensity of the symmetric CH_2 mode leveled off while the contact angle was still dropping. The harsh conditions and long reaction time required for the Boc removal demonstrate how inefficient wet chemistry methods are for this post-deposition monolayer modification. In addition, HCl etches CaF_2 and thus is incompatible with the IR and visible transparent substrates used to probe the buried water interface with SFG spectroscopy.

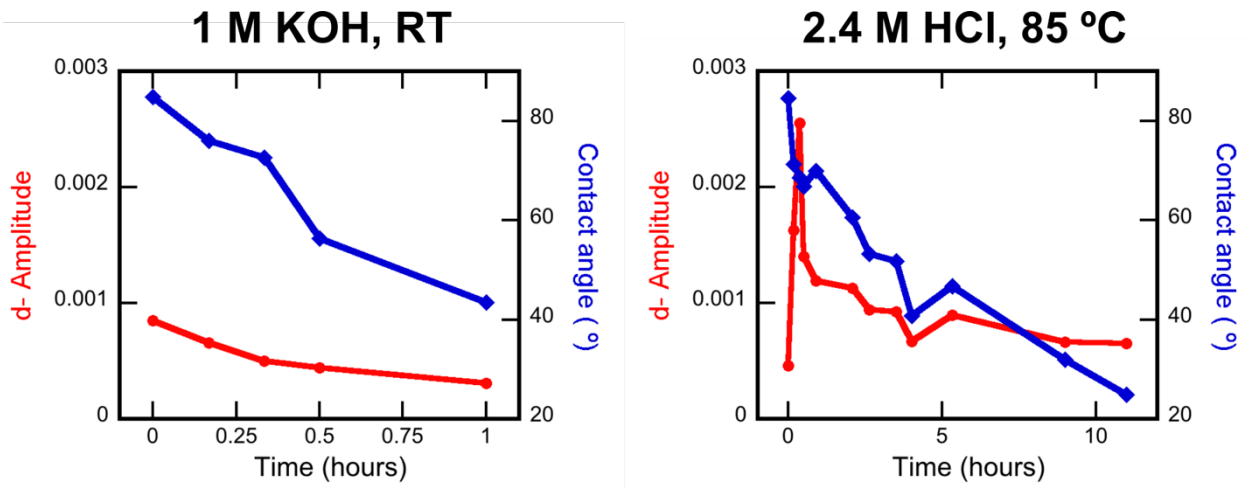

Figure 4.7 CH_2 asymmetric (d-) intensity and water contact angle for Boc monolayers placed in 1 M KOH and 85 ºC 2.4 M HCl solutions for Boc removal.

Heat deprotection was more successful. The loss of Boc and t-butyl protecting groups was found by TGA to occur at least 200 ºC below decomposition of the alkane spacer, making selective removal feasible. In Figure 4.8, the change in sample mass with temperature is shown for bare fumed silica and C18, Boc, and t-butyl ester monolayers. The bare fumed silica does not lose

mass with heating as there is no organic content to decompose, but fumed silica covered with a C18 monolayer shows a small peak at ~150 ºC, from adsorbed water,32 and a large peak at 500 ºC, where the alkane chain is removed.33 The 500 ºC peak is shared by all monolayers as they all have an alkane chain. Additional peaks appear at lower temperatures for the Boc and t-butyl ester monolayers where the heat labile groups decompose. Boc and t-butyl come off at temperatures similar to those reported for the protecting groups in range of photo-cross-linkable polymers.34–36 However, the ratio of mass lost in the first (heat labile) and second (alkane) decomposition peaks is lower than expected for the Boc monolayer. The ratio should be 0.65 for Boc, but is only 0.24 (Table 4.2).

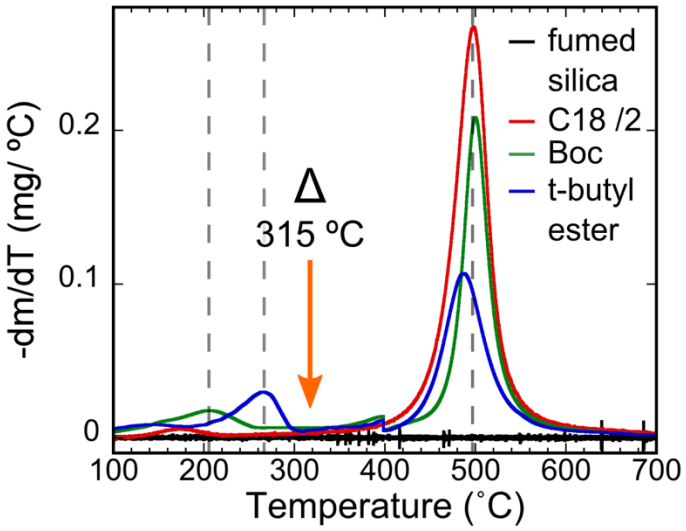

Figure 4.8 Thermogravimetric analysis (TGA) of monolayers on fumed silica. Peaks represent temperatures at which material decomposes.

Table 4.2 Decomposition of monolayers on fumed silica. Fractional coverage is calculated assuming 200 m^2/g surface area of fumed silica, 25 $Å^2$ area per monomer.

Monolayer	Decomposition (º C)	Expected mass (peak) ratio ($1^{st}/2^{nd}$)	Measured mass (peak) ratio	Fractional coverage
C18	498	0	---	0.37
Boc	205, 502	0.65	0.24	0.48
t-butyl ester	267, 488	0.33	0.28	0.35

FTIR spectra of monolayers on fumed silica are consistent with the loss of Boc and t-butyl and the retention of the alkane spacer after heating the monolayers to 315 ºC (Figure 4.9). The regions below 1350 cm^{-1} and above 3100 cm^{-1} are not shown due to strong absorption by fumed silica. No mass change is observed for fumed silica and C18 (aside from water) below 315 ºC, and similarly, the FTIR spectra of these samples show no change after heating. A change in the FTIR spectra is observed with Boc and t-butyl ester monolayers, confirming that the mass loss below 315 ºC (Figure 4.8) causes a change in chemical structure. For the Boc monolayer, the asymmetric CH_3 stretch (2980 cm^{-1}) from the t-butyl group and the C=O stretch (1750 cm^{-1}) from the carbonyl are removed, while the CH_2 stretching (2800-2940 cm^{-1}) and bending (1400-1450 cm^{-1}) modes from the alkane chain remain. The t-butyl ester loses the CH_3 but not the C=O stretch, suggesting that the t-butyl is gone but the carbonyl has remained.

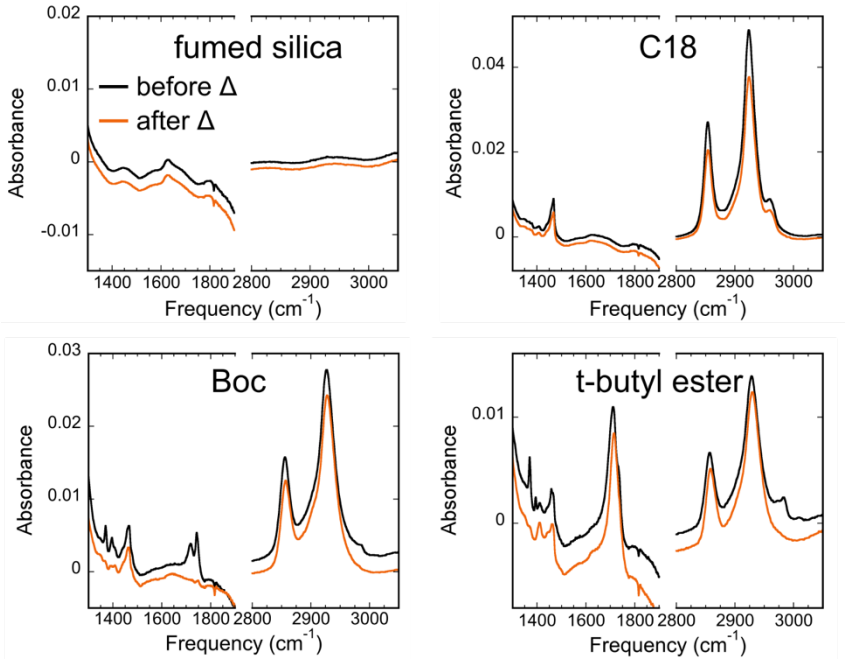

Figure 4.9 Monolayers on fumed silica before and after heating in N_2 to 315 ºC. Compare to bare fumed silica, upper left.

FTIR spectra were acquired for heat-treated C18, C12, and Boc ("OH") monolayers applied to glass and silica-coated CaF_2 substrates (Figure 4.10). For comparison, some Boc ("Boc") monolayers were not baked. Two intense CH_2 symmetric and asymmetric stretching modes, d+ and d- (2850 and 2920 cm^{-1}), are common to all samples. An asymmetric CH_3 stretch (r-) is clearly resolved above 2940 cm^{-1} for all, but the frequency is higher for the tertiary methyl groups of the Boc monolayer, at ~2980 cm^{-1}, than for the primary methyl groups of the C18 and C12 monolayers, ~2960 cm^{-1}. As in the spectrum of the Boc monolayer on fumed silica, the carbonyl C=O stretch of Boc appears ~1720 cm^{-1}. While these monolayers were heated to 315 ºC like the monolayers on fumed silica, the effect is less consistent here. Shown below (Figure 4.10) are IR spectra of two heat-treated Boc "OH" monolayers, OH 1 and OH 2, representative of the range in structure observed. The t-butyl and ester functional groups are almost entirely gone for OH 2, but are only half removed for OH 1. Possibly the energy required to remove the Boc is

higher for a densely packed monolayer prepared on a flat surface, compared to the more sparsely covered fumed silica (Table 4.2).

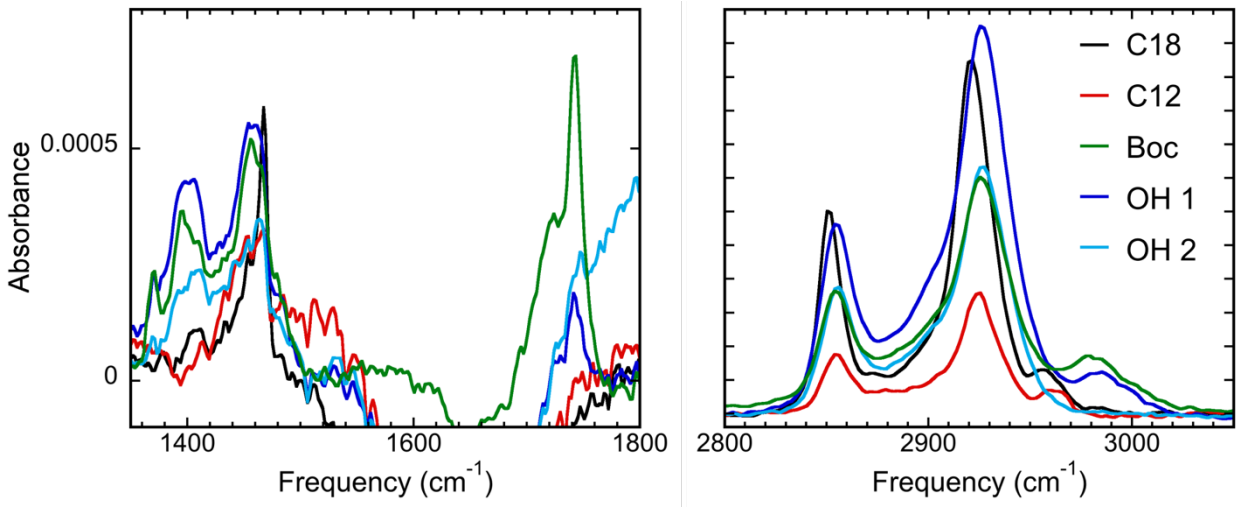

Figure 4.10 IR spectra of SiO_2 substrates modified with monolayers. Two spectra of heat-treated Boc "OH" monolayers (blue) are included to show variation between OH monolayers.

Deprotection of the Boc and t-butyl ester monolayers is at least partially successful as judged by the FTIR and TGA data, but the removal of the protecting groups was not accompanied by a decrease in water contact angle (Table 4.3). An OH- or carboxylic acid-terminated surface should have a contact angle near zero, as do thiol monolayers with these functionalities.[31] Partial deprotection should still result in a decrease in contact angle, not an increase. A study of ester monolayers on silicon which were incompletely hydrolyzed to carboxylic acids showed a decrease in contact angle from ~70º to 55º.[16]

Table 4.3 Contact angles of monolayers on glass before and after heating to 315 ºC.

Monolayer	Before Δ (º)	After Δ (º)
C18	105 ± 2	102 ± 2
Boc	78 ± 2	89 ± 3
t-butyl ester	70 ± 3	79± 6

SFG spectra of the monolayers complicate the interpretation further. While methylene (d+ and d-) peaks dominate the CH stretch region in the IR spectra of these monolayers, CH_2 modes from trans alkane chains cancel in sum frequency generation. A good indicator of order for a methyl-terminated alkane monolayer like C18 and C12 is a large CH_3 stretch response, as the methyl groups will be aligned and signal will add constructively, and a small CH_2 stretch response, as signal from opposing CH_2 groups will cancel. In Figure 4.11 a, we see SFG spectra of two alkane monolayers C18 (black) and C12 (red), both of which have previously been heated to 315 ºC. The two largest features are the symmetric methyl stretch (r+, ~2860 cm^{-1}) and Fermi resonance (r+FR, ~2930 cm^{-1}) from methyl groups pointing away from the substrate. At 2880 cm^{-1} is the asymmetric methylene stretch d-. That the d- mode is large enough relative to the CH_3 modes to be well resolved (compare to C18/C12 100/0 in Figure 3.7) suggests that heating disordered the C18 and C12 monolayers somewhat.

On the same plot is shown a Boc monolayer which has not been heated ("Boc," green) and one which has been heated to 315 ºC, ("OH," blue). Again, the largest peaks are r+ and r+FR, but the d- peak is not visible. It is strange that both Boc and OH have large r modes, even though OH has been heated so the methyl groups (from t-butyl) should be removed. All OH monolayers examined had large r+ and r+FR peaks; this result is characteristic.

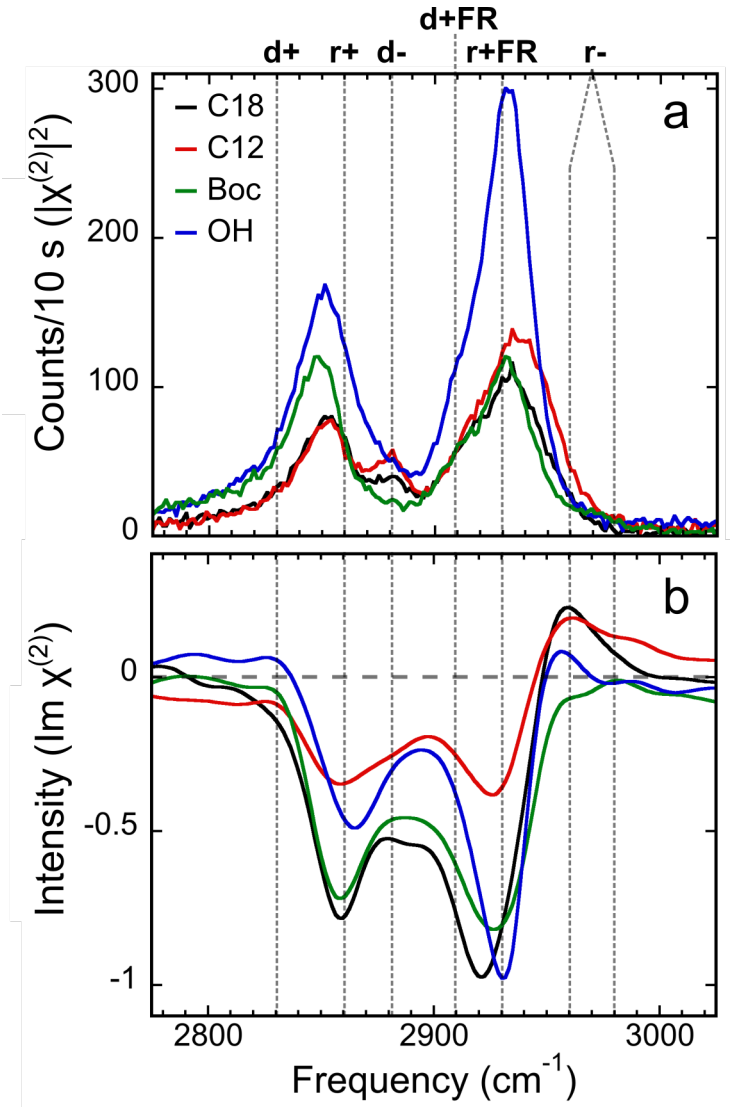

Figure 4.11 SFG of dry monolayers: C18, C12, Boc (green) and heat-treated Boc ("OH", blue), (a) standard SFG , and (b) homodyned SFG. The C18 monolayer shown in (b) was not heat-treated.

In Figure 4.11 b we see the $Im\chi^{(2)}$ spectra for the same monolayers obtained by heterodyned SFG. As noted in Chapter 1.3, the sign of the imaginary component of $\chi^{(2)}$ can be positive or negative and depends on the up/down orientation of the chromophore. Thus, heterodyned SFG spectra relate the absolute orientation of molecules at an interface. The real (blue) and imaginary (red) components for the OH monolayer are shown in Figure 4.12. When combined and squared, the standard SFG $|\chi^{(2)}|^2$ response (black) is recovered. Comparing the $Im\chi^{(2)}$ spectra in Figure 4.11 b, all monolayers have a negative r+ and r+FR peak, meaning that the methyl groups

for all the monolayers are pointing in the same direction: away from the surface. While the OH monolayer should not have the r+/r+FR modes, it at least makes sense that the methyl groups would be oriented up even for a multilayer, because the monomers should be anchored to the substrate or to preceding layers by a siloxane bond. With the additional information about peak sign, an additional mode is visible which is not obvious in the standard SFG spectra: the asymmetric CH_3 stretch r-.

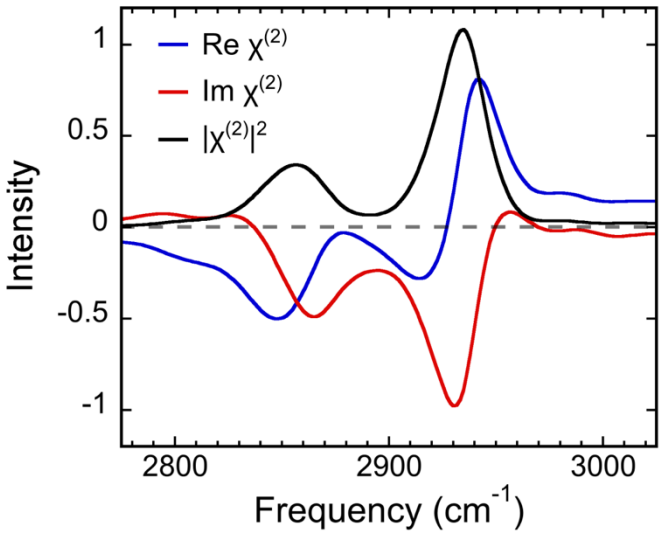

Figure 4.12 Real, imaginary and squared $\chi^{(2)}$ elements of OH monolayer acquired by heterodyned SFG.

4.2. Discussion

NMR and FTIR spectra confirm that the intended Boc and t-butyl ester terminated trichlorosilane monomers were synthesized. Upon hydrosilation of the alkene, the alkene features in the spectra are removed, while the Boc and t-butyl ester functionalities are retained. The C18, Boc, and t-butyl ester monolayers all share a decomposition event at ~500 ºC, verifying that this peak represents the decomposition of the alkane spacer which they all share. The second peak for Boc

and t-butyl ester occurs at a lower temperature and is consistent with the literature value for thermal decomposition of these groups.[35]

The mass lost at the lower temperature for Boc, however, is smaller than expected. During deposition of trichlorosilane monolayers, Si-Cl bonds are hydrolyzed by water at the silica surface, which leads to the formation of siloxane Si-O-Si bonds to the substrate.[37] This also lowers the pH of the deposition solution as H^+ and Cl^- are released, which could cause acid labile groups like t-butyl ester and Boc to be removed prematurely. This might explain why the Boc heat labile peak from TGA is smaller than predicted. In fact, the hydrosilation of the Boc alkene to produce the Boc trichlorosilane has failed multiple times from loss of the Boc group.

The Boc and t-butyl ester groups from the synthesis of trichlorosilane monomers are also observed for the monomers when bound to fumed silica and flat silica substrates. The intensity of the Boc monolayer CH_2 modes in IR spectra (Figure 4.10), arising from the 11 carbon alkene spacer, are large compared to the CH_2 modes of the C12 monolayer, which also has 11 methylene groups. This could be explained by the formation of a multilayer film. The SFG intensity of the Boc monolayer is similar to C12 and C18 (Figure 4.11), suggesting that the multilayer structure, if present, is structured and not a product of disorganized polymerization. The Boc SFG spectrum is, like C12 and C18, dominated by the r+ and r+ FR modes. It is odd that the CH_3 modes of Boc are so close in frequency to those of C12 and C18 when presumably they come from tertiary and not primary CH_3 groups (the t-butyl), but it is reasonable that methyl modes are present. Boc and t-butyl ester monolayers are hydrophobic (contact angles of 78º and 70º, respectively), consistent with a t-butyl group termination.

Boc and t-butyl ester film contact angles do not decrease, however, after they have been baked to remove the heat labile groups. Even so, IR spectra of the monolayers on fumed silica and flat silica substrates show at least partial loss of the expected functional groups. Just as before deprotection, the CH_2 modes of Boc in the IR spectra are stronger than predicted by the number of methylene groups in the monomer. Up to this point, the evidence is consistent with adsorption of a Boc multilayer. Multi-monomer strands may form in the deposition solution or at the surface of the growing film when a chlorosilane or silanol bonds with an exposed OH or COOH. The resulting film would be thicker than a monolayer and also well aligned due to interactions between the long monomers. The terminal group might still have an intact Boc or t-butyl ester group before heating, accounting for their appearance in the IR spectra and the lower temperature decomposition peak in TGA. After heating, the terminal Boc or t-butyl would be removed, no longer showing up in IR spectra. However, the SFG spectra of heat-treated Boc monolayer ("OH") are not compatible with this idea. The r+ and r+ FR peaks are not smaller but more intense for the OH film compared to Boc. This is hard to reconcile with the removal of the t-butyl r- peak in the FTIR spectra. It is unlikely that the two large peaks attributed to the methyl symmetric mode are actually CH_2 modes. For the CH_2 modes to be so prominent, the monomers of the OH film would have to kinked in order to break the symmetry of the chain axis, and also be arranged in a consistent way.

Premature deprotection of the acid-labile Boc and t-butyl ester groups is likely the cause of the failure to prepare hydrophilic OH- and COOH-terminated monolayers. This mechanism could account for the similar difficulties with both films. Switching from a trichlorosilane to a trimethoxy binding group is a good option. It has been shown here that Boc and t-butyl ester protecting groups can be efficiently removed at temperatures well separated from the

decomposition point of the alkane spacer, when deposited on silica substrates. A trimethoxysilane binding group could still anchor these groups to silica, but is less reactive, and less likely to lead to the acid-catalyzed cleavage of Boc and t-butyl ester.

4.3. Conclusions

A strategy for preparing hydrophilic silane monolayers by post-deposition removal of heat labile groups has been explored. Monolayers assembled from trichlorosilane monomers are robust and can be applied to a range of transparent substrates,[38] but choice in monolayer functionality is limited by the reactivity of trichlorosilane with many hydrophilic moieties.[12] Boc and t-butyl ester groups are compatible with trichlorosilane and can be removed by heat to reveal OH and COOH termini. Boc and t-butyl ester trichlorosilane monomers were synthesized and applied to fumed silica and flat silica substrates. Thermogravimetric analysis and FTIR spectra of the monolayers show that the protecting groups can be removed without damaging the alkane chain beneath. Contact angles did not decrease along with the removal of the protecting groups, however, and SFG spectra also indicated that the desired monolayers were not created. Boc and t-butyl ester are acid labile as well as heat labile, and their partial removal during monolayer deposition is probably responsible for this result.

References

(1) Hopkins, A. J.; McFearin, C. L.; Richmond, G. L. SAMs under Water: The Impact of Ions on the Behavior of Water at Soft Hydrophobic Surfaces. *The Journal of Physical Chemistry C* **2011**, *115*, 11192–11203.

(2) Shen, Y.-R.; Ostroverkhov, V. Sum-Frequency Vibrational Spectroscopy on Water Interfaces: Polar Orientation of Water Molecules at Interfaces. *Chemical Reviews* **2006**, *106*, 1140–1154.

(3) Wang, H.-W.; DelloStritto, M. J.; Kumar, N.; Kolesnikov, A. I.; Kent, P. R. C.; Kubicki, J. D.; Wesolowski, D. J.; Sofo, J. O. Vibrational Density of States of Strongly H-Bonded Interfacial Water: Insights from Inelastic Neutron Scattering and Theory. *Journal Of Physical Chemistry C* **2014**, *118*, 10805–10813.

(4) Novak, A. Structure and Bonding. **1974**, *18*, 177–216.

(5) Stiopkin, I. V.; Weeraman, C.; Pieniazek, P. A.; Shalhout, F. Y.; Skinner, J. L.; Benderskii, A. V. Hydrogen Bonding at the Water Surface Revealed by Isotopic Dilution Spectroscopy. *Nature* **2011**, *474*, 192–195.

(6) Tian, C. S.; Shen, Y. R. Sum-Frequency Vibrational Spectroscopic Studies of Water/vapor Interfaces. *Chemical physics letters* **2009**, *470*, 1–6.

(7) Limmer, D. T.; Willard, A. P.; Madden, P. A.; Chandler, D. Water Exchange at a Hydrated Platinum Electrode Is Rare and Collective. *The Journal of Physical Chemistry C* **2015**, *119*, 24016–24024.

(8) Rotenberg, B.; Patel, A. J.; Chandler, D. Molecular Explanation for Why Talc Surfaces Can Be Both Hydrophilic and Hydrophobic. *J. Am. Chem. Soc* **2011**, *133*, 20521–20527.

(9) Rasaiah, J. C.; Garde, S.; Hummer, G. Water in Nonpolar Confinement: From Nanotubes to Proteins and Beyond *. *Annual Review of Physical Chemistry* **2008**, *59*, 713–740.

(10) Balachander, N.; Sukenik, C. N. Functionalized Siloxy-Anchored Monolayers with Exposed Amino, Azido, Bromo, or Cyano Groups. *Tetrahedron Letters* **1988**, *29*, 5593–5594.

(11) Gooding, J. J.; Ciampi, S. The Molecular Level Modification of Surfaces: From Self-Assembled Monolayers to Complex Molecular Assemblies. *Chem. Soc. Rev.* **2011**, *40*, 2704–2718.

(12) Haensch, C.; Hoeppener, S.; Schubert, U. S. Chemical Modification of Self-Assembled Silane Based Monolayers by Surface Reactions. *Chemical Society Reviews* **2010**, *39*, 2323.

(13) Fryxell, G. E.; Rieke, P. C.; Wood, L. L.; Engelhard, M. H.; Williford, R. E.; Graff, G. L.; Campbell, A. A.; Wiacek, R. J.; Lee, L.; Halverson, A. Nucleophilic Displacements in Mixed Self-Assembled Monolayers. *Langmuir* **1996**, *12*, 5064–5075.

(14) Chen, E. H.; Saslow, S. A.; Nguyen, S. T.; Geiger, F. M. Zinc Ion–Hydroxyl Interactions at Undecanol-Functionalized Fused Silica/Water Interfaces Using the Eisenthal $\chi(3)$ Technique. *The Journal of Physical Chemistry C* **2012**, *116*, 7016–7020.

(15) Konek, C. T.; Musorrafiti, M. J.; Al-Abadleh, H. A.; Bertin, P. A.; Nguyen, S. T.; Geiger, F. M. Interfacial Acidities, Charge Densities, Potentials, and Energies of Carboxylic Acid-

Functionalized Silica/Water Interfaces Determined by Second Harmonic Generation. *Journal of the American Chemical Society* **2004**, *126*, 11754–11755.

(16) Asanuma, H.; Noguchi, H.; Uosaki, K.; Yu, H.-Z. Structure and Reactivity of Alkoxycarbonyl (Ester)-Terminated Monolayers on Silicon: Sum Frequency Generation Spectroscopy. *The Journal of Physical Chemistry B* **2006**, *110*, 4892–4899.

(17) Gershevitz, O.; Sukenik, C. N. In Situ FTIR-ATR Analysis and Titration of Carboxylic Acid-Terminated SAMs. *Journal of the American Chemical Society* **2004**, *126*, 482–483.

(18) Wasserman, S. R.; Tao, Y. T.; Whitesides, G. M. Structure and Reactivity of Alkylsiloxane Monolayers Formed by Reaction of Alkyltrichlorosilanes on Silicon Substrates. *Langmuir* **1989**, *5*, 1074–1087.

(19) Miyake, T.; Tanii, T.; Kato, K.; Hosaka, T.; Kanari, Y.; Sonobe, H.; Ohdomari, I. Nanopatterning of Hydroxy-Terminated Self-Assembled Monolayer Taking Advantage of Terminal Group Modification. *Chemical physics letters* **2006**, *426*, 361–364.

(20) Holger Schönherr; Chuanliang Feng, and; Shovsky, A. Interfacial Reactions in Confinement: Kinetics and Temperature Dependence of Reactions in Self-Assembled Monolayers Compared to Ultrathin Polymer Films. *Langmuir* **2003**, *19*, 10843–10851.

(21) Vaidya, B.; Chen, J.; Porter, M. D.; Angelici, R. J. Effects of Packing and Orientation on the Hydrolysis of Ester Monolayers on Gold. *Langmuir* **2001**, *17*, 6569–6576.

(22) Barbara Dordi; Holger Schönherr, and; Vancso, G. J. Reactivity in the Confinement of Self-Assembled Monolayers: Chain Length Effects on the Hydrolysis of N-Hydroxysuccinimide Ester Disulfides on Gold. *Langmuir* **2003**, *19*, 5780–5786.

(23) Chechik, V.; Crooks, R. M.; Stirling, C. J. M. Reactions and Reactivity in Self-Assembled Monolayers. *Advanced Materials* **2000**, *12*, 1161–1171.

(24) Bartoli, G.; Bosco, M.; Carlone, A.; Dalpozzo, R.; Locatelli, M.; Melchiorre, P.; Palazzi, P.; Sambri, L. The First Simple Method of Protection of Hydroxy Compounds as Their O-Boc Derivatives under Lewis Acid Catalysis. *Synlett* **2006**, *17*, 2104–2108.

(25) Wang, R.; Guo, J.; Baran, G.; Wunder, S. L. Characterization of the State of Order of Octadecylsilane Chains on Fumed Silica. *Langmuir* **2000**, *16*, 568–576.

(26) Linehan, J. C.; Stiff, C. M.; Fryxell, G. E. A Simple Determination of Alkylsilane Monolayer Population Density. *Inorganic Chemistry Communications* **2006**, *9*, 239–241.

(27) Gao, W.; Reven, L. Solid-State NMR Studies of Self-Assembled Monolayers. *Langmuir* **1995**, *11*, 1860–1863.

(28) Spivey, A. C.; Srikaran, R. 2 Synthetic Methods. Part (iii) Protecting Groups. *Annu. Rep. Prog. Chem., Sect. B: Org. Chem.* **2001**, *97*, 41–60.

(29) Jarowicki, K.; Kocienski, P. Protecting Groups. *Contemporary Organic Synthesis* **1995**, *2*, 315–336.

(30) Orain, D.; Ellard, J.; Bradley, M. Protecting Groups in Solid-Phase Organic Synthesis. *Journal of Combinatorial Chemistry* **2002**, *4*, 1–16.

(31) Bain, C. D.; Troughton, E. B.; Tao, Y. T.; Evall, J.; Whitesides, G. M.; Nuzzo, R. G. Formation of Monolayer Films by the Spontaneous Assembly of Organic Thiols from Solution onto Gold. *Journal of the American Chemical Society* **1989**, *111*, 321–335.

(32) Zhuravlev, L. T. The Surface Chemistry of Amorphous Silica. Zhuravlev Model. *Colloids and Surfaces A: Physicochemical and Engineering Aspects* **2000**, *173*, 1–38.

(33) Kulkarni, S. A.; Mirji, S. A.; Mandale, A. B.; Vijayamohanan, K. P. Thermal Stability of Self-Assembled Octadecyltrichlorosilane Monolayers on Planar and Curved Silica Surfaces. *Thin Solid Films* **2006**, *496*, 420–425.

(34) Shirai, M.; Morishita, S.; Okamura, H.; Tsunooka, M. Photo-Cross-Linkable Polymers with Thermally Degradable Property. *Chem. Mater* **2002**, *14*, 334–340.

(35) Okamura, H.; Yamauchi, E.; Shirai, M. Photo-Cross-Linking and de-Cross-Linking of Modified Polystyrenes Having Degradable Linkages. *Reactive and Functional Polymers* **2011**, *71*, 480–488.

(36) Conlon, D. A.; Crivello, J. V.; Lee, J. L.; O'Brien, M. J. The Synthesis, Characterization, and Deblocking of poly(4-Tert-Butoxystyrene) and poly(4-Tert-Butoxy-.alpha.-Methylstyrene). *Macromolecules* **1989**, *22*, 509–516.

(37) Wang, Y.; Lieberman, M. Growth of Ultrasmooth Octadecyltrichlorosilane Self-Assembled Monolayers on SiO2. *Langmuir* **2003**, *19*, 1159–1167.

(38) Onclin, S.; Ravoo, B. J.; Reinhoudt, D. N. Engineering Silicon Oxide Surfaces Using Self-Assembled Monolayers. *Angewandte Chemie (International ed. in English)* **2005**, *44*, 6282–6304.

5. Anti-fouling films

5.1. Introduction

Prevention of protein and bacterial adhesion is sought in many industries and for many applications, including indwelling medical devices (catheters, joint prostheses, contact lenses, pace makers, etc.),[1–4] bioassays,[5] desalination membranes,[6] and marine vehicle coatings.[7,8] Accumulation of foulants at surfaces can severely limit product safety and efficiency, as in the formation of infectious biofilms on central veinous catheters,[9] or the increased drag at ship hulls coated with algae and invertebrates.[10] This study is a collaboration with the Belfort group at Rensselaer Polytechnic Institute, who graft a diverse library of monomers to filtration membranes and screen the membranes for protein adsorption and filtration performance.[11–14] We wish to develop a better mechanistic understanding of the role of water structure in determining susceptibility to protein adhesion. Specifically, I examine the effect of phosphate ions on water structure at treated poly (ether sulfone) membranes using sum frequency generation (SFG) spectroscopy.

Designing a surface to resist fouling from a diverse feed stock is challenging due to the range in protein size, shape, and charge. Even individual proteins are heterogeneous, having hydrophilic, hydrophobic, cationic, and anionic patches. Still, there are materials that impart general surface passivity. These include polymers of ethylene oxide, zwitterions, balanced charge mixtures of positively and negatively-charged monomers, saccharides, and polypeptides, and all (1) bind water molecules tightly, but (2) do not induce long-range ordering of water molecules. For instance, water hydrogen-bonds strongly to the oxygens in loosely packed[15] poly(ethylene

glycol) (PEG),[16–20] but returns to bulk structure within two water layers. Sugars,[21–23] such as mannitol,[24] are an interesting case. The hydroxyl groups of some monosaccharides are camouflaged in water due to their congruence with the hydrogen bonding network of bulk water, causing them to behave as hydrophobic solutes.[25] Zwitterionic and balanced mixed charge films also impart resistance to adhesion.[26,27] While water molecules are strongly aligned by and attracted to charge centers, the spatial distribution and balance of the charges scrambles the structure of the interfacial water overall.[28–30] Thus, at short length scales an anti-fouling surface binds tightly to water molecules to resist displacements by adsorbates, and at long length scales conceals the presence of the interface.

Clearly the charge of an interface is a concern as a surface potential will orient water dipoles, and may directly interact with a charged solute. But when previous studies have probed water structure at anti-fouling surfaces, they generally use neat water[18,26,31–33] even when fouling and filtration metrics are determined using biological buffers. Therefore, it is relevant to determine how charged species within a buffer interact with the membrane surface and affect the water structure. Here we use SFG spectroscopy to investigate the water structure at a series of chemically modified filtration membranes. SFG is a nonlinear optical vibrational spectroscopy sensitive only to molecules in interfacial regions, and can be used to probe buried surfaces.[34,35] SFG is the ideal tool for probing water structure at solid substrates such as films and membranes.[32,33,36–42]

Whereas ions are isotropically distributed in the bulk, they assume structured density profiles at surfaces. The surface propensity differs among ionic species, which can lead to a charge separation and therefore a surface field in solutions with ions of dissimilar surface activities.[43,44] Ion distribution is determined by the interfacial water structure, ion hydration energy, and the

presence of other ions, among other factors.[44–49] Specific ion effects were first observed in the nineteenth century, when Franz Hofmeister observed that some salts caused ovalbumin to retain its structure and precipitate (kosmotropes) and others to denature and solubilize (chaotropes).[50] Hofmeister effects are observed in other phenomena, where the cations and anions can be ordered by their effect on protein solubility, on water surface tension, and many other interfacial aqueous processes, to generate essentially the same series.[47] The terms kosmotrope and chaotrope have their roots in the idea that a salt's effect on proteins is due to the ordering or disordering of the bulk structure of water. However, while ions interact with water to different extents and weak long range effects do exist at low salt concentrations, it is now generally agreed that the ions strongly affect the water structure only in the first one to two solvation shells at physiological salt concentrations and the Hofmeister effect is likely a surface phenomenon.[51–54]

In this work we examine the water structure at three polymeric surfaces with different chemistries and fouling resistance: unmodified (polyether sulfone) PES, PES modified with hydrophobic alkane (C18, promotes protein adhesion), and PES modified with poly(ethylene glycol) (PEG, resists adhesion). Water at these films was examined in neat water, 0.01 M phosphate buffer (ionic strength 0.166), and phosphate buffered saline (PBS, I=0.025 M). The functionalized surfaces were prepared by spin-coating poly(ether sulfone) (PES) onto a CaF_2 wafer forming a thin polymer film, which was subsequently modified with alkane and PEG surfaces chemistries. We observe that the specific ion interactions within the phosphate buffer at low ionic strengths lead to a surface charge causing a large degree of water structuring, which is screened at high ionic strengths and absent in neat water.

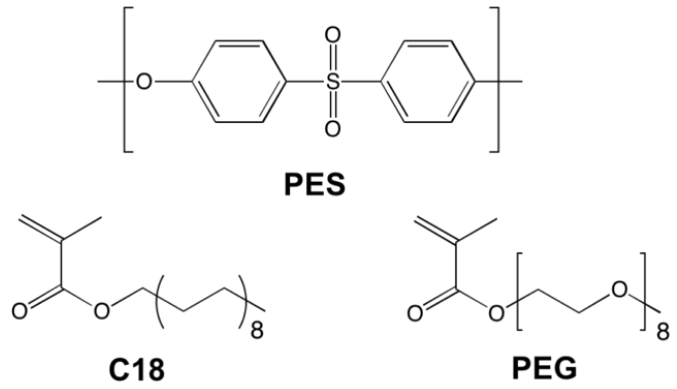

Figure 5.1 Membrane material poly(ether sulfone) (PES) and grafting polymers C18 and PEG).

5.2. Materials and Methods

5.2.1. Preparation of poly(ether sulfone) (PES) film

PES films were prepared and modified by Joseph Imbrogno at Rensselaer Polytechnic Institute. Poly(ether sulfone) (PES, Ultrason®, BASF Corporation, Wyandotte, MI) powder was dissolved in dichloromethane (Sigma-Aldrich) to make a 1% (w/v) solution. PES was applied to CaF_2 wafers (Crystran Limited, 25 mm diameter, 1 mm thick) on the same side as a sputter-coated spot of gold, used for reference in SFG analysis. Using an 8 in. Headway Spinner (Headway Research, Inc., Garland, Texas), PES solution was deposited onto the CaF_2 surface and ramped by 1000 rpm s^{-1} to 3000 rpm, then spun at 3000 rpm for 20 s, and then ramped down to 0 rpm at 1000 rpm s^{-1}. The films were annealed at 120°C for 30 min with heating and cooling rates of < 1 °C min^{-1} to avoid thermal stress on the wafers and to relax the spin-coated layer into a stable state. After annealing, they were kept covered at room temperature.

5.2.2. Surface Activation and Grafting of PES films

PES coated CaF_2 wafers were pre-soaked in Milli-Q water overnight prior to modification. They were then exposed to an atmospheric pressure plasma (APP) source (model ATOMFLO, Surfx

Technologies LLC, Culver City, CA) for 6 min at a helium flow rate of 30.0 L min^{-1}, an oxygen flow rate of 0.4 L min^{-1}, and a source-to-membrane distance of 20 mm. The plasma source was operated at 140 W and driven by a radiofrequency power at 27.12 MHz. An XYZ Robot (Surfx Technologies LLC) was used to control the plasma source over the plate with a scan speed of 6 mm s^{-1}. Following exposure to the plasma and subsequent formation of radicals at the membrane surface, 5 mL of each monomer solution (PEG was dissolved in water and C18 was dissolved in absolute ethanol) was added to each wafer in 30 mL beakers. The poly(ethylene glycol) methyl ether methacrylate (n=8) (PEG) and stearyl methacrylate (C18) monomers were purchased from Sigma-Aldrich (Figure 5.1). The beakers were then covered and placed in an oven. Graft polymerization of monomers was immediately initiated at 60 ± 1°C for 2 h. After removing the monomer solutions, the wafers were rinsed and soaked with pure ethanol for 24 h to remove any homopolymer and unreacted monomer residue from the membrane surfaces. The wafers were then dried and stored at room temperature before SFG measurements.

5.2.3. Atomic Force Microscopy Measurements

Atomic force microscopy (AFM; MFP 3D, Asylum Research, Santa Barbara, California) images of spin-coated PES on CaF_2 wafers were collected by Joseph Imbrogno. The root mean square (RMS) roughness of the PES layer before and after modification were calculated from 5 x 5 μm scans with 512 measurements/line in at least two different areas of the sample.

5.2.4. Sum Frequency Generation Spectroscopy

Sum frequency generation spectra were acquired in this laboratory. The films were probed in reflection at the buried interface through the substrate, both dry and in contact with aqueous solutions using the liquid cell detailed in Figure 2.8. Sum frequency signal was generated largely as described in Chapter 3, with the following differences. The frequency range of the IR

broadband pulses was extended to cover 2400 - 4000 cm^{-1} by purging the point of IR to SFG generation of water vapor and CO_2 and using a 2505 nm long pass filter (Spectrogon, Ge) to filter out idler signal from the OPA. The visible (10 mJ, 60º) and IR (4.5 mJ, 65º) beams were focused and overlapped on the film, and the SFG signal was dispersed by an Acton SP-2500i monochromator (Princeton Instruments, 600 grooves/mm grating blazed at 500 nm) and imaged on a liquid nitrogen cooled Spec-10 CCD camera (Princeton Instruments, 1340 × 400 pixels).

Sample spectra were collected in *ssp* (SFG, visible, and IR, respectively) polarizations, while the nonresonant spectra from gold used for normalization were collected in *ppp* polarization. '*s*' ('*p*') indicates polarization parallel (perpendicular) to the sample plane. Each sample window had a section of gold film used for generating this nonresonant signal. Background spectra were taken by introducing a large time delay (20 ps) between the visible and IR beams, in order to subtract dark counts and scattered light. Prior to characterization, PES films were rinsed in ultrapure water, dried with N_2, and equilibrated with the climate controlled laboratory atmosphere (70±0.5 ºF and 35±2 % relative humidity). SFG spectra of the PES films were acquired for multiple samples of each film type, and in multiple locations on each sample, to determine sample variability. Spectra were taken of the dry films in the CH stretch region, 2800-3200 cm^{-1}. Two to four spectra were averaged for each sample of each film type (Figure 5.4).

5.2.5. Water Structure

To examine water structure, samples were loaded into the liquid cell. All components apart from the sample were soaked in Nochromix solution, prepared by dissolving Nochromix cleaning reagent (Godax Laboratories) in concentrated sulfuric acid (Fisher Scientific, certified ACS Plus), and then rinsed in ultrapure water (18.2 MΩ·cm @25 °C, 5 ppb TOC). Phosphate buffer (10 mM, pH 7.5) was prepared by dissolving NaH_2PO_4 (Sigma, 98%+, anhydrous) and Na_2HPO_4

(Fisher Scientific, certified ACS, anhydrous) in ultrapure water. Phosphate buffered saline (PBS) from a powder (Sigma) was prepared with ultrapure water (10 mM phosphate, 138 mM NaCl, 2.7 mM KCl, pH 7.5, I=0.166 M). All glassware used for preparing solutions was cleaned with Nochromix solution and rinsed with ultrapure water. Solutions were filtered through a nylon syringe filter (Cameo, 0.22 mm).

SFG spectra of the buried film/air, phosphate buffer, and PBS interfaces were taken on two or three different samples of each film type. Two were averaged for each spectrum (Figure 5.5). They were normalized to the nonresonant gold spectrum taken from a gold spot applied to the window of the same sample to account for both IR intensity envelope and visible and IR beam powers. To cover the CH and OH stretch regions (2700-3800 cm^{-1}), the IR wavelength was tuned to 2700, 2900, 3100, 3300, and 3500 nm and the resulting SFG spectra were averaged together.

5.3. Results

5.3.1. Films at neat water

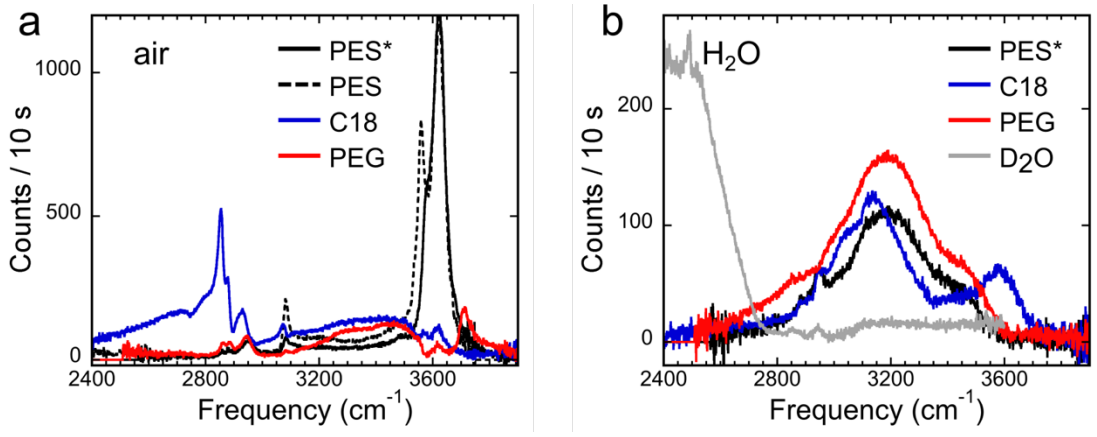

Figure 5.2 SFG spectra of PES membranes at very low graft concentration of PEG (0.002 M, PES*), pure PES (PES), C18 modified PES (C18), and PEG-modified PES (2.0 M, PEG): (a) damp films, and (b) films at H_2O. For comparison, an unmodified PES film at D_2O is shown in gray.

In the first stage of this study, PES films were characterized at air and neat water. PES and C18 and PEG modified PES films were rinsed and dried immediately before mounting for analysis without an equilibration period in laboratory atmosphere, leading to 'damp' films. In Figure 5.2 a, we see SFG spectra spanning the CH stretch and OH stretch region for the air interface. Aliphatic (2800 - 3000 cm^{-1}) and aromatic (~3075) CH stretch modes are visible. Weak H-bonded OH signal is also present (< 3550 cm^{-1}). What is particularly interesting about these damp films are the sharp OH modes above 3550 cm^{-1}. Bare PES membrane has two intense peaks arising from H-bonding of water monomers with the π-system of the phenyl moieties, a symmetric and asymmetric OH stretching mode.[55–57] The large intensity indicates ordering of the PES with respect to the interface, as signal from water molecules bonding to the π-systems adds constructively and does not cancel. The same peak pair appears in the spectrum of damp C18, reduced in intensity perhaps from the layer of C18 between PES and film surface. No free OH consistent with interaction with C18 itself is present. The spectrum of PEG-modified film has an additional peak at 3712 cm^{-1}, matching the frequency of non-hydrogen bonded OH vibrations of water at the neat water/air interface. As PEG is hydrophilic, it is likely coated with layers of water molecules, the topmost of which is similar to that at the neat water/air interface.

At the interface with bulk H_2O (Figure 5.2 b), the narrow peaks due to non-hydrogen bonded water molecules and water molecules hydrogen bonding with phenyl groups are predictably gone. Hydrogen-bonded OH modes now dominate. Intensity peaks around 3150 cm^{-1} for all films, but the range in frequency (2400 - 3650 cm^{-1}) indicates a wide range in hydrogen bonding strengths. Both intensity and peak shape are similar for all film types. When H_2O is replaced

with D_2O at unmodified PES Figure 5.2 b, gray), all the OH stretch signal disappears, leaving only the CH stretches and the higher frequency end of the H-bonded OD stretch.

5.3.2. Sample Variability

Studies of materials such as the modified PES membranes examined in this study are directly relevant to products used outside the laboratory setting, but they are also more complex and heterogeneous than simpler model systems. The dry PES films were first assessed for consistency both spatially across single samples, and for multiple samples of the same film type. To maximize the number of sites that could be sampled, only the region from 2800 - 3150 cm^{-1} was probed. This covers the aliphatic C-H stretch (2820 - 3000 cm^{-1}) and the single aromatic C-H stretch from the PES (3080 cm^{-1}). Spectra were taken at four positions on each sample (Figure 5.3). Within the same sample, the spectra are consistent both in the frequency and relative intensity of peaks. There is some variation in the overall intensity, likely due to scattering from the polymer surface, which exhibits roughness within the laser spot size of a few hundred microns. Comparing spectra taken on different samples of the same film type, the relative height of the peaks varies somewhat, but the frequencies are the same. Figure 5.4 shows the sample-to-sample variation. Shifts in peak heights, such as in the aromatic CH peak, could indicate differences in polymer orientation or density. Considering the porous and loose structure of the films, some amount of variation is to be expected. Overall, the degree of similarity both within and between samples of the same film type indicates that the samples are fairly uniform, and a small number of spectra are representative of the materials.

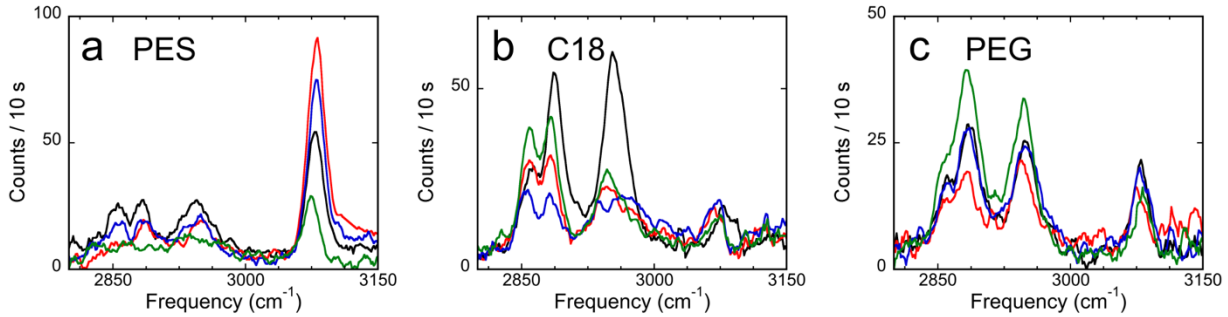

Figure 5.3 Variation within individual samples: SFG spectra taken at four positions on one sample of (a) unmodified PES, (b) C18, and (c) PEG.

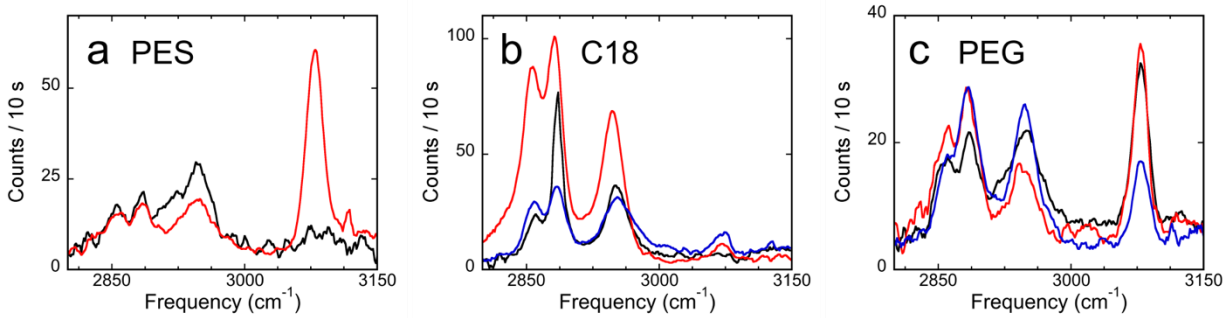

Figure 5.4 Variation between different samples of the same film type: Average of SFG spectra taken at each sample of (a) unmodified PES, (b) C18, and (c) PEG.

AFM images were taken of each sample and an increase in the roughness was observed after modification, as expected. Overall, the unmodified and modified films were smooth at the micron and sub-micron length scale with average RMS roughness values of 0.5 ± 0.1 nm, 1.4 ± 0.4 nm, and 2.2 ± 1.4 nm for unmodified PES, C18 modified PES, and PEG modified PES, respectively. The AFM data is not contradicted by the observed scattering, which is explained by the presence of roughness on a longer length scale within the beam spot size of the laser on the sample. Such scattering would reduce the overall efficiency of SFG detection, but as the samples are smooth relative to the SFG coherence length (60 μm), would not manifest as increased disorder of the polymer or any other spectral change.

5.3.3. PES films in air, phosphate buffer, and PBS

Having confirmed the consistency of the samples, the frequency range was expanded to include the OH stretch region of water in addition to CH stretch. The water spectrum of bulk water stretches from roughly 3000 to 3650 cm^{-1}, with two broad peaks at ~3200 cm^{-1} and ~3400 cm^{-1}. Water molecules can exhibit a range in the number of hydrogen bonding partners that is reflected in the range of OH stretch bond frequencies.[58] While individual hydrogen-bonding geometries exhibit broad OH stretch frequency distributions, generally stronger H-bonding correlates to weaker OH stretch bonds and therefore lower OH frequencies. Broadly speaking, frequencies around 3200 cm^{-1} are characteristic of more tetrahedrally-coordinated (bulk-like) water, where frequencies around 3400 cm^{-1} contain larger contributions from incomplete H-bonding (water has fewer than two donor and two acceptor bonds).[59]

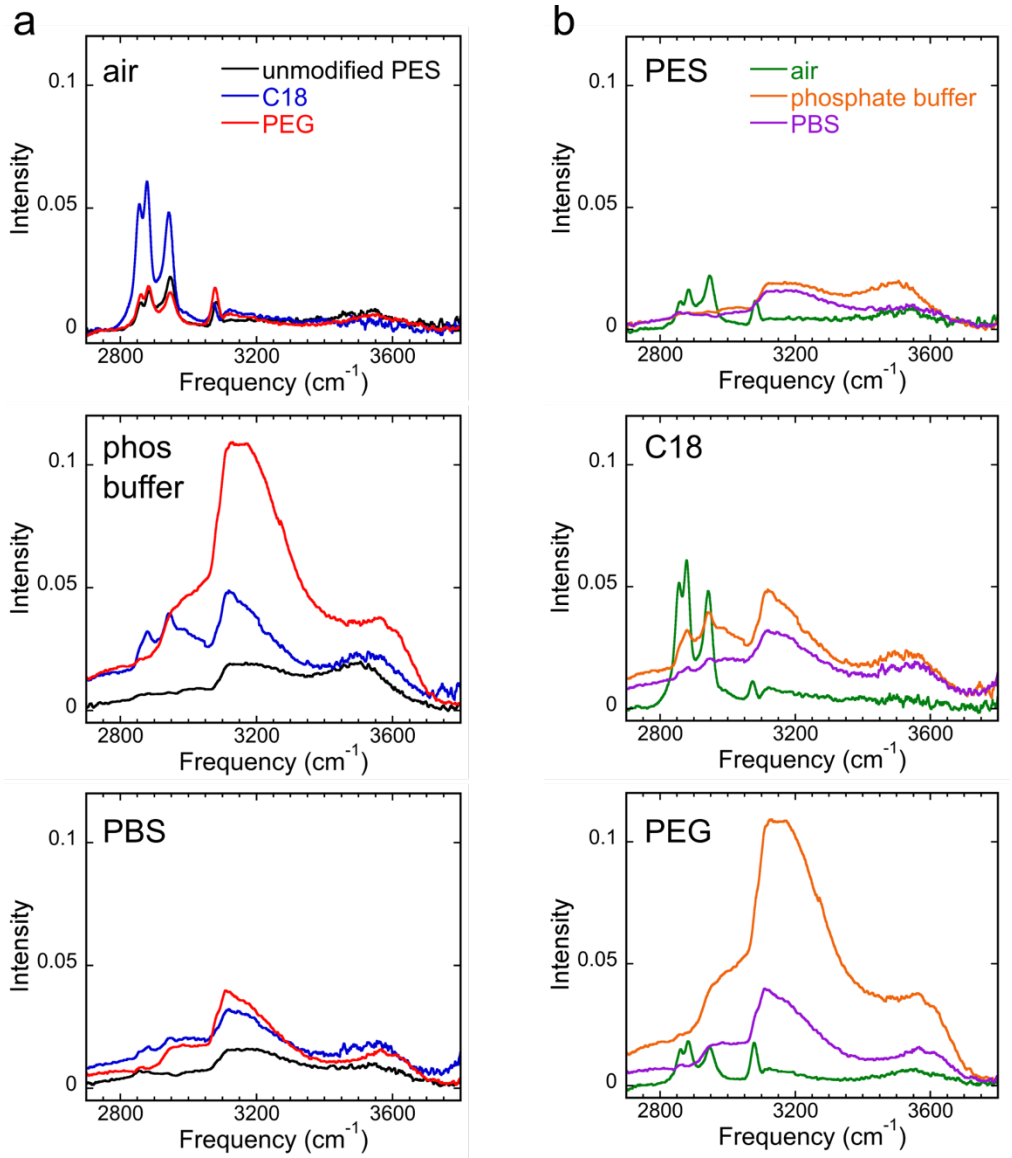

Figure 5.5 PES films in air, phosphate buffer (I=0.025 M), and PBS solution (I=0.166 M) arranged by (a) fluid type, and (b) film type.

The spectra averaged over two or three different samples of the films in contact with air, low salt phosphate buffer, and PBS solution are shown in Figure 5.5. For films in contact with air (Figure 5.5 a, top) the spectra are nearly flat in the OH stretch region. The small bump around 3500 cm^{-1} is likely due to surface-adsorbed water from the 35% relative humidity in the laboratory air. The same films in contact with the 0.01 M phosphate buffer solution Figure 5.5a, middle) display a broad SFG signal from 2700 to 3700 cm^{-1} with main features at 3150 cm^{-1} and 3500 cm^{-1}. The

PEG film has the highest intensity in the OH region with a large peak at 3150 cm^{-1} (strongly H-bonded water), followed by C18 and then bare PES. The CH stretching modes of the wetted films are much smaller than those of the dry films due to less efficient reflection of the SFG signal at the sample/solution boundary. The steep increase in intensity at 3075 cm^{-1} for all films is due to destructive interference between the aromatic CH and OH stretching modes. At 0.01 M phosphate buffered saline (PBS) (Figure 5.5 a, bottom) the addition of 138 mM NaCl to the phosphate buffer leads to a large decrease in OH intensity for PEG, some decrease in C18, and little change in the unmodified PES. The decrease is mainly in the lower frequency peak for C18 and PEG. The large reduction in OH intensity upon increasing the NaCl concentration (0 mM for phosphate buffer, 138 mM for PBS) suggests that the large OH intensities at the phosphate buffer are due to a surface potential arising from the ion-specific surface propensities of the phosphate and sodium ions.

5.4. Discussion

When an interface is charged, the resulting electric field from the overall surface potential reorients the interfacial water molecules, widening the interface over the length-scale of the Debye length (the length over which the surface electric field decays). The aligned water molecules give rise to an increased effective second-order nonlinear response. This is generally referred to as the Eisenthal $\chi^{(3)}$ effect and has been used to examine both the water structure and to determine the surface potential for a variety of surfaces.[60–64] Surface potentials can also be generated at innately neutral materials by the unequal attraction of certain cations and ions, resulting in a local charge imbalance. For instance, surface potentials have been generated at the neutral water/air interface upon the addition of different salts.[43,44,65,66] Water alignment driven by

a surface potential can be distinguished from more direct surface interactions by observing water ordering as a non-surface-active salt, such as NaCl, is added to the solution. As the ionic strength is increased, the Debye length is decreased, screening the surface potential if it is present. The large decrease in the water ordering for the PBS solution compared with the low salt phosphate buffer (Figure 5.5 b) is thus reflective of a surface potential caused by differential ion adsorption of the single and particularly doubly valent phosphate ions versus the sodium counter ions. More interestingly, the differences in the water structure (and subsequent reduction of water structure upon addition of salt) among the PEG, C18 and unmodified PES surfaces reflect differences in specific ion interactions between the different surface chemistries.

Previous studies have found phosphate anions to be excluded from the hydration layer of ethylene glycol polymers.[67–69] Initially, it seems surprising that a hydrophilic polymer such as PEG should exhibit the same Hofmeister series effects typical of hydrophobic interfaces. Water bonds strongly to the ethylene oxide residues of PEG. The kinks in loosely packed PEG monomers are driven by water molecules bridging two adjacent oxygen atoms to donate two hydrogen bonds. Hydrogen-bonding between water and PEG is stronger than that between water molecules,[16] and multiple simulations and experiments confirm the presence of strongly-bound water at the PEG.[17–20,70] However, the placement of water molecules is highly constrained and therefore entropically unfavorable. The attraction between adjacent PEG monomers can pull the strands together, squeezing out and excluding water molecules from binding.[69] Ions outcompete PEG for water to complete their hydration shells, leading to a low-salt region surrounding PEG which is largest for ions with large hydration energies, such as mono- and divalent phosphate.

As discussed above, a disparity in surface propensity between anions and cations, such as between Na^+ and HPO_4^{2-}, results in charge separation and creates an electric field near the

interface. In the phosphate buffer and PBS solutions (pH ~7.4), the divalent phosphate anion is predominant. Considering the position of $H_2PO_4^-$ and HPO_4^{2-} in the Hofmeister series, their large hydration shells,[71] and their use in driving the phase separation of PEG/phosphate salt aqueous systems,[72–74] it is clear that these anions are excluded from the surface of PEG. While Na^+ is on the more strongly hydrated, "kosmotrope," side of the series in terms of its interaction with PEG,[67,69] the effect of cations on the phase diagram of PEG solutions is much smaller than that of anions, and so Na^+ probably sits much closer to the PEG/water interface than do the phosphate anions. Accordingly, a sodium phosphate solution at PEG forms an electric double layer, with sodium and chloride ions several angstroms from the polymer, and $H_2PO_4^-$ and then HPO_4^{2-} a few layers of H_2O away from the surface (Figure 5.6 a & c). The electrical double layer will increase the SFG OH intensity by deepening the layer of water molecules that is noncentrosymmetric (SFG active). The water in the electric double layer will be oriented with oxygens towards the net positively charged interface, and since it is not in direct contact with the PEG, will be more strongly hydrogen-bonded and bulk-like. The large peak of the PEG film at 0.01 M phosphate buffer (Figure 5.5 b, bottom) at 3150 cm^{-1} supports this interpretation.

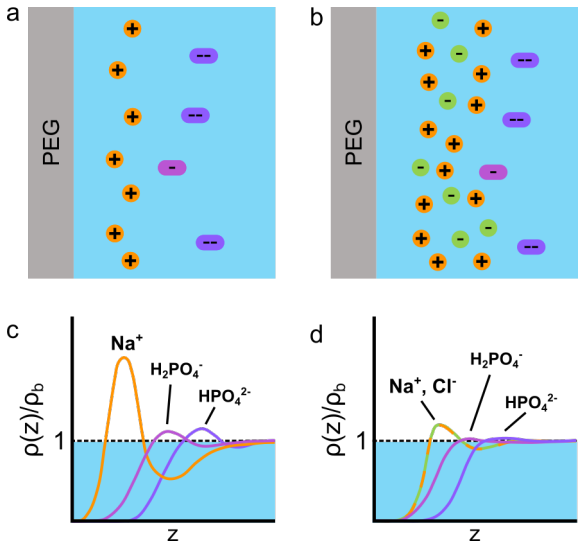

Figure 5.6 Schematic of ion distribution at the PEG interface in (a) phosphate buffer (I=0.025 M) and (b) phosphate buffered saline (PBS) (I=0.166 M). Schematic of density, $\rho(z)$, normalized to the bulk density, ρ_b, as a function of distance from the Gibbs dividing surface, z, for phosphate buffer (c) and PBS (d).

Addition of a much larger concentration of NaCl to the phosphate buffer (138 mM) will disrupt the water ordering by decreasing the Debye length.[75] In Figure 5.6 b and d, the excess of chloride ions at the PEG surface largely negates the effect of the sodium ions in generating a positive surface potential. The static electric surface field which orients water molecules at the phosphate buffer is neutralized by PBS, leading to the large decrease in the OH intensity for PEG at the phosphate buffer (Figure 5.5 b). Studies of aqueous PEG/phosphate systems with and without added NaCl have found that the addition of NaCl shifts the onset of phase separation toward lower phosphate and PEG concentrations, and that adding NaCl increases chromatographic resolution of proteins by salting them out of the phosphate salt phase.[76,77] The reduction in the phosphate and PEG concentrations for phase separation and salting out the proteins suggests that Na^+ and Cl^- are excluded from the PEG surface somewhat, though to a smaller degree than phosphate. For the PBS solution (0.138 M Na^+, 0.141 M Cl^-, 0.0027 M K^+, 0.01 M phosphate), chloride and sodium will be closest to the interface, followed by the monovalent and divalent phosphates. Since sodium and chloride exhibit similar surface propensity, they effectively screen

the surface field and greatly reduce the degree of water ordering. Indeed, spectra of the films at PBS, where the surface charge is masked, look very similar to spectra of the films at neat water (Figure 5.2), where there is no phosphate anion to create a surface charge.

The C18 -modified PES film is hydrophobic, making simulations and experiments of air/water and air/oil interface studies applicable to understanding the distribution of ions at this surface. While phosphate anions at water interfaces have not been studied, the divalent HPO_4^{2-} probably acts similarly to the SO_4^{2-}, which is more kosmotropic.[67,78] At the air/water interface, the sulfate in both 1.2 M $(NH_4)_2SO_4$ and Na_2SO_4 is buried below the cation.[79] This creates an electrical double layer which aligns water molecules and increases the SFG OH stretch intensity, particularly around 3150 cm^{-1}, characteristic of more bulk-like water. As expected, phosphate buffer at C18-modified PES has the same effect of increasing the low-frequency OH stretch response (Figure 5.5 b, middle). C18 induces the same ion distribution as seen at PEG but to a much smaller degree, causing a somewhat higher OH intensity at the phosphate buffer solution, and a reduction in intensity at PBS. The smaller OH intensity for C18 compared to PEG at the phosphate buffer, coupled with the proportionately smaller 3150 cm^{-1} peak (tetrahedrally-structured water) for C18, suggests that the charge separation is significantly less pronounced at C18 than at PEG. While the unmodified PES film is also somewhat hydrophobic, there does not appear to be any electrostatically-induced increase in OH intensity.

5.5. Conclusions

Sum-frequency generation spectroscopy was used to examine the water ordering at functionalized PES surfaces in contact with neat water and phosphate buffers at low- and high-

ionic strength. Structured water is observed at all films in contact with low-salt phosphate buffer. Large differences in the intensity of OH stretching modes between film types are seen, with PEG>C18>PES. The large reduction of the OH stretch modes upon the addition of salt indicates that the increase in OH intensity emanates mainly from strongly hydrogen bonded water molecules oriented in a surface field. The surface deficit of strongly hydrated phosphate anions relative to sodium cations at the interface creates a static electric field that orients water molecules more deeply into the bulk. The surface field is responsible for the large OH response at the phosphate buffer, especially in the strongly H-bonded 3150 cm^{-1} region characteristic of tetrahedral bulk-like water molecules aligned in a surface field. The addition of a large concentration of sodium chloride (PBS solution, I=0.166 M) reduces the electrostatic effect by screening the surface charges and dissipating the ordered water structure. The effect is strong for PEG-functionalized PES, significantly less pronounced for C18-functionalized PES, and essentially absent for unmodified PES. This in turn means that phosphate is strongly excluded from PEG, less so from C18, and not excluded from unfunctionalized PES surface, illustrating the chemical sensitivity to the specific-ion effects. Our results show that phosphate buffer strongly influences the interfacial water structure at different types of modified polymer films. Investigations of the interplay between water structure and protein resistance must be performed under physiologically relevant conditions.

References

(1) Cheng, W.; Yang, C.; Ding, X.; Engler, A. C.; Hedrick, J. L.; Yang, Y. Y. Broad-Spectrum Antimicrobial/Antifouling Soft Material Coatings Using Poly(ethylenimine) as a Tailorable Scaffold. *Biomacromolecules* **2015**, *16*, 1967–1977.

(2) Pavithra, D.; Doble, M. Biofilm Formation, Bacterial Adhesion and Host Response on Polymeric Implants--Issues and Prevention. *Biomedical materials (Bristol, England)* **2008**, *3*, 034003.

(3) Donlan, R. M. Biofilm Formation: A Clinically Relevant Microbiological Process. *Clinical infectious diseases : an official publication of the Infectious Diseases Society of America* **2001**, *33*, 1387–1392.

(4) Selan, L.; Palma, S.; Scoarughi, G. L.; Papa, R.; Veeh, R.; Di Clemente, D.; Artini, M. Phosphorylcholine Impairs Susceptibility to Biofilm Formation of Hydrogel Contact Lenses. *American journal of ophthalmology* **2009**, *147*, 134–139.

(5) Hucknall, A.; Kim, D. H.; Rangarajan, S.; Hill, R. T.; Reichert, W. M.; Chilkoti, A. Simple Fabrication of Antibody Microarrays on Nonfouling Polymer Brushes with Femtomolar Sensitivity for Protein Analytes in Serum and Blood. *Advanced Materials* **2009**, *21*, 1968–1971.

(6) Khalid, A.; Al-Juhani, A. A.; Al-Hamouz, O. C.; Laoui, T.; Khan, Z.; Atieh, M. A. Preparation and Properties of Nanocomposite Polysulfone/multi-Walled Carbon Nanotubes Membranes for Desalination. *Desalination* **2015**, *367*, 134–144.

(7) Ciriminna, R.; Bright, F. V.; Pagliaro, M. Ecofriendly Antifouling Marine Coatings. *ACS Sustainable Chemistry & Engineering* **2015**, *3*, 559–565.

(8) Callow, M. E.; Callow, J. E. Marine Biofouling: A Sticky Problem. *Biologist (London, England)* **2002**, *49*, 10–14.

(9) Sousa, C.; Henriques, M.; Oliveira, R. Mini-Review: Antimicrobial Central Venous Catheters – Recent Advances and Strategies. *Biofouling* **2011**.

(10) Lindholdt, A.; Dam-Johansen, K.; Olsen, S. M.; Yebra, D. M.; Kiil, S. Effects of Biofouling Development on Drag Forces of Hull Coatings for Ocean-Going Ships: A Review. *Journal of Coatings Technology and Research* **2015**, *12*, 415–444.

(11) Zhou, M.; Liu, H.; Kilduff, J. E.; Langer, R.; Anderson, D. G.; Belfort, G. High Throughput Synthesis and Screening of New Protein Resistant Surfaces for Membrane Filtration. *AIChE Journal* **2010**, *56*, 1932–1945.

(12) Zhou, M.; Liu, H.; Venkiteshwaran, A.; Kilduff, J.; Anderson, D. G.; Langer, R.; Belfort, G. High Throughput Discovery of New Fouling-Resistant Surfaces. *Journal of Materials Chemistry* **2011**, *21*, 693–704.

(13) Gu, M.; Vegas, A. J.; Anderson, D. G.; Langer, R. S.; Kilduff, J. E.; Belfort, G. Combinatorial Synthesis with High Throughput Discovery of Protein-Resistant Membrane Surfaces. *Biomaterials* **2013**, *34*, 6133–6138.

(14) Imbrogno, J.; Williams, M. D.; Belfort, G. A New Combinatorial Method for Synthesizing, Screening, and Discovering Antifouling Surface Chemistries. *ACS applied materials & interfaces* **2015**, *7*, 2385–2392.

(15) Harder, P.; Grunze, M.; Dahint, R.; Whitesides, G. M.; Laibinis, P. E. Molecular Conformation in Oligo(ethylene Glycol)-Terminated Self-Assembled Monolayers on Gold and Silver Surfaces Determines Their Ability To Resist Protein Adsorption. *The Journal of Physical Chemistry B* **1998**, *102*, 426–436.

(16) Wang, R. L. C.; Kreuzer, H. J.; Grunze, M. Molecular Conformation and Solvation of Oligo(ethylene Glycol)-Terminated Self-Assembled Monolayers and Their Resistance to Protein Adsorption. *The Journal of Physical Chemistry B* **1997**, *101*, 9767–9773.

(17) Bandyopadhyay, S.; Chanda, J. Monolayer of Monododecyl Diethylene Glycol Surfactants Adsorbed at the Air/Water Interface: A Molecular Dynamics Study. *Langmuir* **2003**, *19*, 10443–10448.

(18) Tyrode, E.; Johnson, C. M.; Kumpulainen, A.; Rutland, M. W.; Claesson, P. M. Hydration State of Nonionic Surfactant Monolayers at the Liquid/vapor Interface: Structure Determination by Vibrational Sum Frequency Spectroscopy. *Journal of the American Chemical Society* **2005**, *127*, 16848–16859.

(19) Mafi, A.; Hu, D.; Chou, K. C. Interactions of Water with the Nonionic Surfactant Polyoxyethylene Glycol Alkyl Ethers Studied by Phase-Sensitive Sum Frequency Generation and Molecular Dynamics Simulation. *Special issue dedicated to Gabor Somorjai's 80th birthday* **2016**, *648 IS* -, 366–370.

(20) Ohe, C.; Goto, Y.; Noi, M.; Arai, M.; Kamijo, H.; Itoh, K. Sum Frequency Generation Spectroscopic Studies on Phase Transitions of Phospholipid Monolayers Containing Poly(ethylene Oxide) Lipids at the Air-Water Interface. *The Journal of Physical Chemistry B* **2007**, *111*, 1693–1700.

(21) Hower, J. C.; Bernards, M. T.; Chen, S.; Tsao, H.-K.; Sheng, Y.-J.; Jiang, S. Hydration of 'Nonfouling' Functional Groups. *The Journal of Physical Chemistry B* **2009**, *113*, 197–201.

(22) Pertsin, A. J.; Grunze, M. Computer Simulation of Water near the Surface of Oligo(ethylene Glycol)-Terminated Alkanethiol Self-Assembled Monolayers. *Langmuir* **2000**, *16*, 8829–8841.

(23) Otto, S.; Engberts, J. B. F. N. Hydrophobic Interactions and Chemical Reactivity. *Organic & Biomolecular Chemistry* **2003**, *1*, 2809–2820.

(24) Yan-Yeung Luk; Mihoko Kato, and; Mrksich, M. Self-Assembled Monolayers of Alkanethiolates Presenting Mannitol Groups Are Inert to Protein Adsorption and Cell Attachment. *Langmuir* **2000**, *16*, 9604–9608.

(25) Galema, S. A.; Blandamer, M. J.; Engberts, J. B. F. N. Stereochemical Aspects of Hydration of Carbohydrates in Aqueous Solutions. 2. Kinetic Medium Effects. *The Journal of Organic Chemistry* **1992**, *57*, 1995–2001.

(26) Nagasawa, D.; Azuma, T.; Noguchi, H.; Uosaki, K.; Takai, M. Role of Interfacial Water in Protein Adsorption onto Polymer Brushes as Studied by SFG Spectroscopy and QCM. *Journal Of Physical Chemistry C* **2015**, *119*, 17193–17201.

(27) Holmlin, R. E.; Chen, X.; Chapman, R. G.; Takayama, S.; Whitesides, G. M. Zwitterionic SAMs That Resist Nonspecific Adsorption of Protein from Aqueous Buffer. *Langmuir* **2001**, *17*, 2841–2850.

(28) Chen, X.; Hua, W.; Huang, Z.; Allen, H. C. Interfacial Water Structure Associated with Phospholipid Membranes Studied by Phase-Sensitive Vibrational Sum Frequency Generation Spectroscopy. *J. Am. Chem. Soc* **2010**, *132*, 11336–11342.

(29) Kondo, T.; Gemmei-Ide, M.; Kitano, H.; Ohno, K.; Noguchi, H.; Uosaki, K. Sum Frequency Generation Study on the Structure of Water in the Vicinity of an Amphoteric Polymer Brush. *Colloids and surfaces. B, Biointerfaces* **2012**, *91*, 215–218.

(30) Mondal, J. A.; Nihonyanagi, S.; Yamaguchi, S.; Tahara, T. Three Distinct Water Structures at a Zwitterionic Lipid/Water Interface Revealed by Heterodyne-Detected Vibrational Sum Frequency Generation. *J. Am. Chem. Soc* **2012**, *134*, 7842–7850.

(31) Kondo, T.; Nomura, K.; Gemmei-Ide, M.; Kitano, H.; Noguchi, H.; Uosaki, K.; Saruwatari, Y. Structure of Water at Zwitterionic Copolymer Film-Liquid Water Interfaces as Examined by the Sum Frequency Generation Method. *Colloids and surfaces. B, Biointerfaces* **2014**, *113*, 361–367.

(32) Leng, C.; Han, X.; Shao, Q.; Zhu, Y.; Li, Y.; Jiang, S.; Chen, Z. In Situ Probing of the Surface Hydration of Zwitterionic Polymer Brushes: Structural and Environmental Effects. *Journal Of Physical Chemistry C* **2014**, *118*, 15840–15845.

(33) Leng, C.; Buss, H. G.; Segalman, R. A.; Chen, Z. Surface Structure and Hydration of Sequence-Specific Amphiphilic Polypeptoids for Antifouling/Fouling Release Applications. *Langmuir* **2015**, *31*, 9306–9311.

(34) Boyd, R. W. Chapter 7 - Processes Resulting from the Intensity-Dependent Refractive Index. *Nonlinear Optics (Third Edition)* **2008**, 329–390.

(35) Shen, Y. R. The principles of nonlinear optics http://newcatalog.library.cornell.edu/catalog/52346.

(36) Tyrode, E.; Liljeblad, J. F. D. Water Structure Next to Ordered and Disordered Hydrophobic Silane Monolayers: A Vibrational Sum Frequency Spectroscopy Study. *The Journal of Physical Chemistry C* **2013**, *117*, 1780–1790.

(37) Becraft, K. A.; Richmond, G. L. In Situ Vibrational Spectroscopic Studies of the CaF 2/H 2O Interface. *Langmuir* **2001**, *17*, 7721–7724.

(38) Zhang, L.; Tian, C.; Waychunas, G. A.; Shen, Y. R. Structures and Charging of A-Alumina (0001)/Water Interfaces Studied by Sum-Frequency Vibrational Spectroscopy. *J. Am. Chem. Soc* **2008**, *130*, 7686–7694.

(39) Hopkins, A. J.; Schrödle, S.; Richmond, G. L. Specific Ion Effects of Salt Solutions at the CaF2/water Interface. *Langmuir* **2010**, *26*, 10784–10790.

(40) McFearin, C. L.; Richmond, G. L. The Role of Interfacial Molecular Structure in the Adsorption of Ions at the Liquid−Liquid Interface. *The Journal of Physical Chemistry C* **2009**, *113*, 21162–21168.

(41) Nomura, K.; Nakaji-Hirabayashi, T.; Gemmei-Ide, M.; Kitano, H.; Noguchi, H.; Uosaki, K. Sum-Frequency Generation Analyses of the Structure of Water at Amphoteric SAM-Liquid Water Interfaces. *Colloids and surfaces. B, Biointerfaces* **2014**, *121*, 264–269.

(42) Hopkins, A. J.; McFearin, C. L.; Richmond, G. L. SAMs under Water: The Impact of Ions on the Behavior of Water at Soft Hydrophobic Surfaces. *The Journal of Physical Chemistry C* **2011**, *115*, 11192–11203.

(43) Petersen, P. B.; Saykally, R. J. On the Nature of Ions at the Liquid Water Surface. *Annual Review of Physical Chemistry* **2006**, *57*, 333–364.

(44) Jungwirth, P.; Tobias, D. J. Specific Ion Effects at the Air/Water Interface. *Chemical Reviews* **2006**, *106*, 1259–1281.

(45) Vincent, J. C.; Matt, S. M.; Rankin, B. M.; D'Auria, R.; Freites, J. A.; Ben-Amotz, D.; Tobias, D. J. Specific Ion Interactions with Aromatic Rings in Aqueous Solutions: Comparison of Molecular Dynamics Simulations with a Thermodynamic Solute Partitioning Model and Raman Spectroscopy. *Chemical physics letters* **2015**, *638*, 1–8.

(46) Otten, D. E.; Shaffer, P. R.; Geissler, P. L.; Saykally, R. J. Elucidating the Mechanism of Selective Ion Adsorption to the Liquid Water Surface. *Proceedings of the National Academy of Sciences of the United States of America* **2012**, *109*, 701–705.

(47) Markovich, T.; Andelman, D.; Podgornik, R. Surface Tension of Electrolyte Interfaces: Ionic Specificity within a Field-Theory Approach. *Journal of Chemical Physics* **2015**, *142*, 044702.

(48) Rankin, B. M.; Ben-Amotz, D. Expulsion of Ions from Hydrophobic Hydration Shells. *J. Am. Chem. Soc* **2013**, *135*, 8818–8821.

(49) Duignan, T. T.; Parsons, D. F.; Ninham, B. W. Ion Interactions with the Air–Water Interface Using a Continuum Solvent Model. *The Journal of Physical Chemistry B* **2014**, *118*, 8700–8710.

(50) Hofmeister, F. Zur Lehre von Der Wirkung Der Salze. *Archiv für experimentelle Pathologie und Pharmakologie* **1888**, *25*, 1–30.

(51) Jungwirth, P.; Cremer, P. S. Beyond Hofmeister. *Nature Chemistry* **2014**, *6*, 261–263.

(52) Zhang, Y.; Cremer, P. S. Interactions between Macromolecules and Ions: The Hofmeister Series. *Current opinion in chemical biology* **2006**, *10*, 658–663.

(53) Marcus, Y. Effect of Ions on the Structure of Water: Structure Making and Breaking. *Chem. Rev* **2009**, *109*, 1346–1370.

(54) Chen, Y.; Okur, H. I.; Gomopoulos, N.; Macias-Romero, C.; Cremer, P. S.; Petersen, P. B.; Tocci, G.; Wilkins, D. M.; Liang, C.; Ceriotti, M.; Roke, S. Electrolytes Induce Long-Range Orientational Order and Free Energy Changes in the H-Bond Network of Bulk Water. *Science advances* **2016**, *2*, e1501891.

(55) Gierszal, K. P.; Davis, J. G.; Hands, M. D.; Wilcox, D. S.; Slipchenko, L. V.; Ben-Amotz, D. Π-Hydrogen Bonding in Liquid Water. *The Journal of Physical Chemistry Letters* **2011**, *2*, 2930–2933.

(56) Dobrowolski, J. C.; Jamróz, M. H. The IR Evidence of H2O-Aromatic Hydrocarbons Single Hydrogen Bond. *Journal of Molecular Structure* **1993**, *293*, 147–150.

(57) Besnard, M.; Danten, Y.; Tassaing, T. Dynamics of Solitary Water in Benzene and Hexafluorobenzene: An Infrared and Raman Study. *Journal of Chemical Physics* **2000**, *113*, 3741–3748.

(58) Auer, B. M.; Skinner, J. L. Water: Hydrogen Bonding and Vibrational Spectroscopy, in the Bulk Liquid and at the Liquid/vapor Interface. *Chemical physics letters* **2009**, *470*, 13–20.

(59) Tainter, C. J.; Ni, Y.; Shi, L.; Skinner, J. L. Hydrogen Bonding and OH-Stretch Spectroscopy in Water: Hexamer (Cage), Liquid Surface, Liquid, and Ice. *The Journal of Physical Chemistry Letters* **2012**, 12–17.

(60) Chen, X.; Yang, T.; Kataoka, S.; Cremer, P. S. Specific Ion Effects on Interfacial Water Structure near Macromolecules. *Journal of the American Chemical Society* **2007**, *129*, 12272–12279.

(61) Ong, S.; Zhao, X.; Eisenthal, K. B. Polarization of Water Molecules at a Charged Interface: Second Harmonic Studies of the Silica/water Interface. *Chemical physics letters* **1992**, *191*, 327–335.

(62) Yan, E. C. Y.; Liu, Y.; Eisenthal, K. B. New Method for Determination of Surface Potential of Microscopic Particles by Second Harmonic Generation. *The Journal of Physical Chemistry B* **1998**, *102*, 6331–6336.

(63) Jena, K. C.; Covert, P. A.; Hore, D. K. The Effect of Salt on the Water Structure at a Charged Solid Surface: Differentiating Second- and Third-Order Nonlinear Contributions. *The Journal of Physical Chemistry Letters* **2011**, *2*, 1056–1061.

(64) Hayes, P. L.; Malin, J. N.; Jordan, D. S.; Geiger, F. M. Get Charged up: Nonlinear Optical Voltammetry for Quantifying the Thermodynamics and Electrostatics of Metal Cations at Aqueous/oxide Interfaces. *Chemical physics letters* **2010**, *499*, 183–192.

(65) Tian, C.; Byrnes, S. J.; Han, H.-L.; Shen, Y. R. Surface Propensities of Atmospherically Relevant Ions in Salt Solutions Revealed by Phase-Sensitive Sum Frequency Vibrational Spectroscopy. *The Journal of Physical Chemistry Letters* **2011**, *2*, 1946–1949.

(66) Verreault, D.; Allen, H. C. Bridging the Gap between Microscopic and Macroscopic Views of Air/aqueous Salt Interfaces. *Chemical physics letters* **2013**, *586 IS* -, 1–9.

(67) Ananthapadmanabhan, K. P.; Goddard, E. D. Aqueous Biphase Formation in Polyethylene Oxide-Inorganic Salt Systems. *Langmuir* **1987**, *3*, 25–31.

(68) Huddleston, J. The Molecular Basis of Partitioning in Aqueous Two-Phase Systems. *Trends in Biotechnology* **1991**, *9*, 381–388.

(69) Florin, E.; Kjellander, R.; Eriksson, J. C. Salt Effects on the Cloud Point of the Poly(ethylene Oxide)+ Water System. *J. Chem. Soc., Faraday Trans. 1* **1984**, *80*, 2889–2910.

(70) Chanda, J.; Bandyopadhyay, S. Molecular Dynamics Study of Surfactant Monolayers Adsorbed at the Oil/water and Air/water Interfaces. *The Journal of Physical Chemistry B* **2006**, *110*, 23482–23488.

(71) Pluhařová, E.; Ončák, M.; Seidel, R.; Schroeder, C.; Schroeder, W.; Winter, B.; Bradforth, S. E.; Jungwirth, P.; Slavíček, P. Transforming Anion Instability into Stability: Contrasting Photoionization of Three Protonation Forms of the Phosphate Ion upon Moving into Water. *The Journal of Physical Chemistry B* **2012**, *116*, 13254–13264.

(72) Carolina P Carvalho; Jane Sélia R Coimbra; Isabele Andressa F Costa; Luís Antonio Minim; Luís Henrique M Silva; Maffia, and M. C. Equilibrium Data for PEG 4000 + Salt + Water Systems from (278.15 to 318.15) K. *Journal of chemical and engineering …* **2007**, *52*, 351–356.

(73) Lei, X.; Diamond, A. D.; Hsu, J. T. Equilibrium Phase Behavior of the Poly(ethylene Glycol)/potassium Phosphate/water Two-Phase System at 4.degree.C. *Journal of chemical and engineering …* **1990**, *35*, 420–423.

(74) Asenjo, J. A.; Andrews, B. A. Aqueous Two-Phase Systems for Protein Separation: Phase Separation and Applications. *Journal of Chromatography A* **2012**, *1238*, 1–10.

(75) Adamson, A. W.; Gast, A. P. Physical Chemistry of Surfaces. **1997**, *6th ed*.

(76) Schmidt, A. S.; Andrews, B. A.; Asenjo, J. A. Correlations for the Partition Behavior of Proteins in Aqueous Two-phase Systems: Effect of Overall Protein Concentration. *Biotechnology and Bioengineering* **1996**, *50*, 617–626.

(77) Mistry, S. L.; Kaul, A.; Merchuk, J. C.; Asenjo, J. A. Mathematical Modelling and Computer Simulation of Aqueous Two-Phase Continuous Protein Extraction. *Journal of Chromatography A* **1996**, *741*, 151–163.

(78) Schwierz, N.; Horinek, D.; Netz, R. R. Anionic and Cationic Hofmeister Effects on Hydrophobic and Hydrophilic Surfaces. *Langmuir* **2013**, *29*, 2602–2614.

(79) Gopalakrishnan, S.; Jungwirth, P.; Tobias, D. J.; Allen, H. C. Air-Liquid Interfaces of Aqueous Solutions Containing Ammonium and Sulfate: Spectroscopic and Molecular Dynamics Studies. *The Journal of Physical Chemistry B* **2005**, *109*, 8861–8872.

6. Brush polymers

6.1. Motivation

The number of Americans diagnosed with arthritis was 47.8 million in 2005, and is projected to increase to nearly 67 million by 2030.[1] Many people with knee arthritis are severely constrained by it, unable to climb stairs (10.2%), walk a mile (32.2%), or do heavy home chores (34.4%).[2] Osteoarthritis, the most prevalent type of arthritis,[3] results from mechanical damage to the joint tissue. Increased stress and friction at a defect begins a process of escalating damage which can progress to complete joint failure.[4] Despite the large and repetitive mechanical forces sustained by the surface of the joint, regeneration of the tissue is limited.[5] Articular cartilage is a highly structured matrix of primarily collagen and proteoglycans populated only by isolated chondrocytes (Figure 6.1). There is no vasculature. Synovial fluid bathes the articular surfaces and works along with the stiff yet permeable cartilage to distribute compressive force.[6,7] Macromolecules secreted by the chondrocytes, most notably lubricin (a boundary lubricant),[8] and hyaluronan (a viscous hydrodynamic lubricant) minimize friction between opposing joint faces.[9-11]

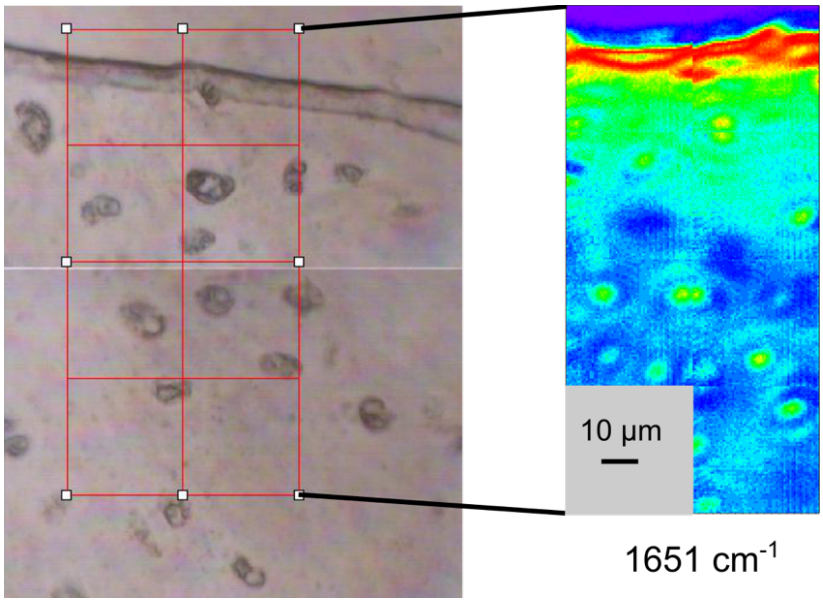

Figure 6.1 Articular cartilage from neonatal bovine fixed in formalin, 5 µm section. Each square is 34 µm wide. Left: image from visible microscope. Note thicker tangentially-oriented cartilage at surface (first 5 µm), and scattered chondrocytes throughout. Right: IR microscope image from similar sample at 1651 cm^{-1}, an amide peak. Concentric variation in the matrix density can be seen around chondrocytes.

Despite the high incidence of osteoarthritis, current pharmacological treatments are poor. They include pain relief (acetaminophen, non-steroidal anti-inflammatory drugs, and opioids), corticosteroid injection, hyaluronan injection, and supplements of glucosamine and chondroitin sulfate.[4,12] Evidence for short-term symptom reduction by corticosteroid injection is strong,[13] but is conflicting for hyaluronan[14,15] and only weakly positive for glucosamine/chondroitin sulfate.[6,16]

Augmentation of synovial fluid with lubricin or a lubricin-like substance is promising as a therapy. Lubricin is a proteoglycan with a negatively-charged, heavily glycosylated middle section (mucin-like), and positively-charged termini (Figure 6.2). The mucin domain assumes a bottle-brush conformation due to strong hydration of the sugars and charged residues. Steric repulsion causes lubricin molecules to slide past surfaces rather than intercalate, creating an excellent boundary lubricant.[17-19] Lubricin binds specifically to the articular surface by the

hemopexin-like domain at the C-terminus.[20,21] Both bound and solvated lubricin are important lubricants,[22] helping to create the extremely low friction coefficient of a healthy joint and prevent mechanical wear. But even as an acute or chronic injury leaves joint tissue vulnerable to further damage, expression of lubricin is down-regulated.[23-26]

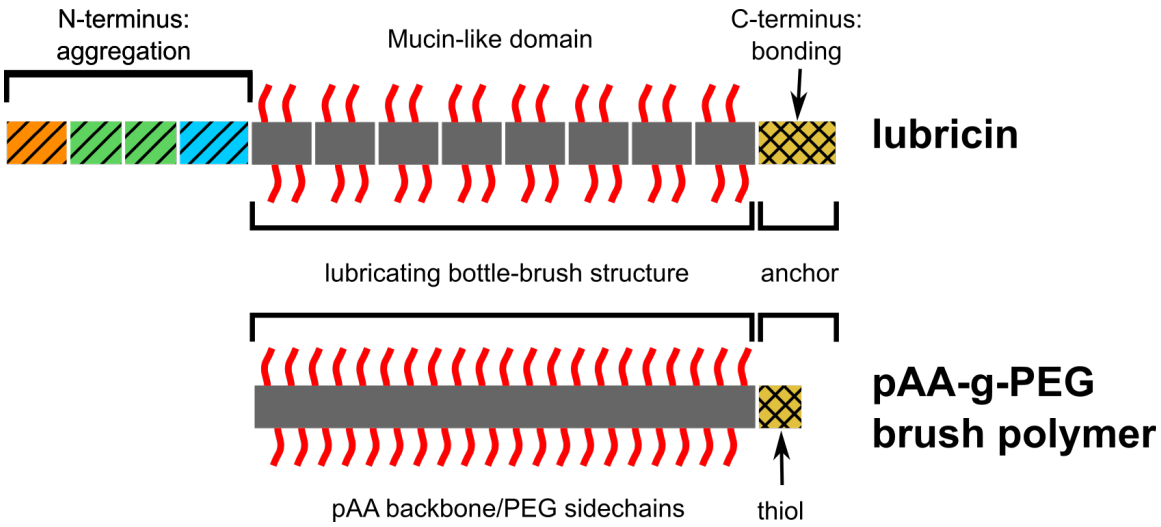

Figure 6.2 Comparison of lubricin and brush polymer structure

Intra-articular supplementation of lubricin was shown to reduce cartilage degeneration[27] (recombinant lubricin) and improve joint function in a rat model of osteoarthritis (lubricin from cultured human synoviocytes),[28] compared to placebo. While the benefits of lubricin are encouraging, both recombinant and extracted types are expensive, and an alternative is necessary.

A polymer was developed which, like lubricin, binds at one end to cartilage, and has a negatively-charged and strongly hydrated middle domain with a stiff, bottle-brush form (Figure 6.2).[29] In-vitro tests of cartilage lubrication and an in-vivo trial of a rat osteoarthritis model showed a similar protective effect for the polymer as for lubricin.[29,30] The lubricin mimic bound

to the articular surface and reduced friction. Joint cartilage from rats treated with the polymer had healthier tissue as determined by grading of histological sections and friction measurements.

In this collaboration, Ming-Chee Tan of the Putnam laboratory (Cornell School of Biomedical Engineering) synthesized the biomimetic polymer, and Kirk Samaroo of the Bonassar laboratory (Cornell School of Biomedical Engineering) characterized the polymer's effect on cartilage tribology. I was interested in the role of water in inducing the bottle-brush form of the lubricin and biomimetic polymer, to what extent water structure was similar at the two lubricants, and more generally, the effect of hydration on lubricity. Ultimately, the water structure could not be characterized by SFG due to the degree of polymer disorder, but I provided expertise in the characterization of the polymer composition. Determination of the optimal parameters of the polymer for joint protection is needed, but standard techniques have failed to characterize the polymers.

6.2. pAA-*g*-PEG brush polymer

In Professor Putnam's laboratory Tan synthesized[29] pAA-g-PEG brush polymers to mimic the structure of lubricin. The polymers have a backbone of poly (acrylic acid) to which branches of poly (ethylene glycol) are grafted (Figure 6.3). Three features of the brush polymers were varied: (1) the length of the pAA backbone, (2) the length of the PEG side chains, and (3) the proportion of acrylic acid repeats bonded with PEG. Each of these properties are indicated in the format pAA(*a*)-*g*-PEG(*b*), where *a* is the molecular weight of the pAA in kDa, *b* is the molecular weight of PEG in kDa, and *g* is the grafting ratio, or moles of PEG to pAA used in the condensation reaction.

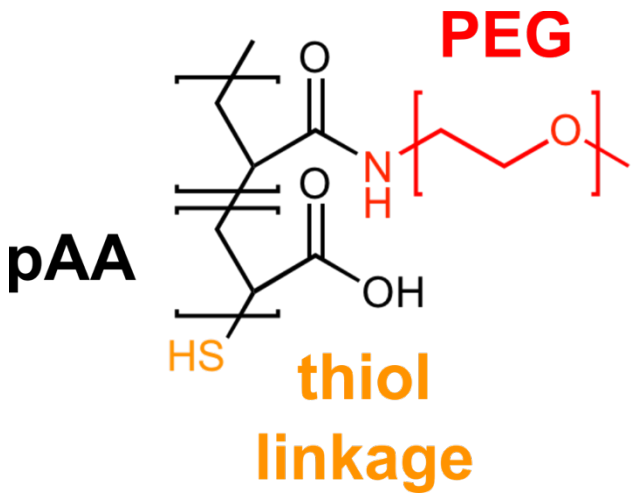

Figure 6.3 Structure of pAA-g-PEG brush polymer. The pAA backbone (black) consists of un-reacted acrylic acid and acrylic acid condensed with PEG (red), forming the brush structure. The thiol (orange) anchors the polymer to gold or cartilage.

Briefly, the polymers were synthesized in two steps. Reversible addition-fragmentation chain transfer[31,32] was used to polymerize acrylic acid into linear pAA polymers with low polydispersity. Next, PEG polymer with an amine terminus was grafted by condensation to the carboxylic acid of pAA.[33] The molecular weight of the pAA product could be accurately determined by gel permeation chromatography (GPC). The weight and polydispersity of the PEG came from a commercial source and was also well characterized. However, the efficiency of the grafting step was not known; due to the high density of the PEG side chains, it cannot be assumed that the fraction of the acrylic acid grafted to PEG (the conjugation percentage) will be equal to the grafting ratio.

Standard techniques for polymer analysis, GPC and proton NMR, could not be used to characterize the conjugation percentage of the full library of brush polymers. Due to the brush structure of the pAA-g-PEG, the polymer was too large for the pores of the GPC column, and also could not be accurately compared to the linear polymer standards. ^{1}H NMR could be used to quantify the amount of pAA and PEG in polymers with low grafting ratios, but failed for

polymers with high grafting ratios. The spectra were dominated by signal from the PEG. Polymers could also be sent out for analysis by multi-angle light scattering size exclusion chromatography (MALLS/SEC) to determine the size of all the brush polymers, but this was too expensive to do routinely.

6.3. FTIR spectra analysis

Fourier-transform infrared (FTIR) spectroscopy is an attractive strategy for polymer characterization as it allows the relative concentrations of pAA and PEG to be measured directly. Spectra of calibration standards, mixtures of un-conjugated pAA and PEG, were compared to spectra of brush polymers to determine their composition. Six to eight polymer solutions ranging from pure pAA to pure PEG in 0.1 M HCl / methanol were prepared, each with a total polymer concentration of 10 mg/mL. These solutions were spin-coated onto CaF_2 windows, and one of us took FTIR spectra in transmission. Brush polymer samples were prepared and analyzed in the same way.

The FTIR spectra of pAA and PEG are very different (Figure 6.4). PEG has a tight cluster of CH stretching modes between 2800 and 3000 cm^{-1} and sharp CH bending and CO stretching modes in the fingerprint region. pAA, due to hydrogen bonding of the carboxylic acid group, has very broad OH stretching peaks between 2400 and 3600 cm^{-1}, which obscure the CH stretching mode, and broad features below 1500 cm^{-1} as well. A result of pAA's hygroscopic property is the large effect of moisture on its spectrum: compare pAA and PEG in Figure 6.5. Emergence of the water OH stretch (3400 cm^{-1}), OH bend (1650 cm^{-1}), and the tail end of the water librations (<800 cm^{-1}) are clear but localized in the PEG spectrum when humidity is increased. Changes in humidity

results in more intense and diffuse effects for pAA. The large sensitivity to humidity complicates analysis of the brush polymers and pAA and PEG homopolymers mixtures, and either must be controlled for experimentally, or as was done in this study, in the data analysis.

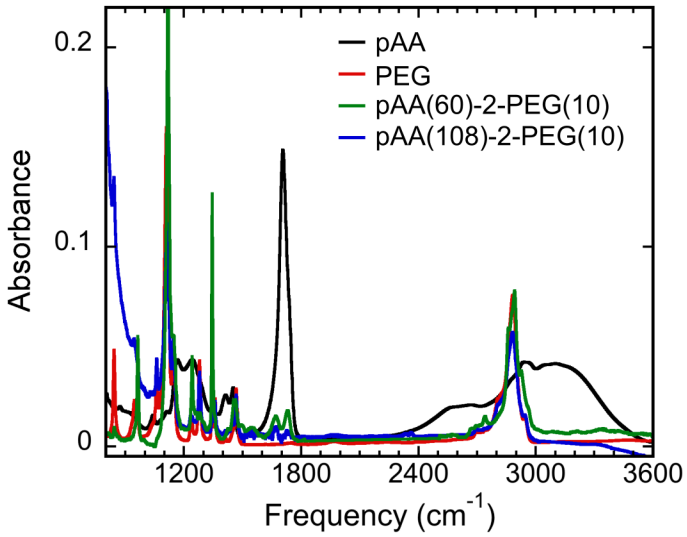

Figure 6.4 FTIR spectra of pAA and PEG homopolymers, along with two pAA-g-PEG brush polymers.

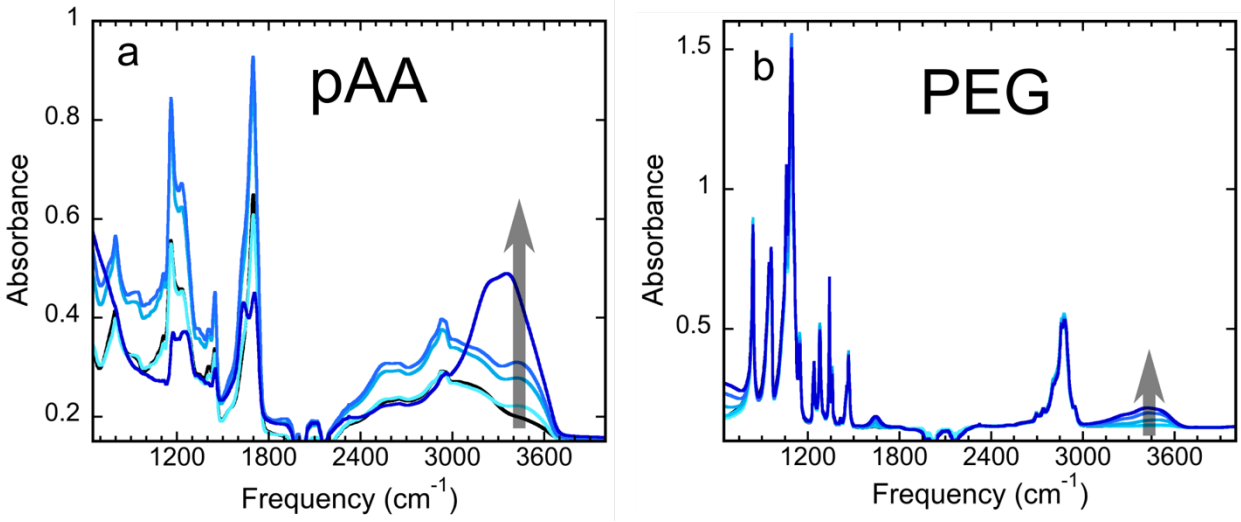

Figure 6.5 Effect of moisture on IR spectrum of polymers, from dry (black) to wet (dark blue): (a) pAA and (b) PEG

pAA does have one sharp feature, the carbonyl stretch at 1700 cm^{-1}, which appears in a region with no other resonance from either pAA or PEG. Its utility is complicated by water because it

coincides with the water bend. The frequency of the C=O stretch itself is sensitive to protonation and hydrogen bonding of carboxylic acid, the former changing the symmetry of the group and therefore the mode assignments, and the later causing shifts exceeding to 60 cm^{-1} upon hydrogen bonding.[34,35] Protonation state is unlikely to be a factor here as the pH of the polymer solutions (pH 1) is much lower than the pK_a of the acetic acid groups (~pH 4 [36]); all the acid groups should be protonated. Hydrogen bonding to other carboxylic acid groups explains the appearance of two peaks in the pAA/PEG homopolymer mixtures (the calibration standards) (Figure 6.6). Formation of cyclic homodimers between carboxylic acids such as formic and acetic acid[37-42] and longer chain mono-carboxylic acids[43] is well documented, and in fact the predominance of the dimer can make study of the monomer difficult. The lower energy 1710 cm^{-1} peak in Figure 6.6 is from the dimer, and the higher energy 1735 cm^{-1} peak from the monomer. The higher intensity of the dimer at high pAA fractions and of the monomer at low fractions supports this assignment.

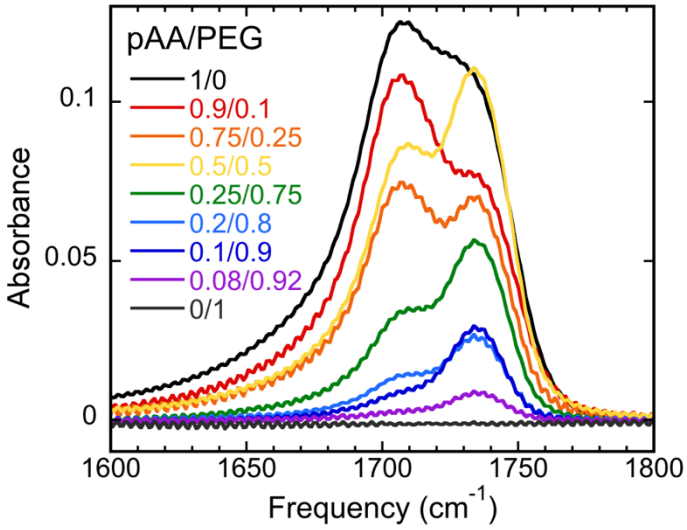

Figure 6.6 Change in pAA carbonyl with pAA/PEG fraction in calibration standards.

The situation is different for the brush polymers. In Figure 6.4, the pAA(60)-2-PEG(10) and pAA(108)-2-PEG(10) also have two carbonyl peaks, one at 1735 cm^{-1}, the monomer, and the other at 1668 cm^{-1}, the amide I mode arising from the carbonyl adjacent to PEG side chain. This structure expected: some un-conjugated carboxylic acid groups remain, but they are both isolated by bulky PEG chains and too low in number to form dimers. It is also a property of the brush polymers not replicated by the calibration standards. Therefore, the method of spectral analysis must predict the concentrations of pAA and PEG using the less intense CH and PEG CO modes.

6.4. Singular Value Decomposition (SVD)

Singular value decomposition (SVD) and basis rotation are used to create a calibration curve relating the FTIR spectra of pAA/PEG mixtures to their pAA fractions. The calibration curve is then used to calculate the pAA fraction of pAA-*g*-PEG brush polymers of unknown composition.

SVD is used here to decompose a set of related spectra into a series of basis vectors, each describing a decreasing amount of the variance between spectra in the data set. Decomposing a matrix $A_{n\times p}$ containing p spectra with length n produces three matrices:

$$A_{n\times p} = U_{n\times n} S_{n\times p} V^{\mathsf{T}}_{p\times p} \qquad \textbf{(6.1)}$$

The columns of $U_{n\times n}$ contain the basis vectors (eigenvectors of AA^{T}), in order of decreasing importance, or weight. $S_{n\times p}$ is a diagonal matrix with the singular values, which quantify the weight of each $U_{n\times n}$ vector. The elements of $V_{p\times p}$ (eigenvectors of $A^{\mathsf{T}}A$) are the coefficients giving the contribution of each of the basis vectors of $U_{n\times n}$ in each spectrum in $A_{n\times p}$.

The broadest meaningful frequency range of the data, 815-3600 cm^{-1}, is used in the spectral analysis, with the carbonyl region (1500-1800 cm^{-1}) excluded for the reasons discussed above. Differences in baseline between spectra, caused by scattering and variations in substrate path length, must be removed. Simple mean centering was the most effective. SVD factoring is applied to all the spectra at once, including standards and unknowns. Since each spectrum contains many more data points (n) than the number of spectra used in the analysis (p), the resulting basis set in $U_{n\times n}$ contains many more vectors than is necessary to describe the system. These excess vectors, and the corresponding rows and columns in $S_{n\times p}$ and $V_{p\times p}$, are removed. We get $U_{red,n\times N}$, $S_{red,N\times p}$, and $V_{p\times p}$, where $N = p$.

$U_{red}$is then rotated by $\Pi_{p\times p}$ to generate $X_{g,N\times p}$ so that the first two vectors $X_g(:,1)$ and $X_g(:,2)$ match the spectra of pure pAA and PEG, respectively (Figure 6.7).

$$X_g = U_{\text{red}}\Pi \qquad \textbf{(6.2)}$$

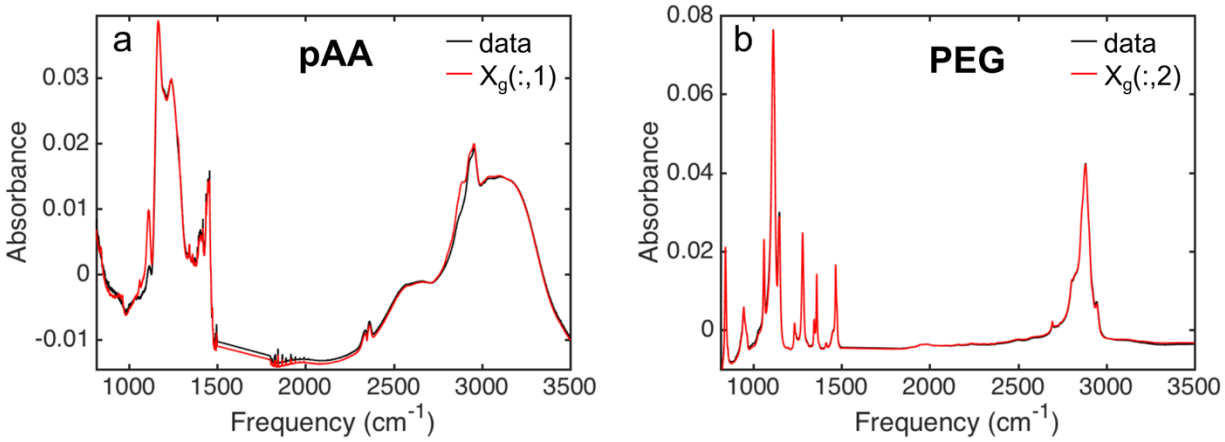

Figure 6.7 Agreement between spectra of pure homopolymers and Xg for (a) pAA (b) PEG

The elements of Π (a symmetric matrix) are solved for by least squares. Once Π and X_g are determined, V is rotated as well so that its elements relate the pAA and PEG character of each spectrum in the data set.

$$V_{\text{rot}} = V\Pi \qquad \textbf{(6.3)}$$

A pAA coefficient fraction is then calculated for each spectrum

$$\text{pAA coefficient fraction} = \frac{V_{\text{rot}}(:,1)}{V_{\text{rot}}(:,1) + V_{\text{rot}}(:,2)} \qquad \textbf{(6.4)}$$

and plotted against the known pAA fraction for the standards. This is fitted with an appropriate function (in this case, quadratic), to relate the two. Now the pAA fraction of the unknowns can be calculated from their pAA coefficient fraction.

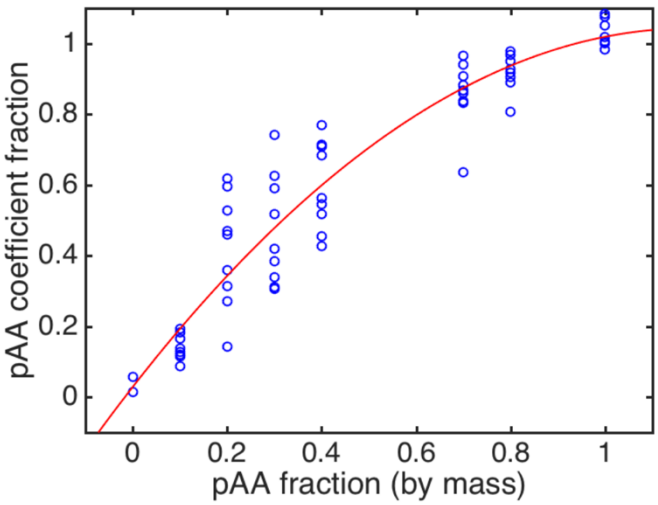

Figure 6.8 Calibration curve relating pAA coefficient fraction to known pAA mass fraction.

This technique produced plausible values for the conjugation percentage (the fraction of pAA repeats functionalized with PEG), and the degree of conjugation does increase with grafting

ratio. However, the sample-to-sample variation is large, and the values are very sensitive to the choice of frequency window. Results were particularly poor when a different batch of pAA was used to synthesize the brush polymer than used to prepare the standards, as with pAA(150)-0.5-PEG(2). Upon analyzing a different data set, it was apparent that this method is also intolerant of defects in the spectra such as water vapor and sloping baselines.

Table 6.1 Conjugation percentage for pAA-g-PEG brush polymers from SVD technique. Three polymer samples were characterized for each polymer type. Uncertainties are ± 1 standard deviation.

Polymer	**Conjugation %, SVD**
pAA(146)-0.25-PEG(2)	20±20
pAA(150)-0.5-PEG(2)*	500±900
pAA(146)-1-PEG(2)	30±30
pAA(146)-2-PEG(2)	50±10
***synthesized with different batch of pAA**	

6.5. Partial Least Squares (PLS) Regression

PLS regression is similar to SVD in that the independent variables are recombined and ordered to create a set of orthogonal vectors. However, in PLS the new basis set is not calculated by maximizing the variance in the independent variables, but by maximizing the covariance between the independent and dependent variables:[44-46] the spectra of the polymer mixtures and the corresponding pAA fractions. Only properties in the independent data (X) which are correlated with changes in the dependent data (Y) are given weight in the model. Both X and the

estimate of Y, $\hat{Y}$ are expressed in terms of T, the new orthogonal basis set. P and C are analogous to V in singular value decomposition, and is B analogous to S:

$$X = TP^{\intercal}\hat{Y} = TBC^{\intercal} \qquad \textbf{(6.5)}$$

The columns of T, or t, are the latent variables, and they are calculated by maximizing the covariance in X and Y:

$$\begin{gathered} t = Xw \\ u = Yx \\ \text{maximize } t^{\intercal}u \end{gathered} \qquad \textbf{(6.6)}$$

After the first t is found, the process is repeated to find the vector maximizing the remaining covariance, and this is continued until there are as many latent variables as there are independent variables. It is not desirable to use all the latent variables (LVs) in the prediction because, while the entire set of t contains as much information as X (i.e., all the spectra), we hope that there is a simpler underlying relationship between X and Y. If this is true, including too many LVs will only add noise. There are different methods of determining the optimal number, but they generally involve leaving out some members of X, calculating t and the X -weights w with the remainder, and finding the number of LVs after which the prediction of Y is not improved by adding more latent variables. One measure is root mean squared error of cross validation, RMSECV.

A collection of PLS functions[47] written for Matlab was used in this analysis. As before, the pAA carbonyl stretch region was excluded. The frequency range of 815-1500; 1800-3500 cm^{-1} was

chosen. Spectra were smoothed and differentiated once to remove baseline offset (Figure 6.9), and then mean centered to avoid bias toward more intense spectra.

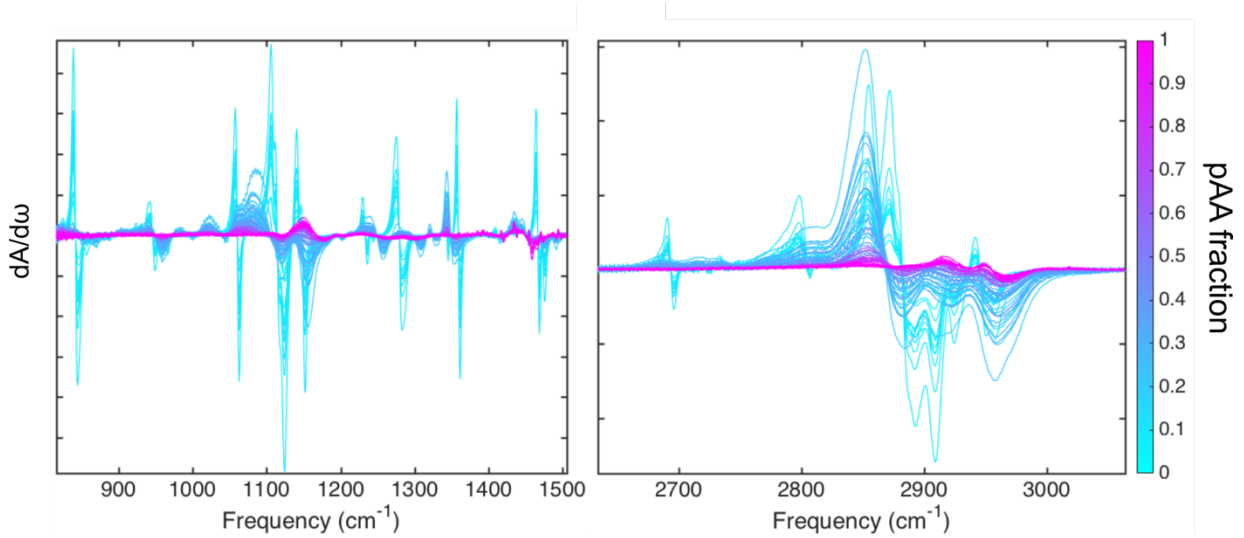

Figure 6.9 Derivative spectra of pAA(146)/PEG(2) standards used to build PLS model. Differentiating absorbance removed baseline offset from spectra, increasing consistency in the PLS model of the calibration set.

Cross validation shows the model is robust. The thirteen (of fifty-four) most outlying spectra as chosen by the Kennard-Stone algorithm were excluded from the model, and then the Y-predictions of this test group was compared to the predictions of the training group (Figure 6.10).

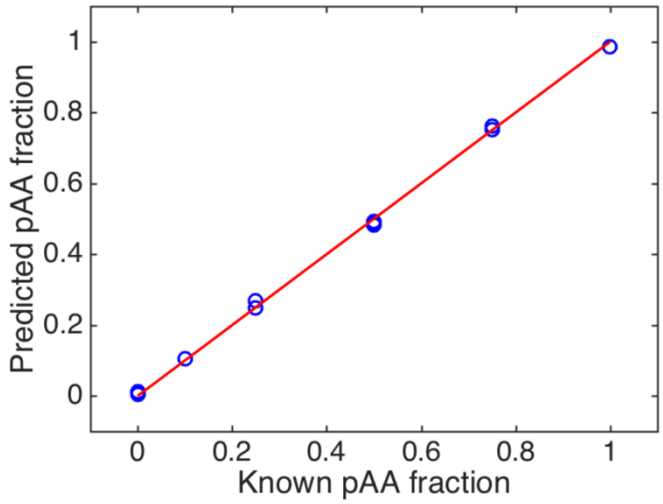

Figure 6.10 Validation of PLS model: model generated using training set (41 spectra), red line, and agreement of test set (13 spectra), blue circles.

The optimal LV number is ten (Figure 6.11), higher than the minimum of two (pAA and PEG) or three (including water), but much smaller than the number of spectra in the calibration set.

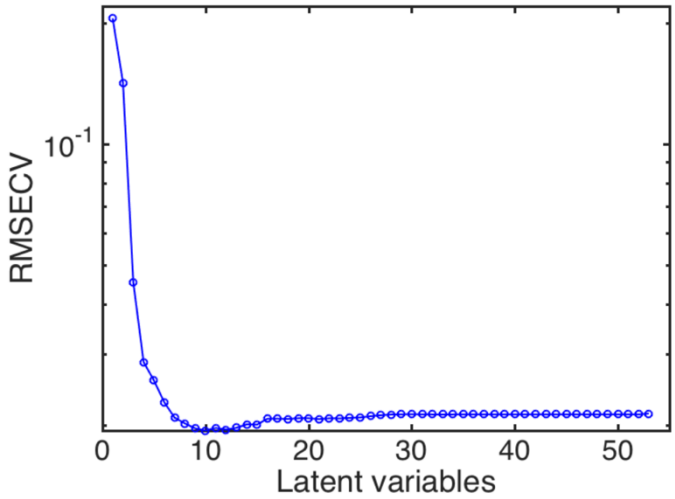

Figure 6.11 Root mean square error of cross validation (RMSECV) as a function of the number of latent variables in the model. Note minimum at LV=10.

The PLS method was used successfully to calculate plausible pAA fractions for the pAA(60)/PEG(2) data set, where SVD failed. The conjugation percent values agree well with those determined by standard methods (light scattering, NMR, and GPC) for brush polymers

with lower grafting ratios, but not for higher ratios. Since acrylic acid COOH moieties become amides upon condensation with PEG, the calibration standards grow less representative of brush polymers as the grafting ratio increases. Predictions of conjugation percentage may fail at higher graft ratios due to this mismatch. While the carbonyl region (1500-1800 cm^{-1}) was initially left out of the analysis due the carboxylic acid/amide issue, its inclusion actually improves the prediction of conjugation percentage (Table 6.2). This suggests that sensitivity to pAA is the limiting factor, as the carbonyl peak is the most intense and distinctive feature of the spectrum of pAA (Figure 6.4). Polymers with a high conjugation percentage also have low pAA content, only 4.3% at full conjugation.

Table 6.2 PEG conjugation percentage (%C). PLS uncertainty given as one standard deviation.

Polymer	**% C, reference**	**% C, PLS w/ C=O**	**% C, PLS w/out C=O**	**# replicates, PLS**
pAA(60)-2-PEG(2)	81.2*	300±800	-270±200	6
pAA(60)-1-PEG(2)	~100†	100±20	120±40	3
pAA(60)-0.5-PEG(2)	23.1†	26±2	22±6	5
pAA(60)-0.25-PEG(2)	23.7†	23.8±0.7	20.2±0.9	3
*** From MALLS/SEC † From ^{1}H NMR**		**LV=10**	**LV=14**	

6.6. Conclusions

PLS regression analysis of IR spectra predicted the brush polymer pAA content with higher precision than SVD decomposition, but was only effective for pAA-*g*-PEG brush polymers with low conjugation ratios. Due to its low detection limit, UV spectroscopy could be more successful. Poly (acrylic acid) has a pK_a around 4,[36] and so at neutral pH, a cationic dye could be used to label the negatively-charged COO^- groups of the backbone. By adding a second dye with specific affinity for the ethylene oxide groups of PEG, the ratio of the dye concentrations could be determined. In addition, the concentration of dye bound to PEG (or pAA) alone should be enough to calculate the conjugation percentage, avoiding the sensitivity issue encountered with NMR and FTIR for very low pAA fractions. Some challenges would include calibration

(determination of dye binding efficiency) and low polymer solubility. Quantitative digestion of brush polymers into pAA and PEG homopolymers followed GPC is another possible strategy.

References

(1) Hootman, J. M.; Helmick, C. G. Projections of US Prevalence of Arthritis and Associated Activity Limitations. *Arthritis Rheum.* **2006**, *54* (1), 226–229.

(2) Guccione, A. A.; Felson, D. T.; Anderson, J. J.; Anthony, J. M.; Zhang, Y.; Wilson, P. W.; Kelly-Hayes, M.; Wolf, P. A.; Kreger, B. E.; Kannel, W. B. The Effects of Specific Medical Conditions on the Functional Limitations of Elders in the Framingham Study. *Am J Public Health* **1994**, *84* (3), 351–358.

(3) Lawrence, R. C.; Felson, D. T.; Helmick, C. G.; Arnold, L. M.; Choi, H.; Deyo, R. A.; Gabriel, S.; Hirsch, R.; Hochberg, M. C.; Hunder, G. G.; et al. Estimates of the Prevalence of Arthritis and Other Rheumatic Conditions in the United States. Part II. *Arthritis Rheum.* **2008**, *58* (1), 26–35.

(4) Felson, D. T. Osteoarthritis of the Knee. *N Engl J Med* **2006**, *354* (8), 841–848.

(5) Bhosale, A. M.; Richardson, J. B. Articular Cartilage: Structure, Injuries and Review of Management. *Br Med Bull* **2008**, *87* (1), 77–95.

(6) Sherman, A. L.; Ojeda-Correal, G.; Mena, J. Use of Glucosamine and Chondroitin in Persons with Osteoarthritis. *PM&R* **2012**, *4* (5), S110–S116.

(7) Sophia Fox, A. J.; Bedi, A.; Rodeo, S. A. The Basic Science of Articular Cartilage: Structure, Composition, and Function. *Sports Health* **2009**, *1* (6), 461–468.

(8) Schumacher, B. L.; Block, J. A.; Schmid, T. M.; Aydelotte, M. B.; Kuettner, K. E. A Novel Proteoglycan Synthesized and Secreted by Chondrocytes of the Superficial Zone of Articular Cartilage. *Arch. Biochem. Biophys.* **1994**, *311* (1), 144–152.

(9) Mabuchi, K.; Tsukamoto, Y.; Obara, T.; Yamaguchi, T. The Effect of Additive Hyaluronic Acid on Animal Joints with Experimentally Reduced Lubricating Ability. *J. Biomed. Mater. Res.* **1994**, *28* (8), 865–870.

(10) Tadmor, R.; Chen, N.; Israelachvili, J. N. Thin Film Rheology and Lubricity of Hyaluronic Acid Solutions at a Normal Physiological Concentration. *J. Biomed. Mater. Res.* **2002**, *61* (4), 514–523.

(11) Swann, D. A.; Radin, E. L. The Molecular Basis of Articular Lubrication I. PURIFICATION and PROPERTIES of a LUBRICATING FRACTION FROM BOVINE SYNOVIAL FLUID. *J. Biol. Chem.* **1972**, *247* (24), 8069–8073.

(12) Sinusas, K. Osteoarthritis: Diagnosis and Treatment. *Am Fam Physician* **2012**, *85* (1), 49–56.

(13) Arroll, B.; Goodyear-Smith, F. Corticosteroid Injections for Osteoarthritis of the Knee: Meta-Analysis. *BMJ* **2004**, *328* (7444), 869.

(14) Rutjes, A. W. S.; Jüni, P.; da Costa, B. R.; Trelle, S.; Nüesch, E.; Reichenbach, S. Viscosupplementation for Osteoarthritis of the Knee: a Systematic Review and Meta-Analysis. *Ann Intern Med* **2012**, *157* (3), 180–191.

(15) Lo, G. H.; LaValley, M.; McAlindon, T.; Felson, D. T. Intra-Articular Hyaluronic Acid in Treatment of Knee Osteoarthritis: a Meta-Analysis. *JAMA* **2003**, *290* (23), 3115–3121.

(16) Vangsness, C. T., Jr.; Spiker, W.; Erickson, J. A Review of Evidence-Based Medicine for Glucosamine and Chondroitin Sulfate Use in Knee Osteoarthritis. *Arthroscopy: The Journal of Arthroscopic & Related Surgery* **2009**, *25* (1), 86–94.

(17) Coles, J. M.; Chang, D. P.; Zauscher, S. Molecular Mechanisms of Aqueous Boundary Lubrication by Mucinous Glycoproteins. *Curr Opin Colloid in* **2010**, *15* (6), 406–416.

(18) Zappone, B.; Ruths, M.; Greene, G. W.; Jay, G. D.; Israelachvili, J. N. Adsorption, Lubrication, and Wear of Lubricin on Model Surfaces: Polymer Brush-Like Behavior of a Glycoprotein. *Biophysical Journal* **2007**, *92* (5), 1693–1708.

(19) Jay, G. D.; Harris, D. A.; Cha, C.-J. Boundary Lubrication by Lubricin Is Mediated by O-Linked B(1-3)Gal-GalNAc Oligosaccharides. *Glycoconj J* **2001**, *18* (10), 807–815.

(20) Jones, A. R. C.; Gleghorn, J. P.; Hughes, C. E.; Fitz, L. J.; Zollner, R.; Wainwright, S. D.; Caterson, B.; Morris, E. A.; Bonassar, L. J.; Flannery, C. R. Binding and Localization of Recombinant Lubricin to Articular Cartilage Surfaces. *Journal of Orthopaedic Research* **2007**, *25* (3), 283–292.

(21) Abubacker, S.; Ponjevic, D.; Ham, H. O.; Messersmith, P. B.; Matyas, J. R.; Schmidt, T. A. Effect of Disulfide Bonding and Multimerization on Proteoglycan 4'S Cartilage Boundary Lubricating Ability and Adsorption. *Connective Tissue Research* **2016**, *57* (2), 113–123.

(22) Gleghorn, J. P.; Jones, A. R. C.; Flannery, C. R.; Bonassar, L. J. Boundary Mode Lubrication of Articular Cartilage by Recombinant Human Lubricin. *Journal of Orthopaedic Research* **2009**, *27* (6), 771–777.

(23) Elsaid, K. A.; Fleming, B. C.; Oksendahl, H. L.; Machan, J. T.; Fadale, P. D.; Hulstyn, M. J.; Shalvoy, R.; Jay, G. D. Decreased Lubricin Concentrations and Markers of Joint Inflammation in the Synovial Fluid of Patients with Anterior Cruciate Ligament Injury. *Arthritis Rheum.* **2008**, *58* (6), 1707–1715.

(24) Ludwig, T. E.; McAllister, J. R.; Lun, V.; Wiley, J. P.; Schmidt, T. A. Diminished Cartilage-Lubricating Ability of Human Osteoarthritic Synovial Fluid Deficient in Proteoglycan

4: Restoration Through Proteoglycan 4 Supplementation. *Arthritis Rheum.* **2012**, *64* (12), 3963–3971.

(25) Young, A. A.; McLennan, S.; Smith, M. M.; Smith, S. M.; Cake, M. A.; Read, R. A.; Melrose, J.; Sonnabend, D. H.; Flannery, C. R.; Little, C. B. Proteoglycan 4 Downregulation in a Sheep Meniscectomy Model of Early Osteoarthritis. *Arthritis Res. Ther.* **2006**, *8* (2), R41.

(26) Elsaid, K. A.; Jay, G. D.; Chichester, C. O. Reduced Expression and Proteolytic Susceptibility of Lubricin/Superficial Zone Protein May Explain Early Elevation in the Coefficient of Friction in the Joints of Rats with Antigen-Induced Arthritis. *Arthritis Rheum.* **2007**, *56* (1), 108–116.

(27) Flannery, C. R.; Zollner, R.; Corcoran, C.; Jones, A. R.; Root, A.; Rivera Bermúdez, M. A.; Blanchet, T.; Gleghorn, J. P.; Bonassar, L. J.; Bendele, A. M.; et al. Prevention of Cartilage Degeneration in a Rat Model of Osteoarthritis by Intraarticular Treatment with Recombinant Lubricin. *Arthritis Rheum.* **2009**, *60* (3), 840–847.

(28) Jay, G. D.; Elsaid, K. A.; Kelly, K. A.; Anderson, S. C.; Zhang, L.; Teeple, E.; Waller, K.; Fleming, B. C. Prevention of Cartilage Degeneration and Gait Asymmetry by Lubricin Tribosupplementation in the Rat Following Anterior Cruciate Ligament Transection. *Arthritis Rheum.* **2012**, *64* (4), 1162–1171.

(29) Tan, M.-C. Synthesis, Characterization and Evaluation of Poly(Acrylic Acid)-Graft-Poly(Ethylene Glycol)'S as Boundary Lubricants for Treatment of Osteoarthritis, Ithaca, NY, 2015.

(30) Putnam, D.; Tan, M.; Samaroo, K. J.; Bonassar, L. J.; Cornell University. Biomimetic Boundary Lubricants for Articular Cartilage. US Patent Office October 1, 2015.

(31) Pelet, J. M.; Putnam, D. Poly(Acrylic Acid) Undergoes Partial Esterification During RAFT Synthesis in Methanol and Interchain Disulfide Bridging Upon NaOH Treatment. *Macromolecular Chemistry and Physics* **2012**, *213* (23), 2536–2540.

(32) Chiefari, J.; Chong, Y. K. B.; Ercole, F.; Krstina, J.; Jeffery, J.; Le, T. P. T.; Mayadunne, R. T. A.; Meijs, G. F.; Moad, C. L.; Moad, G.; et al. Living Free-Radical Polymerization by Reversible Addition−Fragmentation Chain Transfer: the RAFT Process. *Macromolecules* **1998**, *31* (16), 5559–5562.

(33) Pelet, J. M.; Putnam, D. An in-Depth Analysis of Polymer-Analogous Conjugation Using DMTMM. *Bioconjugate Chem.* **2011**, *22* (3), 329–337.

(34) Barth, A. Infrared Spectroscopy of Proteins. *Biochim. Biophys. Acta* **2007**, *1767* (9), 1073–1101.

(35) Takei, K.-I.; Takahashi, R.; Noguchi, T. Correlation Between the Hydrogen-Bond Structures and the C=O Stretching Frequencies of Carboxylic Acids as Studied by Density Functional Theory Calculations: Theoretical Basis for Interpretation of Infrared Bands of Carboxylic Groups in Proteins. *J Phys Chem B* **2008**, *112* (21), 6725–6731.

(36) *CRC Handbook of Chemistry and Physics*, 95 ed.; Haynes, W. M., Bruno, T. J., Lide, D. R., Eds.; CRC Press: [Place of publication not identified], 2014.

(37) Bulmer, J. T.; Shurvell, H. F. Factor Analysis as a Complement to Band Resolution Techniques. I. the Method and Its Application to Self-Association of Acetic Acid. *J. Phys. Chem* **1973**, *77* (2), 256–262.

(38) Maréchal, Y. IR Spectra of Carboxylic Acids in the Gas Phase: a Quantitative Reinvestigation. *Journal of Chemical Physics* **1987**, *87* (11), 6344–6353.

(39) Burneau, A.; Ge nin, F.; Quilès, F. Ab Initio Study of the Vibrational Properties of Acetic Acid Monomers and Dimers. *Phys. Chem. Chem. Phys.* **2000**, *2* (22), 5020–5029.

(40) Halupka, M.; Sander, W. A Simple Method for the Matrix Isolation of Monomeric and Dimeric Carboxylic Acids. *Spectrochimica Acta Part A: Molecular and Biomolecular Spectroscopy* **1998**, *54* (3), 495–500.

(41) Gantenberg, M.; Halupka, M.; Sander, W. Dimerization of Formic Acid-an Example of a "Noncovalent" Reaction Mechanism. *Chem. Eur. J.* **2000**, *6* (10), 1865–1869.

(42) Maçôas, E. M. S.; Myllyperkiö, P.; Kunttu, H.; Pettersson, M. Vibrational Relaxation of Matrix-Isolated Carboxylic Acid Dimers and Monomers. *J. Phys. Chem. A* **2009**, *113* (26), 7227–7234.

(43) Eliason, T. L.; Havey, D. K.; Vaida, V. Gas Phase Infrared Spectroscopic Observation of the Organic Acid Dimers (CH3(CH2)6COOH)2, (CH3(CH2)7COOH)2, and (CH3(CH2)8COOH)2. *Chemical physics letters* **2005**, *402* (1-3), 239–244.

(44) Wold, S.; Sjöström, M.; Eriksson, L. PLS-Regression: a Basic Tool of Chemometrics. *Chemometrics and Intelligent Laboratory Systems* **2001**, *58* (2), 109–130.

(45) Adams, M. J. *Chemometrics in Analytical Spectroscopy*; Royal Society of Chemistry: Cambridge [England] ET -, 1995.

(46) Abdi, H. Partial Least Squares Regression and Projection on Latent Structure Regression (PLS Regression). *Wiley Interdisciplinary Reviews: Computational Statistics* **2010**, *2* (1), 97–106.

(47) Li, H.; Xu, Q.; Liang, Y. libPLS: an Integrated Library for Partial Least Squares Regression and Discriminant Analysis. **2014**.